Design and Construction of a Raman Microscope for Nano-Plasmonic Structures

by
Maryam Habeeb Alshehab

A thesis presented to the
Faculty of Graduate and Postdoctoral Studies
in partial fulfillment of the requirements for the degree of

Master of Applied Science
In Electrical Engineering

Ottawa-Carleton Institute for Electrical and Computer Engineering
School of Electrical Engineering and Computer Science
Faculty of Engineering
University of Ottawa

Abstract

Nanometallic structures efficiently convert light to surface plasmon-polaritons (SPPs) localized to ultra-small volumes. Such structures can provide highly enhanced fields and are of interest in applications involving plasmon-enhanced nonlinear optics. In this study, the devices consist of rectangular gold nanoantennas on a graphene layer on a SiO_2/Si substrate. The nanoantennas are used to exploit SPPs to enhance the interaction between graphene and light.

Specifically, plasmon-enhanced Raman scattering from graphene is of interest. Here, the nanoantennas are spectrally-aligned with a Stokes wavelength of graphene. With the addition of a second laser source, stimulated Raman scattering can be achieved. The first laser source pumps the sample's atoms and molecules into virtual excited states and the second one stimulates emission of a photon and relaxation to a higher mode of the ground state. This work involves designing and constructing a stimulated and spontaneous Raman microscope and also a reflectance measurement tool. Within the framework of this thesis, Raman scattering enhancement in graphene based on plasmonic resonant enhancement of the Stokes emission is demonstrated, providing a maximum cross-sectional gain of approximately 500 per antenna. This work also shows the normalized reflectance response of the nanoantenna structures of different length and width and how their resonant wavelengths shift.

Acknowledgment

First and foremost I wish to express my gratitude to my supervisor Dr. Pierre Berini for giving me this opportunity and providing guidance through my masters study. Thank you for your invaluable advice and your endless patience and encouragement. I would also like to thank Dr. Behnood Ghamsari for introducing and designing this microscope setup with me as well as providing assistance when needed. I would also to express my appreciation to Dr. Jaspreet Walia for providing assistance in the last months of my thesis and helping use the WiTec Raman microscope.

I am very grateful to Anthony Olivieri for fabricating my nanoantennas and guiding me through all the technical parts of my work. I would also like to thank all my lab coworkers and friends for helping when needed, Saba Siadat Mousavi for providing the needed simulation work, Dr. Oleksiy Krupin for helping me setup the fiber, Maude Amyot-Bourgeois for helping with fabrication when I needed it and Dr. Choloong Han for providing suggestions and assistance with the spectrometer.

Finally, none of this would have been possible without the love and support of my parents and siblings. Thank you for constantly supporting me, believing in me and pushing me to do better.

Table of Content

List of Figures

List of Tables

Nomenclature, Acronyms and Symbols

Latin letters and Acronyms

2-D	2-Dimensional
AFM	Atomic force microscope
Ag	Silver
APD	Avalanche Photodiode
ARC	Anti-Reflection Coating
ASE	Strong amplified spontaneous emission
Au	Gold
BS	Beam splitter
CCD	Charge Coupled Device
Cu	Copper
DAQ	Data Acquisition card
DF	Dose factor
DM	Dichroic Mirror
E-beam	Electron-beam
EC-SERS	Electrochemical SERS
FDTD	Finite difference time domain
FT	Fourier transform
FWHM	Full Width at Half Maximum
Hb	Hemoglobin
He-Ne	Helium Neon
HMW	High molecular weight
IPA	Isopropyl alcohol
IR	Infrared

Latin letters and Acronyms

LMW	Low molecular weight
LSPs	Localized surface plasmons
MB	Methalyne blue
MFD	Mode Field Diameter
MIPK	Methyl isopropyl ketone
MIS	Metal-insulator-semiconductors
MOS	Metal-oxide-semiconductors
MW	Molecular weight
NA	Numerical Aperture
NDF	Neutral Density Filter
OD	Optical Density
PD	Photo-Detector
PMMA	poly(methyl methacrylate)
PMT	Photomultiplier Tubes
R6G	Rhodium 6G
RF	Radio Frequency
RS	Raman Scattering
SERS	Surface Enhanced Raman Scattering
Si	Silicon
SNR	Signal-to-noise ratio
SP	Surface plasmons
SPPs	Surface plasmon polaritons
TE	Transverse electric modes

SRR	Split-ring resonators	TM	Transverse Magnetic modes
SRS	Stimulated Raman Spectroscopy	WD	Working Distance
SuperK	Super-Continuum		

Greek Letters and constants

λ	Wavelength
$\hbar$	Planck's Constant =$6.62607004 \times 10^{-34}\ m^2kg/s$
c	Speed of light =$2.99 \times 10^8\ \ m/s$

Chapter 1 – Introduction

1.1 Introduction and Motivation

Metallic nanostructures and their interaction with light have been studied for their optical properties for a number of years. Plasmonic structures based on noble metals specifically are more widely studied due to their favorable optical properties around the visible frequency spectrum. Plasmons are coupled oscillations of light and free electrons at a metal-dielectric interface and in bulk metal [1]. Plasmons have fields that propagate or resonate with localization that may be beyond the diffraction limit. Surface plasmonics was instigated by a prediction of electron energy losses for an electron beam traversing a thin metal film under the energy of bulk plasmons [2].There are two essential plasmon excitations, propagating SPPs and resonating (or localized) surface plasmons (LSPs). Noble metals can support SPPs over the visible and infrared parts of the spectrum and are used for applications such as nanophotonic waveguides [3].

Surface plasmons involve the collective oscillation of free electrons in conducting materials. Surface plasmons (SPs) are the electromagnetic waves coupled to charge excitation at the surface of a metal [4]. Plasmons have a few properties that make them ideal for photonic applications. The most important are: 1) their small spatial extension related to the wavelength of light allowing for a better imaging resolution; 2) their strong interaction with light, which can allow, *e.g.*, the creation of colors through plasmons; 3) the strong optical field enhancement that they can produce [5].

SPPs can confine electromagnetic energies to deep-subwavelength scales, which in return can enhance light-matter interaction at nanoscales [3]. The characteristics of molecular spectroscopy and imaging such as spectral intensity and spatial resolution can be altered by plasmonic nanomaterials. This triggered the development of optical spectroscopy techniques such as surface enhanced Raman scattering (SERS) [1]. SERS has become a widely-used spectroscopy technique with single molecule sensitivity and chemical specificity. Furthermore, plasmonic metallic nanostructures can increase the spatial resolution and the strength of the SERS signal for detection. More specifically, graphene-based SERS has

attracted considerable interest since it can combine chemical and electromagnetic enhancement to achieve single molecular sensitivity.

At the end of chapter one, the scope and organization of this thesis are introduced. Chapter two provides a general introduction to SERS based on optical nanoantennas on graphene. The general theory will be discussed while also providing some background on previous studies. The motivation behind this work was to further the work of Ghamsari *et al*. [6] by building a custom Raman microscope which includes a stimulated Raman emission arm. The work of Ghamsari consisted of enhancing the graphene Raman signal by aligning the resonance of the nanoantenna with that of the stoke wavelengths as opposed to pump wavelengths.

1.2 Thesis Objective and Contributions

The objective of this thesis is to build a Raman microscope that can be slightly altered to obtain three different measurements, which are:

1. Normalized reflectance measurements
2. Spontaneous Raman measurements
3. Stimulated Raman measurements

The main focuses of this work is to build a functioning Raman microscope, which includes designing, acquiring and assembling a custom set-up and repeating the measurements of Behnood Ghamsari to enhance the graphene Raman signal with nanoantennas [6]. The measurements are carried out on graphene samples with gold nanoantenna arrays to enhance the signal. The Raman microscope must be sensitive enough to acquire a Raman signal without the need of enhancement. One of the main contributions of this work is the stimulated Raman microscope arm, which uses a secondary Stokes source. The built spectroscopy tool can have elements added or removed easily to result in different functionalities such as adding a notch filter for anti-stoke measurements. The set-up is controlled and data are acquired via software written in LabVIEW.

1.3 Thesis Organization

The reminder of this thesis is organized as follows. The second chapter, entitled “Background and literature review” will discuss the relevant background information and the research conducted by others related to this thesis. The third chapter entitled, “Optical Setup”, discusses the Raman microscope and its design, which includes four arms, as well as the various software programs written to control the microscope and collect data. Chapter four entitled “Measurements and Results” will discuss briefly the device structure and its fabrication process, the experimental procedures developed, and the measurements obtained. The thesis ends in Chapter five with some concluding remarks and suggestions for future work. Followed by that is a few appendices containing relevant but not crucial information.

Chapter 2 – Background and Literature Review

2.1 Surface Enhanced Raman Spectroscopy

2.1.1 Introduction

In the last few decades laser spectroscopy has been a fast developing field. The technique has an important role in biophysics/biochemistry and the life sciences. Spectroscopy is used in research, diagnosis of diseases and therapy control [7]. Spectroscopy allows the identification and structural characterization of molecules without coming in contact with them thus the molecules will not be damaged; consequently, it has gained significant interest from researchers. Raman spectroscopy is a spectroscopic technique probing vibrational and rotational levels of molecules providing high accuracy structural information and thus it is of high interest from a fundamental standpoint as well as for identifying chemical species specifically. The biggest disadvantage of Raman spectroscopy is the weak signals from the Raman process; the magnitude of the cross-section for the process is in the order of $12 - 14$ lower than the fluorescence cross-section [8].

The first account of Raman Spectroscopy study on electrochemical systems was conducted by Fleischmann, Hendra and McQuillan in 1973 [9]. They observed a strong and potential-dependent Raman signals on thin Hg_2Cl_2, Hg_2Br_2, and HgO films formed on mercury droplets electrodeposited on platinum electrodes. These compounds have a good Raman scattering signal, thus the experiment proved the possibility of Raman spectroscopic measurements under the electrochemical environment. This was followed by Van Duyne *et al*. in 1975 reporting that they were able to obtain Raman signals of electrochemically radical ions both in bulk electrolyte and diffusion layer [10]. This was due to the fact that normal Raman scattering is too weak to be measured in those species in the thin diffusion layer. Thus, the use of resonance Raman spectroscopy was essential to boost the detection sensitivity.

In mid to late 1970s it was discovered that molecules absorbed on a specially prepared silver surface produce a Raman signal that is a million times more intense than expected through the contribution of Fleischmann and Van Duyne [11], [12]. This discovery of a high

gained attention after it was deduced that the high Raman signals are caused by enhancement of Raman scattering (RS). This effect was named SERS [13]. The enhancement factors for Raman were originally $10^3 - 10^5$ but later the enhancement grew to $10^{10} - 10^{11}$ for dye molecules in SERS experiments [7]. This discovery was the starting point to design highly sensitive surface diagnostic techniques applicable to electrochemical, biological and other interfaces. Van Duyne who suggested the acronym SERS [13] has stated in a follow up publication [14] the claim that his group discovered SERS. He believes that the first experimental observation of the phenomenon establishes its discovery.

The biggest contributor to the intensity enhancement is an electromagnetic effect due to the laser excitation of localized surface plasmons at metal surfaces, thus creating an enhanced electric field (E) [15]. The incident and scattered fields are affected by enhancements which results in a total signal enhancement proportional to the fourth power E^4. A motivating factor for SERS is its spatial resolution, where SERS can provide a lateral resolution better than 10 nm for metallic nanostructures. This resolution is two orders of magnitude below the diffraction limit, thus eliminating the need for a focusing lens. SERS also has the advantage of higher specificity since the Raman spectrum is a result of vibrational frequencies of molecules.

2.1.2 Raman Scattering

To observe the impacts of SERS, one needs to discuss Raman scattering first. Raman scattering is a process involving a photon and a molecule. Incoming photons of energy hv_L incident on a molecule are inelastically scattered and shifted in a frequency equivalent to the energy associated with a molecular vibration hv_M, as can be seen from Figure 1. This frequency shift can occur to higher or lower energy levels relative to the incident photon. The shift is dependent on whether the photon is incident on a molecule in the ground state or in an excited vibrational state. During ground state interaction, photons lose energy by exciting a vibration, thus the scattered light will appear at a lower frequency v_S, known as Stokes scattering. In the second case, photons interact with molecules in an excited vibrational state, photons gain energy from the molecular vibrations. Thus, an anti-Stokes scattered signal will

occur where the signal appears at higher frequency v_{aS}. It is important to mention that the anti-stoke Raman shift is also responsible for a spectroscopy technique known as, Coherent Anti-Stokes Raman Spectroscopy (CARS) . Raman shifts are generally represented in wavenumber (units of inverse length), where the wavenumber is the difference between the inverse of the excitation wavelength λ_0 and the Raman spectrum wavelength such as,

$$\Delta\omega(\mathrm{cm}^{-1}) = \left(\frac{1}{\lambda_0(\mathrm{nm})} - \frac{1}{\lambda_1(\mathrm{nm})}\right) \times \frac{10^7 \mathrm{nm}}{\mathrm{cm}} \tag{2. 1}$$

The Raman representation in wavenumber, suggests that for all excitation wavelengths the Raman shift will be the same. In a more general view, the Raman scattered signal is an electromagnetic wave which is induced by a dipole moment in the molecule [7]. This dipole moment is generated by the incoming electric field which produces the molecular vibration. The induced dipole will oscillate at the frequency of the incoming field but will also oscillate at different frequencies related to allowed molecular vibrations, creating the Stokes and anti-Stokes side bands.

The Raman process described above takes place spontaneously. Another type of Raman scattering is stimulated Raman scattering, which takes place when Stokes photons that were previously produced or injected through using a second laser enhancing the Raman signal by producing stokes photons faster. In the stimulated case the Raman scattering rate is increased and the pumped photons are more easily transitioned into Stokes photons [16].

In Figure 1b, a schematic representation of fluorescence and RS in a molecule is given, where it can be seen that the fluorescence spectrum is broadband and does not specify structural information about the molecule. On the other hand, Raman scattering probes specific vibrational levels of a molecule. Such levels depend on the atoms, their bond strength and their arrangement in a molecule. Thus, the Raman spectrum provides a specific signature of the molecule and is narrowband spectrum, leading to what is known as the "molecular fingerprint" of a substance. The total Stokes Raman signal $P^{RS}(v_S)$ can be formally written as,

$$P^{\mathrm{RS}}(v_S) = N\sigma_{\mathrm{free}}^{\mathrm{Rs}} I(v_L) \qquad (2.\ 2)$$

where $\sigma_{\mathrm{free}}^{\mathrm{Rs}}$ is the Raman cross section, $I(v_L)$ is the laser intensity, and N is the number of molecules in the probed volume.

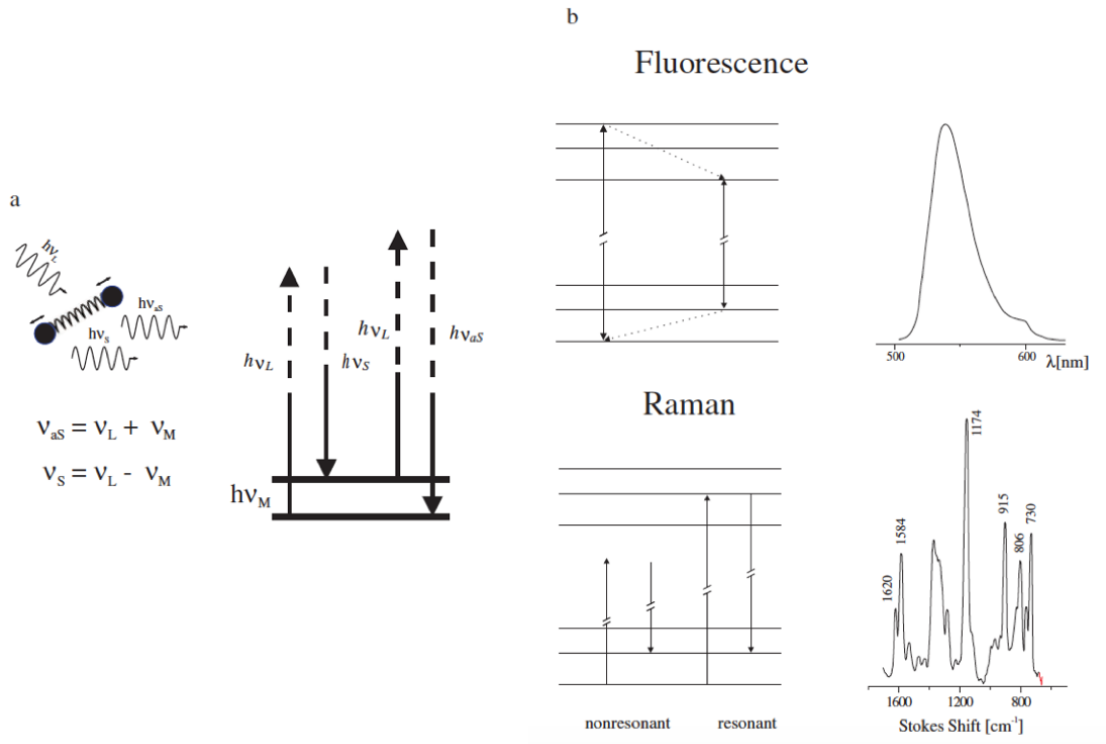

Figure 1 - a) Scattering process between molecule and photon , b) Schematic diagram of Fluorescence and Raman Scattering [7]

2.1.3 SERS mechanisms and SERS enhancement factors

Due to the sensitivity of conventional Raman scattering being fundamentally low, the applications of Raman scattering are limited. Thus, the sensitivity enhancement of SERS resulted in greater application of Raman scattering [17]. SERS occurs when the Raman signal scattered from a molecule is enhanced due to its proximity to a metal surface – enhancements by a factor of almost 10^6 have been observed [18]. In SERS, substrates are covered in metallic nanostructures. It is a phenomenon rooted in the enhancement of the electric field surrounding metallic nanostructures. Initially SERS was observed from rough metal surfaces; however, metal nanostructures have rapidly become of significant interest for SERS applications. This

is due to the fact that nanostructures are much smaller than the wavelength of excitation [19], they produce field enhancement and are controlled by design.

It's important to note that scattering occurs in the enhanced local optical fields of metallic nanostructures, and that molecules interacting with metallic nanostructures involve a new Raman process and cross-section. Specifically, the new Raman process has a larger cross-section than the free Raman process. The SERS stokes power $P^{\mathrm{SERS}}(v_S)$ can be altered to describe the effects of metallic nanostructures as [7]:

$$P^{\mathrm{SERS}}(v_S) = N'\sigma^{R}_{\mathrm{ads}}|A(v_L)|^2|A(v_S)|^2 I(v_L) \tag{2. 3}$$

where $A(v_L)$ and $A(v_S)$ are the enhancement factors of the laser and for the Raman scattered fields. Also, $\sigma^{R}_{\mathrm{ads}}$ is the increased cross-section of the new Raman process and N' is the number of molecules in the SERS process.

The most important property of SERS is the absorption and scattering of light by metallic nanoparticles at a resonant wavelength smaller than that of the exciting light. Without the presence of such particles the enhancement results are not classified as SERS [20]. The enhancement is dependent on the orientation of the SERS substrate with respect to the incident laser polarization and direction. We assume the metallic structure to be a nano-sphere with a dielectric constant $\varepsilon(v)$ and diameter $(2r)$ in a medium with dielectric constant ε_0 as seen in Figure 2. The sphere is a distance d from a molecule which is exposed to a field $E_m = E_0 + E_{\mathrm{sp}}$, where E_0 is the incident field and E_{sp} is the field of the dipolar surface plasmon resonance induced on the sphere. The field enhancement factor $A(v)$ is then given by [7]:

$$A(v) = \frac{E_m(v)}{E_0(v)} \sim \frac{\varepsilon - \varepsilon_0}{\varepsilon + 2\varepsilon_0}\left(\frac{r}{r+d}\right)^3 \tag{2. 4}$$

Similarly, the scattered stokes and anti-stokes will be enhanced if they resonate with the dipolar surface plasmon resonance of the metal sphere. Thus, the enhancement factor of the stokes signal power $G(v)$ considering the enhancement of the stokes and laser fields is given by [7],

$$G_{\mathrm{em}}(v_s) = |A(v_L)|^2 |A(v_s)|^2 \sim \left|\frac{\varepsilon(v_L) - \varepsilon_0}{\varepsilon(v_L) + 2\varepsilon_0}\right|^2 \left|\frac{\varepsilon(v_s) - \varepsilon_0}{\varepsilon(v_s) + 2\varepsilon_0}\right|^2 \left(\frac{r}{r+d}\right)^{12} \quad (2.5)$$

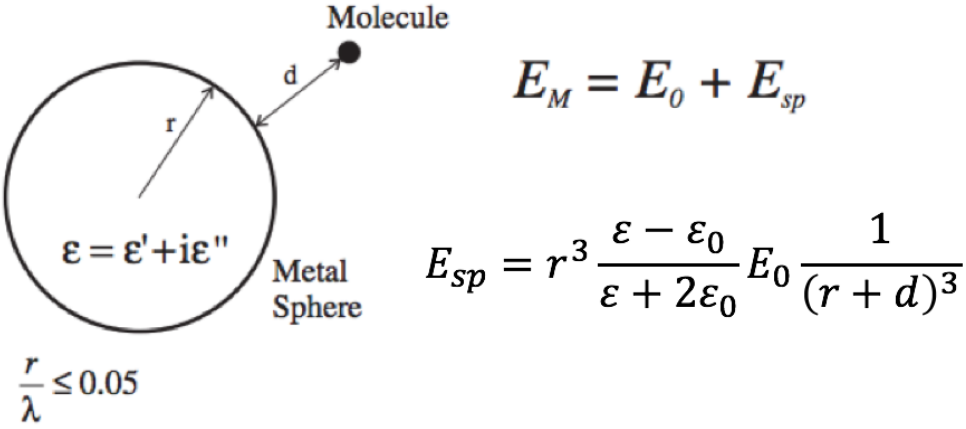

Figure 2 - Schematic diagram of the concept of SERS [7].

2.1.4 Applications of SERS

Despite the fact that thousands of papers have been published in regards to SERS, the development of SERS in applications has been slow due to two main hurdles. The first being that for electrochemical SERS (EC-SERS) only three noble metals provide significant enhancements (Au, Ag, Cu), thus limiting the range of SERS applications [17]. Even though transition metals have a widespread use in electrochemistry applications they have been considered non-SERS active. Almost all of the early studies were performed with pyridine on silver electrodes. Since then however, the effects have been reported on other surfaces such as silver, gold, copper, lithium, sodium, potassium, indium, aluminum, platinum, and rhodium. Silver remains the most efficient and the most studied, however it oxidizes rapidly which can create limitations. The second obstacle is that high SERS-active substrates suffer from instability, leading to poor reversibility during EC-SERS measurements. The reason reversibility is important is it allows one to repeat the measurements on the same area if desired. Thus, making it difficult to correlate the electrochemical data with SERS intensity. In this chapter in a later section it will be discussed why graphene is an appropriate substrate for SERS.

L. Gunnarsson *et al*. investigated the substrate size and geometry dependence of the SERS signal on molecules by fabricating substrates using electron beam lithography. They fabricated arrays of silver structures of different shapes (circular, triangular and square) with sizes ranging between 100 – 200 nm on Si wafers [21]. They performed experiments with Rhodium 6G (R6G) on these surfaces. They used two different excitation wavelengths, 514.5 nm and 632.8 nm. The more suitable one for R6G was 514.5 nm due to the fact that this wavelength is close to being in resonance with the electronic transition of the molecule, thus enhancing the Raman signal. However, the strong absorption of the 514.5 nm beam also leads to an intense fluorescence background, thus decreasing the signal-to-noise ratio.

They observed no enhancement of the Raman signal of R6G on the Si surface or on uniform silver films. It was also clear that the intensity of the signal decreased with increasing separation between the silver particles since they no longer coupled with each other. It was also observed that the peak height was proportional to the silver area or to the number of silver particles in the laser spot. Finally, they concluded that the triangular shaped particles resulted in a higher enhancement than the other shapes due to the presence of corners.

Hongxing Xu *et al*. determined the molecular vibrations in a single hemoglobin (Hb) protein. They achieved results by attaching the Hb proteins to immobilized 100 nm silver particles, thus allowing the use of SERS. They obtained vibrational Raman spectra from the Hb coated silver particles [22]. Single molecule spectroscopy (SMS) has the possibility to identify how an individual molecule reacts to varying outer stimuli. Hence, delivering important information inaccessible in ensemble averaged measurements. In this paper the authors found that the minimal aggregation number for effective SMS is the dimer.

The results indicated that the silver clusters were necessary to observe an effect and that the Hb proteins actually bound the silver particles into clusters. A comparison between calculation and experiment indicates that electromagnetic field effects dominate the surface enhancement, and that single molecule Hb SERS is possible only for molecules situated between Ag particles. The vibrational spectra exhibit temporal fluctuations of unknown origin which appear to be characteristic of the single molecule detection limit. The surface

enhancement factor observed was $M^{\mathrm{SMS}} \approx 10^{10}$ which is mainly due to an increase of the local electric field between the Ag particles.

2.2 Optical Antennas

2.2.1 Introduction

Radio-wave and microwave antennas are structures that transmit and receive electromagnetic waves. Optical antennas, also known as nanoantennas, are a developing type of antenna used in physical optics. They convert the energy of free propagating radiation to localized energy and vice versa [23]. They utilize the properties of metal nanostructures at optical frequencies to control the optical fields at the nanometer scale. This is done to enhance the performance and the efficiency of photodetection, light emission, heat sensing and spectroscopy [23]. The aim of nanoantennas is to optimize the energy transfer between localized source or receiver and the free radiation field.

Optical antennas have similar properties to radio-wave and microwave antennas, however they are preferred in some application due to their nanoscale size and the resonance properties of the metal nanostructures of the antennas [24]. The main goal of an optical antenna is similar to that of microwave and radio-wave antennas which is to enhance the energy exchange between the receiver and the free-radiation field. There is an absence of nanoantennas in technology applications as a consequence of their small size which is of the order of 10 - 100 nm. Such small features require fabrication accuracy down to a few nanometers, which remains challenging but is constantly improving with the development of new machines. The fabrication of nanoantennas has been achieved using nanofabrication tools such as electron beam lithography, ion beam milling and by bottom-up self-assembly schemes. This section will summarize the important properties of optical antennas and their applications.

2.2.2 History

The invention of optical antennas was motivated by microscopy and spectroscopy, unlike radio antennas which were developed as a solution to communication problems. In

microscopy an optical antenna allows the focusing and localizing of laser radiation to dimensions smaller than the diffraction limit. Edward Synge in 1928 proposed the use of colloidal gold particles for concentrating optical radiation on a surface sample, thus transcending the diffraction limit of optical imaging [25]. This was then followed by John Wessel in 1985 who suggested the use of gold particles as an antenna. He wrote "The particle serves as an antenna that receives an incoming electric field" [26]. As a result he became the first to correlate local microscopic light sources and a classical antenna. The discovery of scanning tunneling microscopy and SERS were likely inspired by Wessel's idea.

The first experiment confirming John Wessel's notion of an optical antenna was conducted ten years after the initial statement in 1995 by Dieter Pohl and Ulrich Fischer who used gold-coated polystyrene particles. They imaged a thin film with 320 nm diameter holes and demonstrated a spatial resolution of 50 nm. Another ten years following the suggestion of optical antennas, antenna probes for near-field microscopy and optical trapping using laser irradiated metal tips were proposed. Since then, many geometries of antennas such as rods and bowties have been studied [2].

2.2.3 Antenna Parameters and Advantages

A classical antenna consists of both a receiver and a transmitter connected to a dipole source, as shown in Figure 3. The receiver and transmitter are elemental absorbers or emitters, respectively, such as atoms, ions, molecules, quantum dots or a defect center in a solid that interact with optical radiation through an optical antenna. The antenna also has the ability to modify the emission properties of the transmitter, thus providing a possibility of controlling light-matter interactions on a quantum level. Similarly, the properties of the antenna depend on the receiver and transmitter properties. This section will discuss the different antenna parameters and advantages.

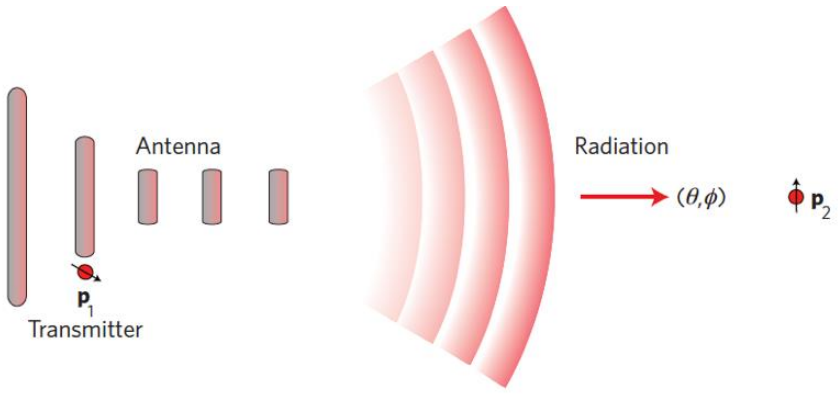

Figure 3 - The transmitter is modelled by the dipole p_1, and the receiver by the dipole p_2 [23].

2.2.3.1 Antenna Efficiency

As previously stated antennas are used to enhance the transmission efficiency from the transmitter to the receiver. Such enhancement is achieved through increasing the total amount of radiation released by the transmitter. For the total power dissipated by the antenna P, the radiated power P_{rad} and power dissipated through the antenna P_{loss}, the antenna efficiency can be written as [23],

$$\varepsilon_{\text{rad}} = \frac{P_{\text{rad}}}{P} = \frac{P_{\text{rad}}}{P_{\text{rad}} + P_{\text{loss}}} \tag{2. 6}$$

An interesting property of the antenna is that the efficiency is the same whether it's a transmitting or a receiving antenna, this property is known as antenna reciprocity. An optical antenna is not just a strong scatterer of resonator but it is defined as a transducer between free radiation and localized energy [23]. With that being said its efficiency can be described as the degree of localization as well as the magnitude of transduced energy.

2.2.3.2 Directivity and Gain

The transmission efficiency can be improved by directing the radiation in the direction of the receiver. The directivity D is the measure of the antenna's capability to direct radiated

power in a specific direction [2]. It is the angular power density relative to an isotropic radiator. The equation can be written as,

$$D(\theta, \varphi) = \frac{4\pi}{P_{\text{rad}}} p(\theta, \varphi) \tag{2. 7}$$

where θ and φ are the directions of observation in spherical coordinates and $p(\theta, \varphi)$ is the angular power density. If the direction is not stated it is often considered that the direction is that of maximum directivity $D_{\max} = \left(\frac{4\pi}{P_{\text{rad}}}\right) Max[p(\theta, \varphi)]$.

The antenna gain G is defined similar to directivity, however instead of normalized radiated power P_{rad} it is defined by relative total power P. More formally:

$$G = \frac{4\pi}{P} p(\theta, \varphi) = \varepsilon_{\text{rad}} D \tag{2. 8}$$

Both D and G can be given in decibels (dB). The gain of antenna is more accurately described as the ratio of the power gain in a given direction to the power gain of a reference antenna in the same direction, due to the absence of isotropic radiators beyond simulations [2].

2.2.3.3 Aperture and Absorption cross section

The aperture of an antenna A is the effective area over which the antenna interacts with the incident radiation [2]:

$$A\left(\theta, \varphi, n_{pol}\right) = \frac{P_{\text{exc}}}{I} = \sigma_A\left(\theta, \varphi, n_{\text{pol}}\right) \tag{2. 9}$$

where P_{exc} is the power incident on the antenna and I is the intensity of radiation from direction (θ, φ) polarized in direction n_{pol}. An antenna increases the optical field in its near-field by gathering field over an effective area. For instance the efficiency of a photodetector can be improved when coupled to an optical antenna [27]. If E_0 donates the field at the target with the absence of an antenna, one can formally write the cross section of the antenna (antenna aperture) as,

$$\sigma = \sigma_o \left| n_p \cdot E \right|^2 / \left| n_p \cdot E_o \right|^2 \quad (2.\ 10)$$

Where, σ_o is the absorption cross section in the absence of an antenna and E is the field of the target in the presence of an antenna, however this is not valid for optical antennas. Here, the superscript 'o' refers to the absence of the antenna. Both σ and σ_o depend on the direction of incidence (θ, φ) and the polarization n_{pol}. Equation (2. 10) suggest that the absorption cross section and aperture correlate to the intensity of the enhancement factor. Experimental studies have proved that an intensity enhancement of $10^4 - 10^6$ is attainable.

2.2.3.4 Effective Wavelength

In microwave antennas elements are proportional to the wavelength λ, thus the scaling of dimensions are easily done based on wavelength. The depth in which the radiation penetrates into the antennas material is called skin depth and is negligible with a relevant length of antenna. The skin depth is orders of tens of nanometers comparable with the dimensions of the antenna. Thus, the classical design rules that dictate the antenna parameters in relation to wavelength are no longer valid in optical antennas since the penetration of radiation into the metal is non-negligible and plasmons can be supported thereon. For a simple nanoantenna structure such as a monopole (rod) or a dipole (two coupled rods), there is an effective wavelength λ_{eff} which is characteristic written as [25],

$$\lambda_{\text{eff}} = n_1 + n_2 \left(\frac{\lambda}{\lambda_p} \right) \quad (2.\ 11)$$

where n_1 and n_2 are constants ant λ_p is the plasma wavelength. This suggests that the optical half wavelength is $\lambda_{\text{eff}}/2$, which is shorter than $\lambda/2$. The difference between the two optical wavelengths is typically between $2 - 5$ fold for most metals.

2.2.3.5 Advantages of Optical Antennas

The main advantage of optical antennas is that they have an aperture that is approximately the square of the wavelength. They also allow the coupling of free radiation to very small volumes with field enhancement [28]. The small volume could be, *e.g.*, an optoelectronic material occupying $0.02\mu m^3$, thus allowing a fast response time. Optical antennas have also proved to be polarization sensitive and can be tuned to a desired wavelength through the manipulation of the geometries [23]. Depending on the design of the metallic structures of optical antennas they can be directionally sensitive. These advantages allow the use of optical antennas in many different applications to manipulate light and control interactions with matter.

2.2.4 Applications of Optical Antennas

Research on optical antennas is motivated by the high field enhancement, large absorption cross-section, and strong field localization. Example applications of optical antennas include antennas for photodetection and photovoltaics. These applications are promising since optical antennas increase the absorption cross-section and consequently the light flux that impinges on a detector, giving it a potential signal-to-noise advantage. Other applications include antenna probes for nano-imaging. This is because optical antennas when used in scanning probe arrangements will result in a spatial resolution on the 10-50 nm scale [23].

There exist many other optical antenna applications such as information processing, to create a super bright single photon source, and for non-linear signal conversion. They offer potential advantages in the detection of light through their polarization dependence, tunability and fast response. They also have the ability to behave as a point detector while being directionally sensitive [23]. Optical antennas have proved to be useful tools for many applications, however the next section will focus on optical antennas used for local field enhancement.

2.2.4.1 Spectroscopy Based on Local field enhancements

The discovery of SERS and scanning tunneling microscopy lead to many theoretical studies targeted at predicting the electromagnetic field enhancement near laser-irritated metals which led to the discovery of optical antennas [24]. A functional antenna interacts strongly with incoming radiation and leads to field localization and enhancement. Such localization is useful for many experimental studies of local spectroscopy such as fluorescence, IR absorption and Raman scattering. The vibrational spectra of Raman scattering define distinctive chemical fingerprint of materials.

As previously discussed Raman scattering cross sections are $12 - 14$ orders of magnitude smaller than the fluorescence of dye molecules making them harder to detect. Thus, to attain a single molecule sensitivity it is necessary to invoke enhancement mechanisms such as resonance or field enhancement. A nearby optical antenna can amplify the Raman scattering by enhancing the incoming and outgoing fields, which allows an enhancement proportional to the fourth power of the field enhancement [24]. Studies have shown that gaps in nanoparticle clusters have a higher than average field enhancement, approximately 10^{14}, which is sufficient to detect a single molecule [29], [30]. Using a well-known antenna can also be used in separating chemical and electromagnetic contributions in the Raman enhancement mechanism.

Another approach to using optical antennas in Raman scattering is by using metal tips for point-by-point Raman spectroscopy, which is known as tip-enhanced Raman scattering (TERS). Using TERS can enhance the Raman signal in the range of $10^4 - 10^8$ as was seen by Anderson and co-workers. Anderson *et al*. used the theory of TERS to study the properties of carbon nanotubes [31], [32]. Similarly Dekert *et al*. studied the significance of TERS in biological material such as DNA and bacteria. Another experiment using TERS in combination with scanning tunnelling was shown by Steidtner and Pettinger to detect a single molecule [24].

2.2.4.2 Optical Resonators

As mentioned, optical antennas have been studied intensively for local field enhancement by simulation and experiment. The simulations can be conducted by using the finite-difference time-domain (FDTD) method to obtain the charge and field distributions on the antenna. Furthermore it can assess the difference enhancement magnitudes with different antenna shape, length and sharpness. Crozier and co-workers fabricated optical antennas using electron beam lithography and found that the experimental efficiencies of optical antenna were in agreement with the FDTD simulation [33]. They showed that the resonant wavelength of the antenna can be tuned by changing the length of the antenna. Mousavi *et al.* used 3D FDTD to investigate gold nano-monopoles and nano-dipoles in a piecewise inhomogeneous background, containing a silicon substrate and a dielectric upper-cladding. They studied the transmission, reflectance and absorption responses of nano-antennas with a change of length, width, thickness and gap [34]. Increasing the length of the antennas red-shifts the resonances of monopoles and dipoles, whereas increasing the width, thickness and gap causes a blue-shift of the responses.

2.3 Graphene

2.3.1 Introduction

Graphene is a 2-dimenstional (2-D) single atom thick sheet of carbon that has gained considerable interest as a consequence of its attractive physiochemical properties and the discovery of an easy method to fabricate and identify the sheets. Some of its properties include the ability to create large area sheets, a high Young's modulus, high thermal conductivity, ease of mass production, and high mechanical strength [35], [36]. Raman spectroscopy is an essential part of graphene research, used to identify the structural characteristics of the material without damaging the graphene layer. It is also used to understand the behavior of electrons and phonons of graphene, the number and orientation of layers (in the multilayer case), the quality and type of the edges, and the effects of perturbation [35], [37]. More importantly Raman spectroscopy is able to identify unwanted byproducts, structure damage, functional groups and chemical modifications [38].

2.3.2 Types of Graphene Samples

Graphene is a 2-D sheet of sp^2-hybridized carbon formed in a lattice honeycomb structure where strong covalent bonds are formed between adjacent carbon atoms [39]. Different types of graphene can exist, it can be stacked to form 3D graphite, rolled to form 1D nanotubes and wrapped to forms 0D fullerenes. Monolayer graphene (1-LG), single layer graphite, contains two carbon atoms A and B which create a triangular 2-D network and are separated by a distance $a_{c-c} = 0.142$ nm as shown in Figure 4a.

The graphite structure is a 3D stacking of graphene sheets in a perpendicular direction (c-axis) to the layer plane in an AB stacking arrangement such that empty centers of a the hexagons on one layer have carbon atom on hexagonal corner sites on the two adjacent graphene layers, as can be seen in Figure 4b [37]. Unlike the graphene sheet in graphite, the unit cell consists of four carbon atoms A_1, A_2, B_1 and B_2 where the A structures are

overlapping in the layers, as shown in Figure 4b where the black circles and dots represent the lower carbon atoms and the grey circles and dots represent the upper carbon atoms. Bilayer graphene (2-LG) structures are similar to graphene where they are stacked in an AB arrangement but only two sheets of graphene are stacked, however they still exhibit the same four atoms per unit cell as seen in Figure 4b and c. Tri-layer graphene (3-LG) structures are a bilayer graphene structure with a third layer that has atoms A_3 over A_1 and B_3 over B_1 as seen in Figure 4d. Similarly, four layer graphene (4-LG) structures are two bilayer structures stacked on top of each other.

In the Brillouin zone (reciprocal lattice) , monolayer and bilayer graphene contain a point at the zone center Γ (Dirac point), the M point in the middle of the hexagon sides, and K and K' points at the corner of the hexagons, as can be seen in Figure 4e. The corner points of the hexagon are not equivalent since they are not connected by the unit vector.

Graphene was mainly produced by mechanical exfoliation of graphite or using a nondiamond precursor material which created multi-layer graphene [37]. Later on samples were made from SiC methods, which resulted in graphene materials that had a significant interaction with SiC substrate, thus resulting in different properties. Recently, more and more experimental procedures are conducted by epitaxial chemical vapor deposition (CVD) growth of graphene on various substrates.

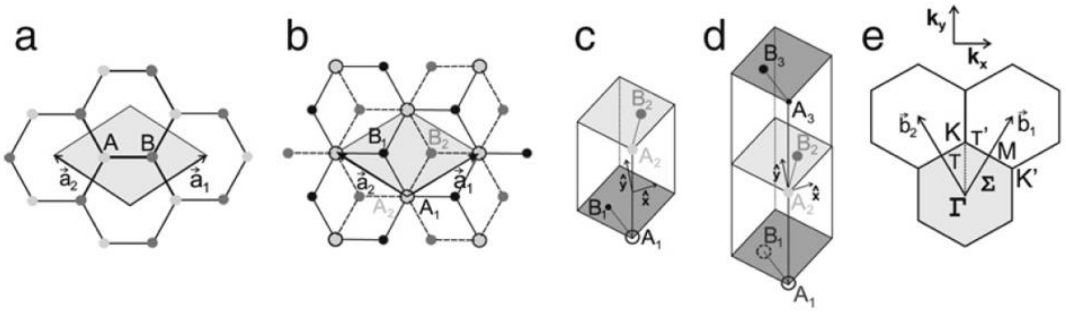

Figure 4 - a)The lattice structure of a single layer graphene with two carbon atoms A and , and unit vectors $\overrightarrow{a_1}$ and $\overrightarrow{a_2}$, b)Top view of bilayer graphene c)The unit cells and the $\hat{x}$ and $\hat{y}$ of bilayer graphene, d) The unit cells and the $\hat{x}$ and $\hat{y}$ of tri-layer graphene e) The first Brillouin zone with points T connecting Γ to K, Σ connecting Γ to M, and T' connecting K to M. Also, the two vectors $\overrightarrow{b_1}$ and $\overrightarrow{b_2}$are shown [37].

2.3.3 Phonon Dispersion of Graphene

The phonon dispersion of monolayer graphene (1-LG) consists of three acoustic branches (A), the movement of atoms of the lattice out of equilibrium, and three optical (O) branches. These branches are due to the fact that monolayer graphene consists of two carbon atoms A and B [38]. A perpendicular atomic vibration to the graphene plane is a result of one acoustic branch, known as out of plane (o) phonon modes [37]. For two acoustic and two optic phonon branches the vibrations are in-plane (i). All phonon modes correspond to two directions transverse (T) or longitudinal (L) which are parallel and perpendicular vibrations respectively in the AB carbon-carbon direction [38]. Thus, along the directions ΓM and ΓK, the six phonon dispersion curves are iLO, iTO, oTO, iLA, iTA, and oTA phonon modes as seen in Figure 5a.

Figure 5b plots the Brillouin zone of graphene and shows the schematic of electronic dispersion. The unique electronic structure of graphene makes it a zero-gap semiconductor (in the undoped state, thus it can be considered a semi-metal). This is due to the conduction and valence bands meeting at the Dirac point. Graphene consists of two atoms and thus six normal modes, two are double degenerate, at the Brillouin zone center $\Gamma = A_{2u} + B_{2g} + E_{1u} + E_{2g}$ [44]. A_{2u} and E_{1u} are the translation planes, B_{2g} is a phonon where carbon atoms move perpendicular to the planes and E_{2g} is a double degenerate in-plane optical vibration and it is the only one to denote Raman activity [40].

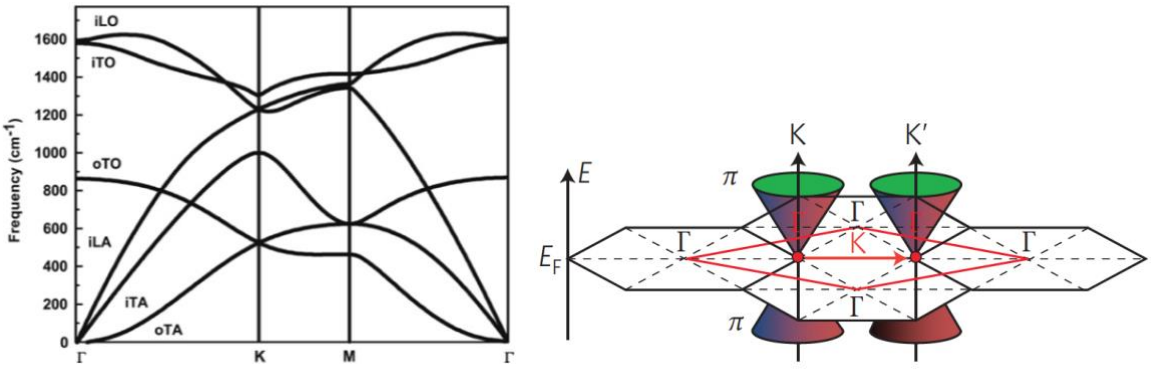

Figure 5 - a) Phonon dispersion modes of graphene [37], *b) Brillouin zones of graphene* [38].

2.3.4 Raman Spectrum of Graphene and Graphite

The graphene layered structures are ideal for studying scanning probe microscopy, however it is required to confirm the graphene thickness and the number of layers, motivating the use of Raman spectroscopy. The most noticeable Raman features of monolayer graphene is the G peak which appears at $1582\ \mathrm{cm}^{-1}$ and the G' (or 2D) peak at approximately $2700\ \mathrm{cm}^{-1}$. In the case of defective graphene or at the edge of a graphene sample a third peak known as the disorder induced D-band at approximately half the frequency of the G' peak appears at $1350\ \mathrm{cm}^{-1}$, and thus will be referred to G' band as 2D from here on [37]. Both the 2D and D peaks display dispersive behaviour. The G peak which is the only one coming from normal first order Raman in graphene is related to the double degenerate (iTO and LO) phonon mode (E_{2g} symmetry) at the Brillouin zone center. The 2D and D peaks are from second order-processes involving iTO phonons near the K points for the 2D band or iTO phonon and one defect for the D-band [37].

The frequencies of the D and 2D peaks in the Raman spectra change based on the incident laser energy E_{laser}. The D band frequency ω_D shifts linearly to higher frequencies with increasing E_{laser} [37]. A double resonance (DR) process generates the dispersive behaviour in the D and 2D bands. The wavevector $\boldsymbol{q}$, associated with D and 2D bands measured from point *K*, would couple preferentially to the wavevector $\boldsymbol{k}$, measured at point *K*, in the DR process such that $q \cong 2k$ [37]. The DR process is seen in the center and on the right side of Figure 6. The process starts with an electron of wavevector $\boldsymbol{k}$ around the Brillouin zone *K* absorbing photons of the energy E_{laser}. The electron is inelastically scattered by a phonon or a defect of wavevector $\boldsymbol{q}$ and energy E_{phonon} to a point in a circle around K' (related to *K* by time reversal symmetry) point with wavevector $\boldsymbol{k}+\boldsymbol{q}$. The electron will then be scattered back to the state $\boldsymbol{k}$ and emit a photon by recombining with a hole at the $\boldsymbol{k}$ state [37].

In the case of the D band, the two scattering processes are a result of one elastic scattering by defects of the crystal and one inelastic scattering by the process of emitting or absorbing a phonon as seen in Figure 6. In the event of the 2D the two processes are a result of inelastic scattering and two phonons are involved, as seen in Figure 6. The DR process connects points in circles around the inequivalent *K* and K' points in the Brillouin zone of

graphene, known as an intervalley process [37]. The intra-valley process connects two points belonging to the same circle around the K/K' point and is responsible for the D' band ($\sim 1620\ \mathrm{cm}^{-1}$). Not all DR processes result in strong 2D and D bands, only iTO and iLO branches are seen in the intervalley and intra-valley processes, respectively. This is due to the phonons strongly coupling to the electrons along the high symmetry direction [37].

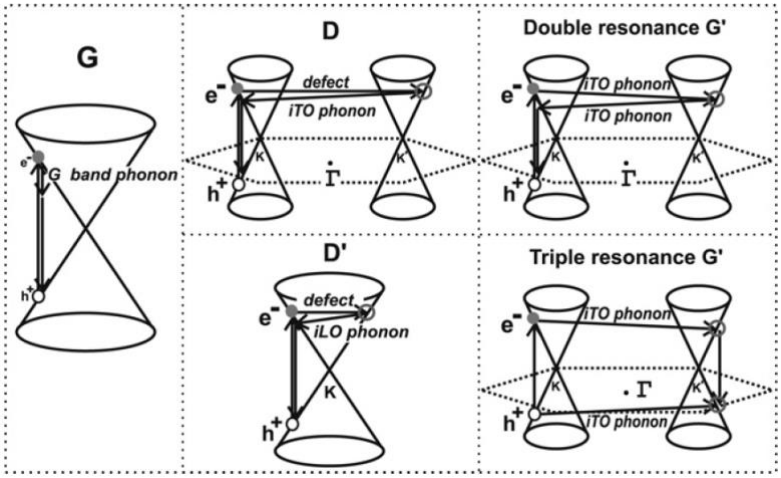

Figure 6 - Left: First order G band; Center top: One phonon second DR process for the D-band; Center bottom: One phonon second DR process for the D'-band; Right top: Two phonon second-order Raman process for the 2D(G') process; Right bottom: Two phonon second-order Raman process for the triple G' process. Resonance points are near the K point and K' point [37].

The graphene 2D band in a bilayer is made up of four components that form a Lorentzian curve. This peak is a result of two phonons with opposite momenta in the highest optical branch near K. Figure 8 shows that this peak changes in excitation and shifts as the number of layers change. This is a result of the DR process that links phonon numbers to the electronic band structures [41]. In a DR process Raman scattering is a fourth order process, requiring 4 transitions,

i. A laser induced excitation of an electron-hole pair, this can be seen in Figure 7a as the transition $a \rightarrow b$.
ii. Exchange phonon momentum q for electron-phonon scattering close to *K*, in Figure 7a as the horizontal transition $b \rightarrow c$.
iii. Exchange phonon momentum $-q$ for electron-phonon scattering close to K', in Figure 7a as the horizontal transition $c \rightarrow b$.
iv. Electron hole recombination in Figure 7a as the vertical transition $b \rightarrow a$.

The condition of DR is satisfied when energy is conserved in the transitions. The exchanged phonon momentum q is determined by the DR conditions and the resulting 2D Raman frequency is twice the frequency of the scattering phonon [37]. Figure 7a and b shows the dispersion along $\Gamma - K - M - K' - \Gamma$. The line transition at the bottom of the figure corresponds to the peaks in the phonon distribution fulfilling DR when the trigonal wrapping is considered.

In the bilayer the interaction of graphene planes causes the π and $-\pi$ band to split into four bands with varying splitting to the electrons and holes as seen in Figure 7b. This results in the incident light coupling more strongly to the two transitions [41]. However, the two degenerate phonons will couple all electron bands. This explains why bilayer graphene has 4 different peaks, the four processes involve phonons with momenta $q_{1b}, q_{1A}, q_{2A}, q_{2B}$ as seen in Figure 7b. Strong phonon dispersion around *K* induced by electron-phonon coupling engenders the four wave vectors of different frequencies [41]. The four corresponding processes have momenta almost identical to the Raman shifts ($0.2\ \mathrm{cm}^{-1}$ difference).

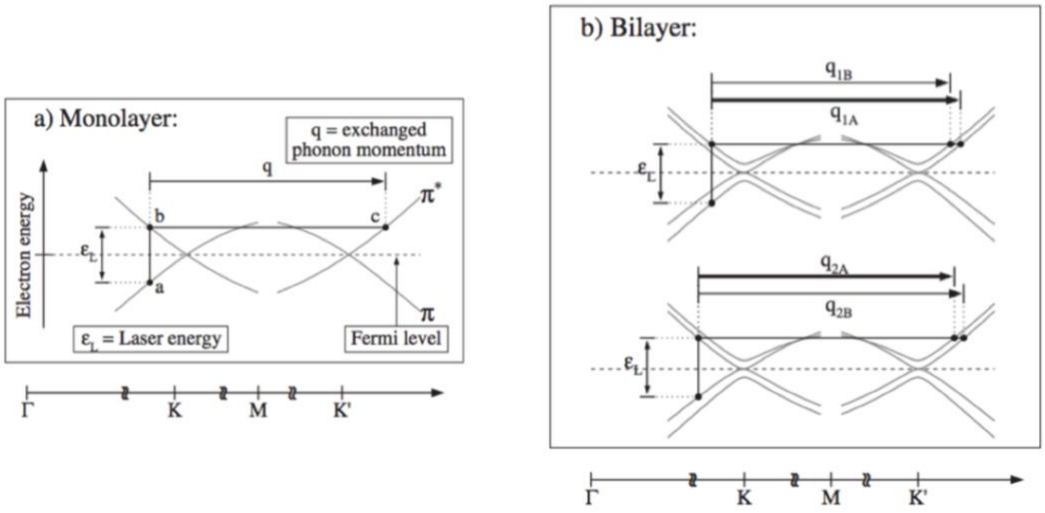

Figure 7 - Double resonance in single layer graphene [41] *https://doi.org/10.1103/PhysRevLett.97.187401*

Observing the Raman spectrum in Figure 8 it is evident that the "fingerprint" of graphene is different than that of graphite. The changes in the G and 2D peaks in terms of peak height and position determine the number of layers. Figure 8a shows that the G peak of a single layer graphene and a multi-layer (more than 10 layers) graphite have a Raman shift of $3 - 5\ \mathrm{cm}^{-1}$ with approximately similar intensity, such shift is a result of chemical doping

[41]. Also at $1350\ cm^{-1}$ the D peak is present in graphite suggesting defect in the structure, it is however not present in the graphene layer thus indicating no significant defects. The measured 2D peak is roughly twice more intense than the G peak. The 2D-peak however shows a significant shape and intensity change from graphite to graphene. The shift in the 2D peak is shown in Figure 8b and c for two different excitation wavelengths as the number of graphene layers changes [41]. This concludes that one can identify the number of graphene layers by observing their Raman spectrum of the 2D-peak.

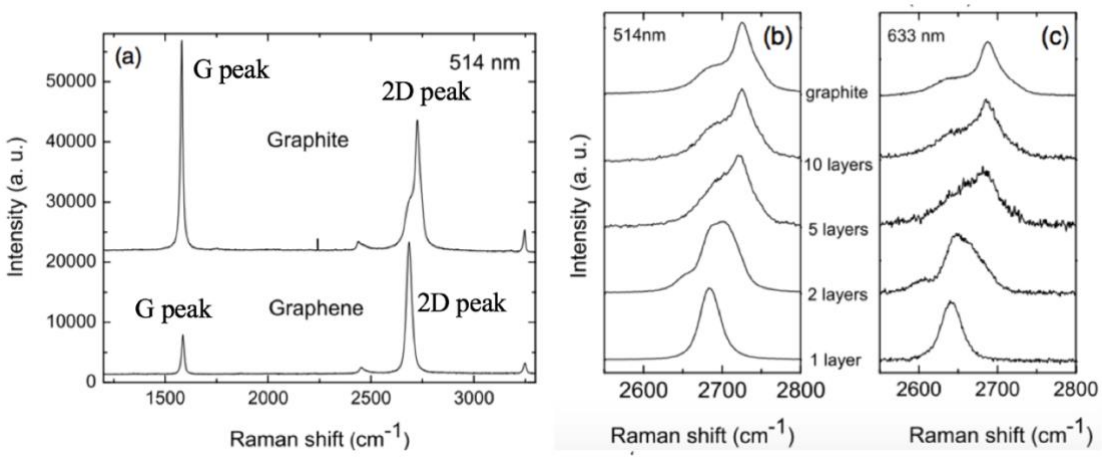

Figure 8 - a) Comparison of Raman spectra with excitation wavelength 514nm of bulk graphite and graphene, b) evolution of 2D peak for excitation wavelength 514nm as the number of graphene layer decreases, c) evolution of 2D peak for excitation wavelength 633nm as the number of graphene layer decreases[41]
DOI:https://doi.org/10.1103/PhysRevLett.97.187401

2.3.5 Graphene Plasmonics

Silicon has been the main material used in electronics and is of strong interest in photonics due to the potential for the monolithic integration of optics thereon. However, not all photonic components can be silicon-based, especially when there is a need for broadband data transfer (*e.g.*, electro-optic modulation or photodetection) and when a wider range of wavelengths is used. This is where the need for graphene is justified. The properties of graphene allow multiple potential functions such as signal emission, transmission, modulation and detection. As previously discussed, graphene has a high thermal conductivity (approximately 36 times higher than Si and 100 times higher than GaAs), high optical damage threshold, and high optical nonlinearities [41], [42]. The behaviour of graphene has motivated research on understanding the dynamics of hot electrons in the material and applications

leading to plasmon attenuation. It can also be used in signal processing, light modulation, sensing, spectral photometry, quantum optics and nonlinear photonics. Graphene plasmons have only been observed at mid-IR and longer wavelengths and only recently have been studied at shorter wavelengths by using noble metal nanostructures [42].

Graphene has powerful plasmonic material due to its unique optical properties discussed earlier but also its ability to be electronically tunable when it is highly doped (through biasing). In the undoped state the excitation of electron-hole pairs in graphene produces a $\sim 2.3\%$ broadband absorption [42].When doped an optical gap opens with an energy proportional to the applied bias voltage. This allows the optical absorption to be controlled by the doping level. The optical behavior of graphene can be controlled by the chemical potential μ and the Fermi level E_F, where the change from dielectric to metallic properties can be tuned by chemical doping and electric gating [42]. Graphene also exhibits high energy plasmons of limited tunability. Tunable plasmons were observed under IR and THz frequencies in graphene, graphene ribbons, disks, rings and holes [5], [42].

The optical conductance of monolayer graphene is independent of frequency in a range of photon energies $G_1(\omega) = G_0 \equiv \frac{e^2}{4\hbar} \approx 6.08 \times 10^{-5}\ \Omega^{-1}$, where ω is the radian frequency, e is the electron charge and the unit of eV (electron- volt), and $\hbar$ is the Planck constant. Due to this, the transmittance of monolayer graphene is also frequency independent and is formally written as [42],

$$T = \left(1 + \frac{2\pi G}{c}\right)^{-2} \approx 1 - \pi\alpha \approx 0.977 \qquad (2.\ 12)$$

where the fine structure constant is $\alpha = e^2/\hbar c$, $\hbar$ and c are Planck's constant and the speed of light, respectively. Graphene presents the strongest broadband absorption per unit mass of any material. The reflectance however is $R = 0.25\pi^2\alpha^2 T = 1.3 \times 10^{-4}$ which is significantly smaller than the transmittance. Thus, graphene can potentially replace indium tin oxide as a transparent conductor.

The conductivity of graphene consists of the complex inter-band and intra-band conductivities, and can be written as,

$$\sigma = \sigma_{\text{intra}} + \sigma'_{\text{inter}} + i\sigma''_{\text{inter}} \tag{2. 13}$$

where the intra-band conductivity and inter-band contributions are,

$$\sigma_{\text{intra}} = \sigma_0 \frac{4\mu}{\pi} \frac{1}{\hbar\tau_1 - i\hbar\omega} \tag{2. 14}$$

, $$\sigma'_{\text{inter}} = \sigma_0 \left(1 + \frac{1}{\pi}\arctan\frac{\hbar\omega - 2\mu}{\hbar\tau_2} - \frac{1}{\pi}\arctan\frac{\hbar\omega + 2\mu}{\hbar\tau_2}\right) \tag{2. 15}$$

and $$\sigma''_{\text{inter}} = -\sigma_0 \frac{1}{2\pi}\ln\frac{(2\mu + \hbar\omega)^2 + \hbar^2\tau_2^2}{(2\mu - \hbar\omega)^2 + \hbar^2\tau_2^2} \tag{2. 16}$$

Here $\sigma_0 = \pi e^2/(2\hbar)$, τ_1 and τ_2 are the relaxation rates associated with the intra-band and inter-band conductivities, respectively. The above equations are associated with the chemical potential of graphene (which can be controlled by chemical doping and electric gating) and the frequency of the incident light. For higher quality graphene there exists no intra-band term since $\mu = 0$ due to the absence of a band gap [5], [42].

Band-filling, blue shift of absorption and gain spectra of semiconductors with increasing the concentration of carries, effects at photon energy is equivalent to transitions that originates from states close to the Fermi surface thus, $2|E_F| = \hbar\omega$ [43]. The optical transitions of graphene can be categorised as, illustrated in Figure 9, :

1) In intrinsic graphene a single photon absorption can take place over a wavelength range from the infrared to the visible.
2) In n-doped graphene a photon with energy smaller than $2E_F$ will not be absorbed because electron vacancies in the conduction bands are unavailable.
3) In p-doped graphene a photon with energy smaller than $2E_F$ will not be absorbed because there are no electrons available in the valence band.

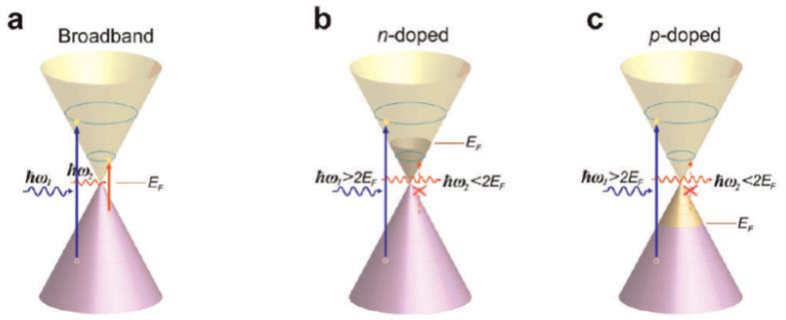

Figure 9 - a)Intrinsic graphene b) n-doped graphene c) p-doped graphene[42]. *Reprinted (adapted) with permission from Q. Bao and K. P. Loh, "Graphene photonics, plasmonics, and broadband optoelectronic devices," ACS Nano, vol. 6, no. 5, pp. 3677–3694, 2012.Copyright (2012) American Chemical Society.*

Noble metals are considered the best available plasmonic materials, however they lack the tunability and possess large Ohmic losses. Graphene however allows waveguiding at infrared and terahertz frequencies of surface plasmons. Graphene having a small chemical potential has a negative σ'' over a large frequency range and thus a semiconductor-like behaviour allowing the guiding of transverse-electric (TE) electromagnetic surface waves. Graphene having a large chemical potential has a positive σ'' and is more metal-like allowing the propagation of transverse magnetic (TM) electromagnetic SPP surface waves, similar to noble metals [5], [41], [42]. The dispersion relation of SPPs can be written as:

$$k_{\mathrm{sp}} \approx \frac{\hbar^2}{4e^2 E_F}(\varepsilon+1)\omega\left(\omega+\frac{i}{\tau_1}\right) \tag{2. 17}$$

The field profile of SPPs on graphene is similar to that of surface plasmons on metal films. The degree of confinement of SPP waves on graphene can be written as [5], [41], [42]:

$$\frac{\lambda_{\mathrm{sp}}}{\lambda_0} \approx \frac{4\alpha}{\varepsilon+1}\frac{E_F}{\hbar\omega} \tag{2. 18}$$

where $\lambda_{\mathrm{sp}} = 2\pi/Re\{k_{\mathrm{sp}}\}$ and λ_0 is the free-space wavelength of light. There are difficulties in exciting and detecting SPP waves on graphene due to the wavevector mismatch between graphene plasmons and free-space photons, as for SPPs on metals, with similar solutions being available (*e.g.*, prism or grating coupling). Recent advancements in graphene photonics include graphene waveguides and graphene photodetectors [42].

2.3.6 Nanostructures on Graphene

Most graphene research has been directed towards the control of its unique properties through doping and electric gating. Metal-graphene interactions have mostly been studied theoretically. However, some calculations (only theoretically) predict that gold will dope graphene in an n-type manner while others have predicted a p-type doping effect [44]. McCreary *et al*. predicted n-type doping for graphene with gold deposition, but p-type doing is predicted from Raman spectroscopy studies of gold-graphene interactions. Others have predicted that Au does not dope single layer graphene but bilayer graphene. Au is the most widely used metal for graphene applications, thus observing the effect of gold on graphene including its nucleation and coverage is essential to understand the interaction of graphene and gold.

One dimensional nanostructures can scatter incident light which in return improves absorption. However, the structures lack conductivity for applications to solar and energy conversion. Thus, the use of a thin layer of graphene can improve the conductivity but also its transparency does not affect the light absorption. Xie *et al*. reported a review on the methods of fabrication and characterization of 1D nanostructures on graphene as well as their efficiency to convert and store energy [45].

Zan *et al*. investigated the structural evolution of gold films evaporated on graphene obtained through exfoliation or chemical vapor deposition (CVD) [44]. They found that initially the size of gold clusters increases as the thickness of deposited Au increases, and beyond 1 nm the gold film merge and its density remains constant. Another way to modify graphene is to dose it using hydrogen and fluorine. Hydrogenation breaks graphene sp^2 bonds and creates sp^3 bonds, thus opening a band gap. However, Zan and collogues noticed that gold does stick to hydrogenated graphene and had better coverage than on pristine graphene. This can possibly be due to the fact that the hydrogenation process takes place mostly in contaminated areas, thus causing gold to adhere more effectively than it would on pristine graphene.

Graphene with metallic nanostructures yields nanocomposites that can serve a range of applications including chemical sensors, energy storage, catalysis and hydrogen storage.

The attachment of metallic nanoparticles on graphene can lead to the inhibition of aggregation of graphene sheets in the dry state. This is done by nanoparticles functioning as spacers between sheets of graphene and thus resulting in accessibility to both faces of the graphene sheet. Goncalves *et al*. conducted experiments that showed that the presence of oxygen on the graphene surface creates reactive sites for nucleation and growth of gold nanoparticles [46]. They were able to grow the gold nanoparticles using chemical methods in an aqueous medium. Furthermore, their studies showed that graphene/gold nanocomposites have the possibility of producing SERS. This was tested with R6G dye molecules using 1064 nm laser source where R6G molecules adsorbed on the nanoparticles yielded SERS signals enhanced by a factor of $10^{14} - 10^{15}$.

Strengthening electron-rich metal nanoparticles with graphene derivatives can regulate the properties of the compound and result in applications in metal-doped graphene field effect transistors, SERS and catalysis. Kamat *et al*. discussed the use of graphene oxide and other metals for application in catalysis [47]. Jasuja *et al*. characterized the interaction of snow-flaked gold nanostructures on graphene using Raman-scattering [48]. They concluded that the gold structures enhanced the Raman signal by a factor of 2.5. It also reduced the band gap from 320 to 173 meV as well as control over the Schottky barrier for the field effect transistors.

Raman spectroscopy is an important technique to investigate the properties of graphene. Li and colleagues compared the Raman spectrum of graphene before and after annealing (applying heat and waiting for a slow cool down to remove stress) [49]. They showed that the D band in the spectrum after annealing was not present and thus no damage to graphene occurred while annealing, while others tend to disagree on this matter. However, it was also seen that the G and 2D bands of graphene shifted to higher frequencies after annealing by approximately $6\ \mathrm{cm}^{-1}$ and $10\ \mathrm{cm}^{-1}$ respectively.

2.4 SERS Studies of Graphene with Metallic Nanostructures

The integration of graphene with plasmonic structures received tremendous attention in the past few years due to the field enhancement with graphene that is enabled when light interacts with nanostructures. Much of the work on SERS has been directed towards increasing the sensitivity of the SERS substrate and enhancing its biosensing abilities by changing its geometry. Scarabelli *et al*. presented the enhancement caused by the self-assembly of nano-triangles which has promising applications [50]. Funston *et al*. used nanorods in different arrangements, separations and sizes, and deduced that the closer the nanorods the better the plasmon coupling [51]. In this section the combination of graphene, SERS and optical antennas will be discussed by examining previously studies.

The main motivators for this thesis work was the work of Ghamsari *et al*. [6]. We aim to replicate this work by building a spontaneous Raman microscope and adding an additional arm to carryout reflectance measurements in situ and eventually investigate stimulated Stokes emission. Ghamsari and colleagues explored the use of SPPs to enhance the graphene-light interaction. They used gold nanorods as nanoantennas in the form of arrays where the nanoantenna length and width were varied, on graphene on SiO_2 on Si. It was found that the different geometries of nanoantennas produce different resonant frequencies, thus providing an array enhancement factor of 2 - 3, approximately, as can be seen from Figure 10. Aside from being able to observe the graphene D, G and 2D peak at $1350, 1570$ and $2700\ \mathrm{cm}^{-1}$ respectively, the silicon $520\ \mathrm{cm}^{-1}$ Si-Si bond peak and the silicon higher-order 2Si peak at around $970\ \mathrm{cm}^{-1}$ are also observed.

Ghamsari *et al*. also discussed the frequency pulling and line shaping of the graphene spectra due to interaction with the nanoantennas [52]. Specifically, Ghamsari *et al.*, showed that the position and linewidth of the G and 2D Raman peaks of monolayer graphene were altered from coupling to SPPs that resonate on nanostructures at the Stokes emission frequencies (and not the pump laser). This is a result of increasing the optical density of states at the Stokes emission frequency. The enhancement of the G and 2D peaks is asymmetric in this case. This asymmetry is a result of the two peaks being approximately 60 nm apart at a pump wavelength of 632.8 nm. Not only did the coupling of SPP resonances with the Stokes

wavelengths change the intensity of the peak but also resulted in frequency pulling and line broadening. The line shapes are not considerably altered when the nanometallic structure resonance lies far from the Stokes wavelength, however the closer the Stokes wavelength is the broader the peak and the more it shifts to lower wavenumbers.

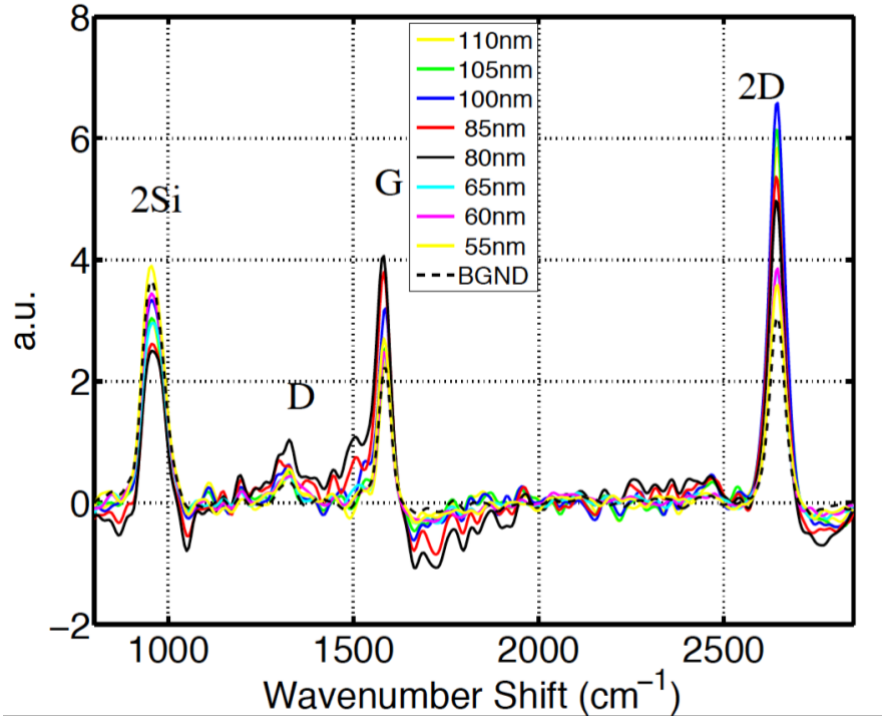

Figure 10 - Raman Spectra of nanoantenna arrays of different lengths. Figure obtained from Behnood Ghamsari with permission to reuse in this thesis [6].

Heeg *et al*. described the graphene Raman enhancement when graphene is suspended between two gold nanodisks and partially extending into the cavity between the disks [53]. They detected an enhancement factor of 10^3 originating from the cavity of the two disks when the cavity was one order of magnitude smaller than the excitation wavelength. This enhancement is a result of the suspension of graphene under tensile strain. However, if the polarization is rotated the two disks are decoupled and the enhancement drops by a factor of 20, which then allowed the probing of strained and unstrained graphene. The suspension of graphene serves two purposes, first the suspension allowed the area of enhancement to be shifted allowing more accurate evaluation and second the local strain resulting from suspension allowed means of local detection. In general graphene can be suspended using various materials, such as silver, and with different nanoparticle geometries, providing different means to locally probe using Raman spectroscopy.

A more extensive study on the effects of cavities or holes for SERS with graphene was conducted by Hao *et al.* (2012) [54]. They used Methylene blue (MB) to study the SERS response of the system that consisted of graphene on and off gold nanoholes. The nanoholes and graphene were placed on SiO_2. Bare graphene showed an enhancement factor of ≈ 16 of MB molecules due to chemical enhancements. However, the combined graphene and nanostructured substrate produced an enhancement factor of 3 to 9 of MB in comparison with bare nanostructures without graphene. Thus, they also concluded that applying graphene to metallic SERS substrates can improve the sensitivity of the substrate since it does not alter the plasmonic properties of nanostructures significantly.

Instead of suspending graphene between two disks, covering graphene with nanoparticles or covering nanoparticles with graphene can be done. Xuanhua Li *et al.* used graphene as a spacer between a silver layer and silver nanospheres on top of graphene [55]. They were able to record one of the highest graphene near field enhancement of 1700 folds to date. This enhancement was a result of the bulk metal and the nanoparticles as opposed to only one or the other. Similarly, Zhao showed that sandwiching graphene between silver nanoparticles and graphene nanoparticles resulted in a very sensitive SERS detection with a limit of 10^{-13} M (molecular level) achieved [56]. Another method of sandwiching graphene was shown by Liu *et al.* where the substrate was bulk silver with an SiO_2 spacer topped by graphene and a silver disk [57]. They were able to achieve a maximum of 70% dual-band enhancement which was a result of the excitation of SPPs and a magnetic dipole resonance on the nanostructure. They were also able to tune the resonance wavelength of the absorption bands resulting from the SPP and magnetic dipole by tuning the array period and changing the diameter of the Ag nanodisks respectively.

Khorasaninejad and colleagues showed that different shapes of nanostructures can yield different SERS spectra for graphene [58]. The plasmonic structures consisted of silver crescent and ring periodic nanoarrays on top of a gold mirror. The mirror is used to move the hot spot to the top of the surface of the silver structures were the graphene lies. They observed that the Raman intensity increased by a factor of 890 for the G-peak of graphene on crescents as compared to graphene on silicon dioxide, which is a result of the electric field being highly enhanced at the corners of the crescent. Also, there was significant enhancement in the 2D-

peak, however not as strong as in the G-peak. The enhancement was different for the two structures studied, where the ring structure showed less wavelength dependence compared to the crescent. They also found that the different diameter of the rings and crescents, and also the different spacing between the structures, resulted in different enhancement factors, possibly leading to additional enhancement due to the plasmonic structures. As one would imagine, the increase in distance between the structures will result in a drop for the G-peak thus demonstrating the strongly confined surface plasmonic fields.

Split-ring resonators (SRRs) are used to produce magnetic susceptibility in various types of metamaterials (materials that do not exist naturally). SRR properties can be tailored to fit a desired application, such as sensing, however they have two main limitations that limit their usefulness. Firstly, the structures (metallic) need to be chemically compatible with molecules in a biosensing application (from instance). Secondly, the vibrational frequencies of the SRR resonances and the target molecules must match thus limiting the size of the SRRs. This resulted in Sarau and colleagues to investigate the possibility of adding graphene to enhance SRRs made of aluminum [59]. They were able to measure a Raman enhancement factor of 75 per area of graphene which indicates strong interaction between the plasmons on the metamaterial surface and graphene.

Modifying SRR structures by adding graphene can produce more transmittance. Novin *et al.* explored different SRR structures by using an 80 nm thick SiN layer as a substrate covered with gold, graphene and SiO_2 nanospheres [60]. They deduced that the asymmetrical formations of antennas resulted in different sensitivities in the X and Y polarizations of the incident beam for antennas without graphene or nanospheres. Furthermore they showed that graphene increased the transmission in the X and Y polarizations which is a predictable behaviour according to the Kubo equations. The presence of nano-spherical surfaces shifted the antenna resonance to higher frequencies. The benefits of graphene in this scenario are: *i*) It acts as a membrane covering the aperture; *ii*) graphene has a useful chemical potential; and *iii*) varying the chemical potential can control the distance between two resonances.

Similar to Ghamsari *et al.* [6] who deposited gold nanoantennas on graphene, Urich and colleagues deposited nano-islands of silver [61]. They observed the same effect of

enhancement of graphene Raman peaks due to localized surface plasmons. The nano-islands resulted in a 100-fold enhancement of the Raman signal. An interesting observation on their part was that prior to the silver deposition process the D-line of graphene was not detected since this is only observed when the graphene has defects. However, after the fabrication process near the nano-islands a more pronounced D-line was detected. This is most likely due to damage caused to graphene during fabrication.

Other work similar to that of Ghamsari and colleagues is the work of Grande *et al.* [62]. They reported the optical response of 2-D periodic arrays of rectangular gold nanopatches on graphene on SiO_2. They found yet again that nanopatches on graphene produced Raman enhancement for the G-peak and the 2D-peak. More interestingly they suggested that the reflection spectrum of rectangular nanopatches produces a polarization-dependent response at normal incidence as opposed to square patches. Figure 11 (a) and (b) show different reflectance responses for a nanoarray as the polarization is changed by 90 degrees, resulting in shifting resonance wavelength. In the same plot they also compared the spectrum of single layer and trilayer graphene compared to no graphene. They found that the higher the number of graphene layers, the more the reflectance of the V and H modes shifted to higher wavelengths. The shift is between $0.5 - 14$ nm, resulting from the fact that the presence of graphene increases the absorption when the field is significantly enhanced on plasmonic resonances. This verifies that the plasmonic resonances are forced to interact with the absorbing layer of graphene. Wei Fan *et al.* attempted to enhance the Raman scattering from graphene by adding a graphene oxide substrate and silver particles [63]. However, they were able to conclude that graphene oxide resulted in a weaker SERS enhancement.

Grande and colleagues discussed briefly that the Raman amplitude at the G and 2D peaks maximize for nanoantennas of different geometries and therefore different resonance wavelengths. The geometry dependence of the transmittance, reflectance and absorptance response of nanoantennas was studied by Mousavi *et al.*, [34]. They found that increasing the length of monopole antennas shifts the transmittance, reflectance and absorptance resonances to longer wavelengths. This shift is in correspondence with classical antenna theory where the resonance shifts to longer wavelengths with increasing antenna length. However, increasing the width of the antennas decreases the resonance wavelength. The physical length l of the

monopole antenna is related to the resonance wavelength of the fundamental dipolar mode λ_{res} but the relationship is not that which would be predicted by microwave antenna theory ($l = \lambda_{\mathrm{res}}/2n_{\mathrm{eff}}$) because of the way in which the optical monopole operates as it appears longer than its physical length as a result of the field extending past the antenna's ends [34]. Thus, Mousavi and colleagues deduced that,

$$\lambda_{\mathrm{res}} = 2L_{\mathrm{eff}}n_{\mathrm{eff}} \tag{2. 19}$$

where n_{eff} is the effective refractive index obtained from modal analysis of the main SPP mode resonating on the nanoantenna, and the effective length L_{eff} is longer than the physical length l. The enhancement mechanism of the Raman signal of graphene suggests that the enhancement relies on the coupling of the G-peak and 2D-peak to the antenna resonance, which was found by Ghamsari *et al.* [6] to be $l = 83$ nm and $l = 108$ nm respectively for a pump wavelength of 633 nm. Raman enhancement due to resonant absorption at the pump wavelength are seen as drops in the transmission spectrum. Finally, it was also concluded that field enhancement depend on the location of excitation on the monopole where the highest enhancement are at the end of the monopole.

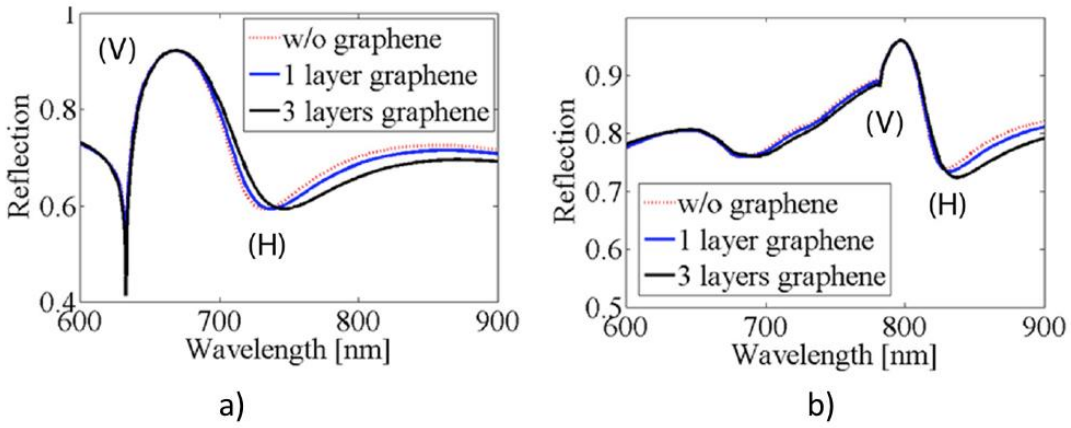

*Figure 11 - Reflectance spectra when the incident polarizations equals a)*0° *and b)*90° *on different number of graphene layers or no graphene* [62]. *Reprinted from [M. Grande et al., "Fabrication of doubly resonant plasmonic nanopatch arrays on graphene," Appl. Phys. Lett., vol. 102, no. 23, 2013.], with the permission of AIP Publishing.*

Chapter 3 – Optical Setup

3.1 Raman Microscopy System: Design and Implementation

3.1.1 Introduction

The transitions between molecular energy levels is a unique characteristic of a molecule. The knowledge of these patterns is generally very useful to identify the type and purity of molecules. Raman technique is a spectroscopic method. Raman scattering describes the inelastic scattering of photons by molecules [64]. The scattered field by a thin film or set of molecules contains reflection and/or Rayleigh scattered fields at the same wavelength as the incident beam plus the spontaneous Raman field at a slightly shorter or longer wavelength (Anti-Stokes/Stokes). By applying two laser sources, stimulated Raman scattering can be achieved, where the first laser source pumps the sample's atoms and molecules into excited states and the second one stimulates emission of a photon and relaxation to a higher mode of the ground state. Stimulated Raman scattering takes place when Stokes photons are injected [16]. This will result in an increase in Raman-scattering rate beyond the spontaneous Raman scattering rate.

The Raman microscope system, shown schematically in Figure 12, focuses the pump laser beam to a very small, ideally diffraction-limited spot, on the sample. The scattered Raman field produced by the sample is then directed to a spectrometer to measure the Stokes shift. A second laser may be employed to achieve stimulated Raman scattering. The spatial distribution of the Raman signal on the sample can be mapped by raster-scanning the sample by a computer-controlled piezo translation stage. Therefore, the Raman signal can be acquired for an array of points, thereby constructing a Raman image.

The beam emerging from the first laser source should pass through an optical chopper to modulate its intensity, the chopper is interchangeably placed between the two source based on the measurements needed. The modulation enables using the lock-in technique, which has been proved highly beneficial for measuring both spontaneous and stimulated Raman scattering with a high signal to noise ratio.

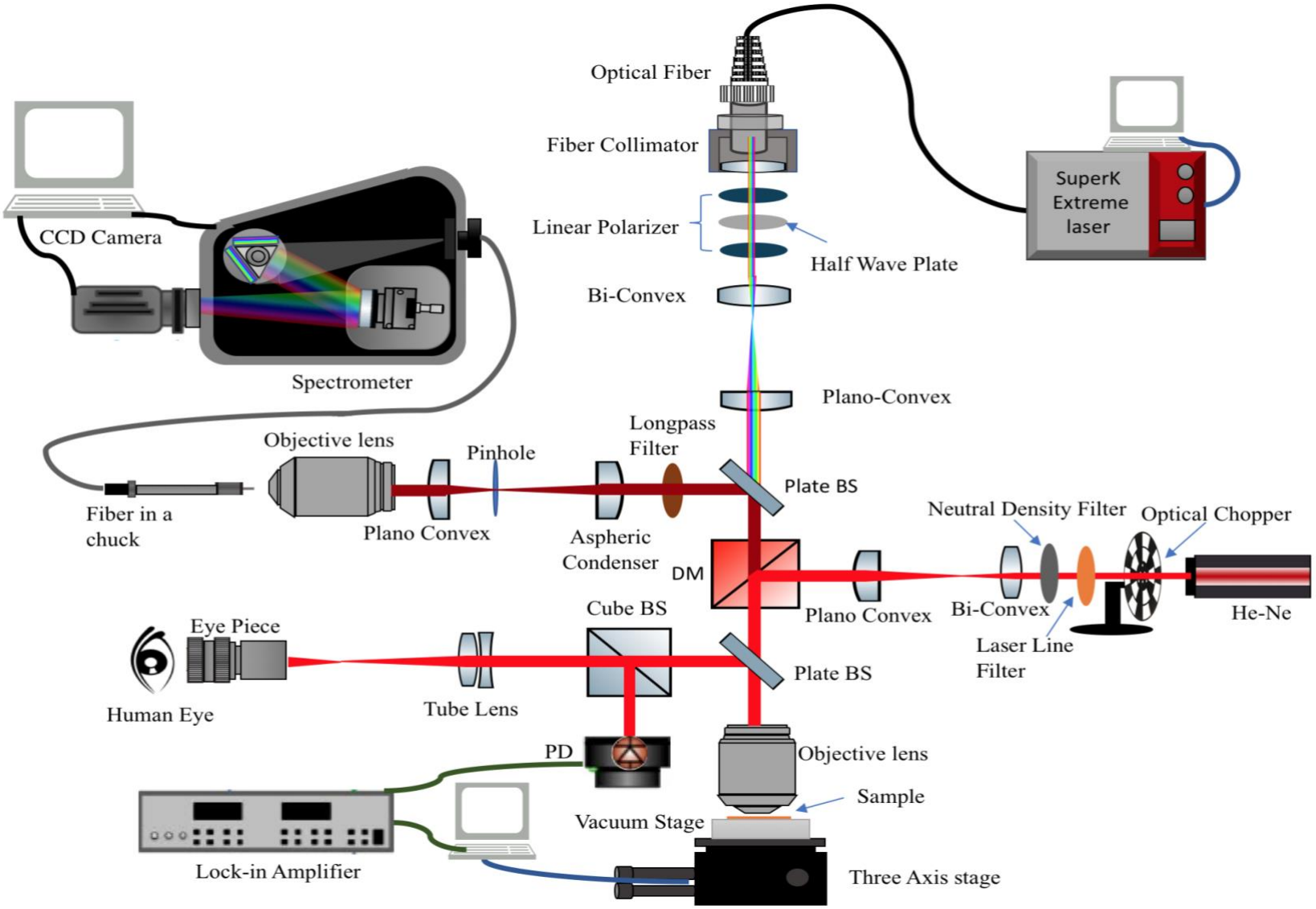

Figure 12 – Complete optical setup. BS: beam splitter, DM: Dichroic Mirror, PD: photodetector

Other means of light modulation, such as electro-optic or acousto-optic modulation, would serve equally well instead of a chopper. To control the system's power throughput, the laser beam is sent through a variable neutral density filter (NDF). The laser beam is then expanded in order to match the size of the objective lens's entrance aperture, the objective lens, in turn, will focus the beam to a small spot on the sample. The size of the focused laser spot is a crucial factor in determining the spatial resolution of the microscope, which is ideally limited by diffraction for far-field probes.

To allow for stimulated Raman measurements with the same system, a dichroic mirror is used between the beam expander and the objective lens to combine the second laser beam into the optical path. Clearly, the second laser should have its own beam expander to again match the objective lens diameter. The objective lens gathers the light reflected and scattered from the sample, including specular reflection(s) of the laser beam(s) and Rayleigh scattering as well as the Raman fields. By adding a beam splitter, half of the collected power is sent towards the spectrometer for spectroscopy and the other half is directed onto a photodetector to measure the sample's reflectance. Acquiring reflectance data along with the Raman data is very useful for interpreting the Raman signal especially from inhomogeneous samples.

The gathered light for spectroscopy is directed into a spectrometry arm by passing through the dichroic mirror used earlier to combine two different lasers. This will separate the beam paths of the pump laser and the Raman signal, the former does not contain any information for Raman spectroscopy but may hinder measurement of the Raman signal due to its much higher power (orders of magnitude higher). To ensure complete rejection of the unwanted pump laser line, a longpass filter is inserted, which allows only the Raman signal to pass.

The system is designed as a confocal microscope to obtain high spatial resolution. This involves passing the Raman signal through a pinhole before sending it to the spectrometer. The pinhole ensures that only the Raman signal from the illuminated point on the sample by the pump laser will contribute to the measured signal in the spectrometer, excluding possible contributions from neighbouring points. Finally, the signal is focused onto an objective lens and coupled into a fiber. The beam's power is then measured at the exit slit of the spectrometer using an intensified charge-coupled device (CCD) camera.

By adding another beam splitter before the first photo-detector responsible for the reflectivity measurements, half the beam goes to the photodetector and the other to the visual access arm. The visual access does not affect the functionality of the system but aids the measurement procedure. It consists of an eyepiece and tube lens. The tube lens focuses the beam converting it to a real object and the eyepiece inverts and magnifies the image for easier visualization. However, the user should always wear proper eye protection such as goggles.

3.1.2 Source and Neutral Density filter

The type of detection device used in the set-up must be considered when choosing a laser for a Raman microscope. Our spectrometer functions at wavelengths less than 900 nm and is a dispersive system. Our intensified camera is based on a CCD array fabricated in silicon which has a detection cut-off wavelength of 1100 nm. Thus, our detection system operates at wavelengths less than 900 nm with a good signal-to-noise ratio (SNR). Systems for detection at longer wavelengths employ nondispersive Fourier transform (FT) detection [65], or a multiplexed spectrometer. Another point to consider when choosing a laser is the output linewidth, which can range from hundreds of reciprocal centimetres to much smaller than $1\ \mathrm{cm}^{-1}$. For Raman spectroscopy a laser linewidth of $1\ \mathrm{cm}^{-1}$ is sufficient.

The laser used in a Raman microscope determines several key aspects of the system's function and design. For instance, it is well-known that Raman scattering intensity varies inversely with the fourth power of the wavelength, $\boldsymbol{\lambda}^{-4}$ [66], [67]. That is, for a given sample, replacing a 1064 nm pump laser with a 532 nm laser (both of which are popular choices for Raman spectroscopy [65]), will increase the scattering cross-section by a factor of 16. This in return means that one requires an acquisition time 16 times longer when using 1064 nm as the pump compared to 532 nm. Such scaling is especially important in the Raman spectroscopy of molecules and thin films, where the scattering cross-section is intrinsically very small. Thus, pumping at shorter wavelengths will, in principle, provide a higher Raman amplitude for a given sample. However, short-wavelength photons can also excite fluorescence in many samples, which in turn can obscure the Raman bands. Therefore, red or near-infrared

wavelengths are widely utilized in Raman spectroscopy, as an acceptable scattering cross-section is accessed while suppressing background fluorescence [65], [66].

There is a variety of laser options to provide coherent light in this range of wavelengths including diode lasers and gas lasers. Gas lasers normally provide stable narrow emission lines [65]. This property is particularly desired for Raman spectroscopy, since the measured spectrum is the convolution of the actual Raman band with the laser lineshape. Gas lasers, furthermore, have very good inherent beam quality, namely single transverse mode beams with low divergence angles. They are also easily convection cooled [65]. On the other hand, diode lasers are very compact and consume less power than most other lasers. However, diode lasers lack the inherent wavelength stability and high beam quality of gas lasers. For instance, their output beams often possess elliptical profiles and are highly divergent, both necessitating some form of beam shaping and collimation. Note that obtaining a high spatial resolution requires diffraction-limited spots, which can be achieved by focusing low-divergence (ideally collimated) beams. These lasers also require temperature stabilization and precise control of the driving current [68], as the output power is directly proportional to the drive current. Strong amplified spontaneous emission (ASE) is another issue with diode lasers which must be suppressed by additional filtering for Raman spectroscopy applications [68], [69].

In a Helium-Neon (He-Ne) laser, the lasing transition is a neon atom. The process of lasing in a He-Ne laser is more efficient than in an ion laser. The Helium ions and electrons carry the current in the He-Ne laser tube and the energy is transferred to the Ne atoms [65]. One disadvantage of He-Ne lasers compared to ion lasers is that the output optical power is much lower ranging from 0.5 to 100 mW at 632.8 nm. The higher the power of the He-Ne the bigger the system; a 50 mW or more He-Ne laser is generally large and inconvenient.

As mentioned earlier an important consideration in Raman spectroscopy is the narrowness of the linewidth of the laser. Since He-Ne is based on gas-phase atoms the output linewidth is sufficiently small and the frequency accuracy is superior. Furthermore, He-Ne lasers also exhibit a variety of atomic emission lines from the DC discharged that need to be filtered out.

Thus, with respect to the attainable spectral and spatial resolution, stability and robustness, ease of use, and cost, a 632.8 nm He-Ne laser was chosen for developing our Confocal Raman Microscope. Due to the small cross-section of Raman scattering, it is advantageous to use laser beams with powers in the range of tens of mW. However, it should be pointed out that a highly focused laser beam can produce very high power densities, which may damage the sample. Furthermore, pumping at 632.8 nm results in Raman scattering in the 633 to 815 nm wavelength range (for graphene) which is sensitive enough for most silicon CCDs [6], [65]. A 21 mW He-Ne laser was selected from Thorlabs (HNL210L). More information on the specifications of this laser are included in Appendix A.

To control the power of the laser input to the microscope, NDFs may be used directly in front of the laser's output aperture. Here a Thorlab NDL-10s-4 filter is utilized, allowing for attenuation in steps of 0.1, 0.2, 0.3, 0.4, 0.5, 0.8, 1, 2, 3 and 4 optical density (OD), which corresponds to a transmittance ranging from 79.43% to 0.01% according to:

$$T = 10^{-\mathrm{OD}} \times 100 \tag{3. 1}$$

where T is the transmittance (in percentage). Note that even after maximum attenuation it is necessary to wear a 7-OD safety goggle to protect the eyes of the experimentalist. The main purpose of the NDF is to reduce the power of the laser in order to protect one's eyes, the sample or sensitive equipment.

3.1.3 Laser Wavelength Filtering

Lasers generally produce light output at wavelengths other than that of the laser line itself. This is more commonly seen in gas lasers ($Ar^+, Kr^+, He-Ne$) because they emit atomic lines (plasma lines), and solid-state lasers, which can interfere with the Raman scattered signal. Thus, the lasers require a bandpass or a laser-line filter to reduce unwanted laser spectra. Although the extraneous emission is a few percent of the total power of the laser, the Raman scattered light is weak and even the smallest amount of non-lasing light from the laser may cause interference, initially this laser was not included in the design but was found later to be essential [65]. The elastic scattering from such emission may be apparent in the Raman

light spectra. Such a spectrum with the use of a mirror in the optical setup is seen in Figure 13 below:

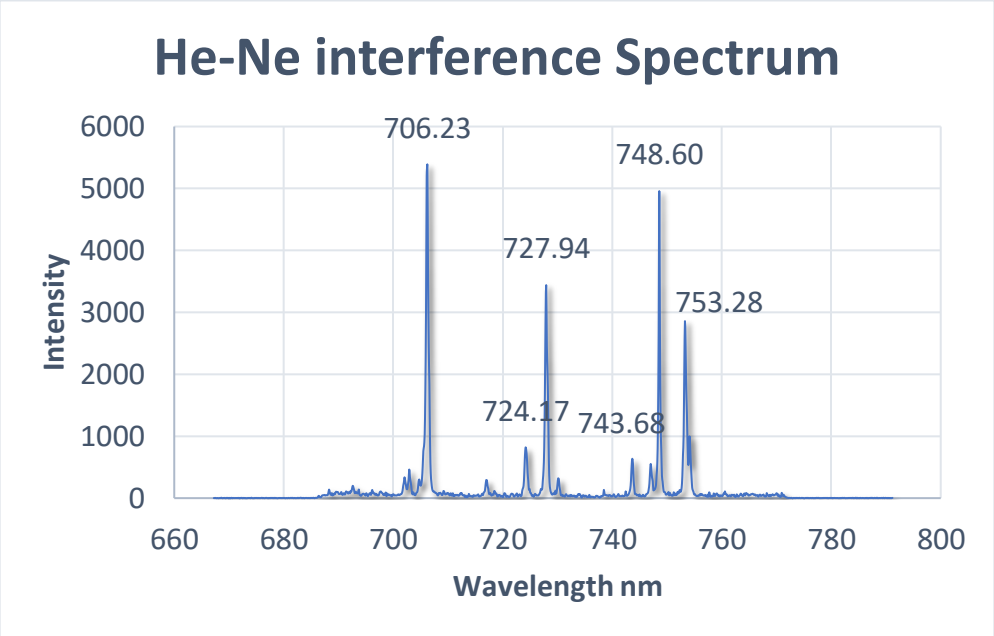

Figure 13 -He-Ne interference pattern near the expected graphene peaks of the system. Data collected from Thorlabs HNL210L He-Ne using Princeton instrument CCDs camera and spectrometer. This spectrum is cleaner with the presence of a laser filter.

A laser/interference filter can remove the interference lines of the He-Ne laser. An OD of 3 is adequate for Raman applications. However, the OD can be increased to a value of 6 by the use of multiple cavities. It is important to have a higher OD level where the Raman shifts are present. Furthermore, the OD away from the excitation wavelength increases with wavelength, meaning it may not function adequately when close to the laser line [65]. The bandwidth of the filter is given as the full width at half maximum (FWHM) of the transmission curves. As the FWHM decreases the peak transmission also decreases, thus creating a tradeoff between maximum laser power and spectral purity.

Interference filters also differ in the maximum power tolerance (damage may occur at high laser powers), and sensitivity to the incident angle. However since the He-Ne laser being used has a power of less than one watt damage is unlikely. The filter used in this application is a laser line filter (Thorlabs FL632.8-3) with a center wavelength at 632.8 ± 0.6 nm and a FWHM $= 3 \pm 0.6$ nm. This filter was chosen since the OD at higher wavelength is closer to 5 and the FWHM is wide enough to make sure the laser power is maximized but not too wide

that it would allow unwanted interference. The transmission and OD data of the filter is given in Appendix B.

3.1.4 Objective Lens

An objective lens is one of the most important optical components that determines the functionality and performance of an optical microscope. The basic design of an objective lens depends on whether the image distance is finite or infinite, and whether a compensating versus a fully corrected system is desired. The ideal diffraction-limited objective generates an infinitely small object point. The diffraction-limited laser spot, whose size depends on the lens' numerical aperture (NA) and wavelength of light (λ), can limit the resolution and quality of an image. For a specific laser wavelength, here λ = 632.8 nm, the diffraction-limited spot size is inversely proportional to the numerical aperture of the lens according to:

$$d_{\text{spot}} = \frac{1.22\lambda}{NA} = \frac{0.771\mu\text{m}}{NA}, \tag{3. 2}$$

where,

$$NA = n * sin(\theta), \tag{3. 3}$$

with n being the refractive index of the imaging environment, usually air, and θ is the half angle of the light cone gathered by the lens, as shown Figure 14.

The resolution (R) of the microscope, which is the smallest resolvable distance between two objects, also depends on the numerical aperture of the lens as

$$R = \frac{\lambda}{2 \times NA} = \frac{\lambda}{2 \times \text{n} \times \sin(\theta)}. \tag{3. 4}$$

Furthermore, the brightness of an image scales with the square of the numerical aperture. Thus, a large numerical aperture is highly desired since it will provide a small diffraction-limited spot diameter, good resolution, and a bright image. The downfall of having a large numerical aperture is a small working distance. The working distance is defined as the distance from the front of the lens to the object. Often, a large working distance is necessary because

the lens needs to be kept at a safe distance from the sample to prevent damage to the sample and lens. Defocusing the objective changes the intensity distribution and size of the image point [70]. It also results in an alternating bright and dark spots (Airy disks). The wave-optical depth of field is the zone of acceptable sharpness in the field plane. A change of depth of field will occur if the image is defocused only $\pm\lambda/(NA)^2$ by moving the sample further and closer to the lens.

The primary role of an objective lens is to magnify the details of the sample under study, thus they become visible to the observer, *e.g.* eye or camera. However, the lens magnification should not exceed the threshold of empty magnification, where further magnification will not increase the resolution [71]. A high magnification will result in a dim image, since the light gathering power ratio of an objective lens is scaled by:

$$\frac{(NA)^2}{(Magnification)^2} \tag{3. 5}$$

Thus, a reasonable choice of magnification is 20X, which allows a good magnification without having a large effect on the brightness of the image.

The focal surface of an imaging system should ideally be a flat plane. Any deviations from a flat focal plane, known as spherical aberration, limits the imaging quality. The image seen through a microscope generally blurred at the edges is an example of the effect of spherical aberration. Spherical aberration occurs when paraxial rays have a different focal length from peripheral rays [70]. Spherically ground lenses will have a focal distance that is shorter for peripheral rays than for paraxial. In order to avoid spherical aberration, a semi-plan or plan objective lens could be used. A semi-plan lens will provide a flat image on the optical axis and becomes less focused and flat further outward, normally producing an image with 80% flatness. On the other hand, a plan objective lens will maintain the flatness over $\sim$95% of the image.

Objective lenses with finite image produce a real image directly. On the other hand, infinitely designed objective require the use of a tube lens for a real image. The quality and resolution of the image improves as the laser spot produced by the objective becomes smaller.

Given a collimated input, this task can be straightforwardly accomplished by using an infinity-corrected objective lens and a large NA as can be seen from equation (3. 2). In contrast to finite objective lenses that map an object to a conjugate real image, an infinity-corrected objective lens maps the object to an "infinitely" distant point in space [72]. Thus, using an infinity-corrected lens focuses the input collimated beam and ensures that the output beam diverges very little with increasing distance. This will allow the beam exiting the lens to be almost collimated. Infinity-corrected lens systems allow the addition of a variety of analytical components to the microscope and provide high-quality images. Infinity or parallel beams are also not affected by the thickness of components inserted to the path as long as they are parallel to the plane field path filed [70]. The alignment between the tube lens and objective remain the same as well as the location of the image point. Thus, an infinity-corrected lens is chosen over a finite lens.

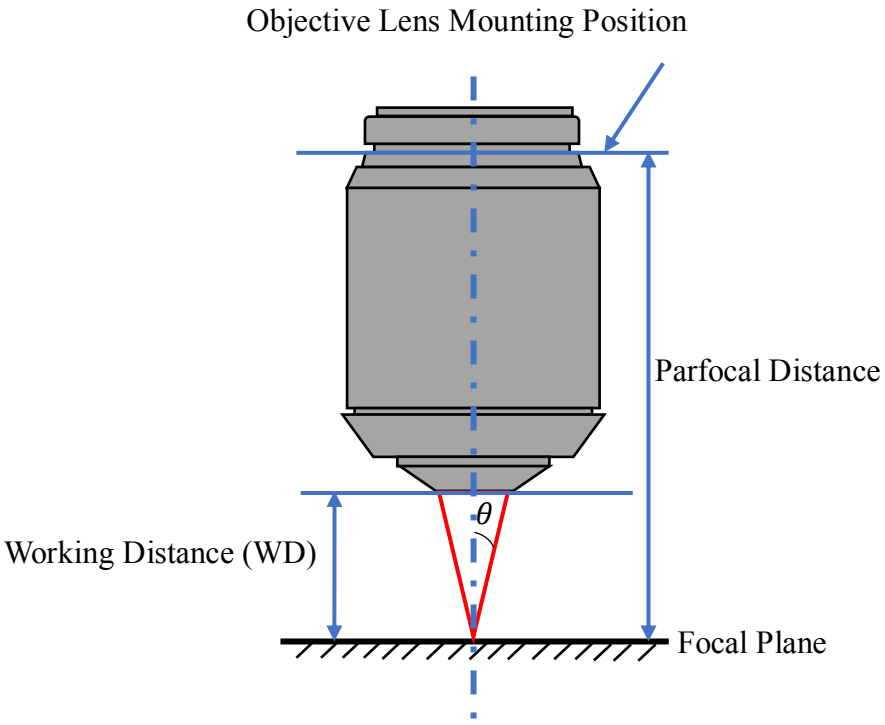

Figure 14 - Objective lens working distance and numerical aperture

Due to the variation of a material's refractive index with wavelength, *i.e.* optical dispersion, the focal point of a lens is displaced for different light colors. This phenomenon is referred to as chromatic aberration, and is another important limiting factor in imaging systems. Chromatic aberration is the wavelength dependence of the objective lens. It is caused

by two factors: 1) The fact that the refractive index for optical glass varies with wavelength, thus the focal point of different colors lies at different longitudinal points on the optical axis and 2) the fact that all colors are focused on the same plane but the focal points are not placed along the same optical axis [70]. The second type of chromatic aberration is only visible at the edges of the first fringes, which can affect the resolution of the image.

There are three major classes of objective lenses with different degrees of correction for chromatic aberration, namely achromat, fluorite (semi-apochromat), and apochromat. An achromat lens is the least expensive and provides chromatic aberration correction for red and blue and single color spherical aberration correction. Similar to an achromat lens, a fluorite lens corrects for red and blue colors for chromatic aberration. However, they also provide two-color spherical aberration correction within the range of the greatest spectral sensitivity for the human eye [73]. In addition, fluorites transmit ultraviolet light more efficiently since instead of glass they are made out of cutting edge glass formulations that are made up of materials such as floruspar (calcium fluorite) or a synthetic replacement. Apochromatic objective lenses provide the highest level of correction for chromatic aberration, and are often much more expensive. They are chromatically corrected for three colors of red, blue, and green, and spherically corrected for at least two colors [73]. Achromat lenses have the smallest NA, while apochromats have the largest possible NA, which in return means a shorter working distance [70]. For Raman spectroscopy and photo-microscopy the lens needs to be able to correct for applications that approach the near-infrared end of the visual color spectrum. Thus, an infinity-corrected plan fluorite objective lens seems an appropriate choice for Raman spectroscopy, providing reasonable balance between quality and cost.

The choice of an infinity-correct plan fluorite lens narrows down the available options of numerical aperture and magnification. The chosen Thorlabs RMS20X-PF objective lens has a magnification of 20X and a numerical aperture of 0.5. This objective is corrected for chromatic aberrations at four wavelengths and spherical aberrations at also four wavelengths. The working distance of the objective lens is 2.1 mm and the input aperture's diameter is 1 cm, producing an ideal spot size of $d_{\text{spot}} = 1.542\ \mu m$ according to equation (3. 2) if the beam fills the entire aperture of the lens. Note, that the working distance is sufficient for the samples used since they are not 3D and are not living organisms either, thus allowing a close distance.

This specific fluorite objective lens is corrected at four wavelengths, has a high signal-to-noise ratio, high resolution and is very efficient in photomicrography.

3.1.5 Beam Expansion

An objective lens achieves the diffraction-limited spot size only if a Gaussian beam entirely fills the input aperture. Under-filling a lens, in general, allows for stray reflections inside the lens which will reduce spatial resolution and the peak intensity. More importantly, since the effective NA of an under-filled lens is less than its nominal value, the obtained focused spot will be larger than the diffraction-limit size. On the other hand, overfilling a lens will partially cut the laser beam. Therefore, the excitation profile on the lens' entrance pupil will no longer be perfectly Gaussian, resulting in diffraction as seen by fringing patterns in the output beam. Because the power distribution of diffracted beams is highly non-Gaussian and they possess high divergence angles, overfilling the objective aperture should be strictly avoided [73]. While filling the objective's aperture by 100% risks cutting the beam due to imperfections and misalignments, 80% coverage is often a reliable design target, albeit at the expense of slightly larger spot size.

There is often a size mismatch between the laser beam output and the objective entrance pupil. In our system, the former is 0.7 mm while the latter measures 1 cm. Therefore, the laser beam should be expanded while keeping it collimated to meet the desired coverage ratio of the objective entrance pupil. Also all lasers have a divergence angle; the HNL210L has an a divergence angle of 1.15 mrad, which can be corrected using a beam expander. A small divergence angle over a small travel distance will not result in a large collimation problem (a beam is never perfectly collimated and a divergence angle of 0 is not achievable in practice).

There are two common methods for expanding collimated beams, namely the Keplerian and Galilean configurations. A Keplerian configuration consists of two positive lenses that are separated by the sum of their focal lengths, as illustrated in Figure 15. In this scheme, a bi-convex lens, where both surfaces are convex, first focuses the incident beam to

a point between the two lenses [74]. As the beam propagates beyond the focus it will diverge and eventually reaches the desired diameter. A plano-convex lens, where one side is convex and the other is plane, is inserted at the other end with the convex side facing the incident light to collimate the beam. The existence of a real focal point in a Keplerian system provides the opportunity of inserting a pinhole in order to remove unwanted higher spatial modes and to align the laser beam to the setup [72]. It should also be pointed out that the resulting beam in this configuration is inverted. Due to the azimuthal symmetry of a Gaussian beam, however, the inversion does not affect the performance of the Raman microscope.

Alternatively, a Galilean beam expander consists of a positive and a negative lens. In this configuration, the negative lens first diverges the incident beam, so that the output beam is originated from a virtual focal point behind the lens [75]. Once the desired beam size is reached, the second lens will again collimate the beam. Here, there is no focal point between the lenses, allowing for a more compact design for the same magnification as the Keplerian design. Nevertheless, the Galilean beam expansion method requires a perfectly collimated beam at the input. The HNL210L laser with its finite divergence angle of 1.15 mrad does not automatically fulfill this requirement of perfect collimation. Moreover, the possibility of inserting an aperture in the Keplerian beam expansion design is beneficial for a Raman microscope. Therefore, a Keplerian configuration is adopted.

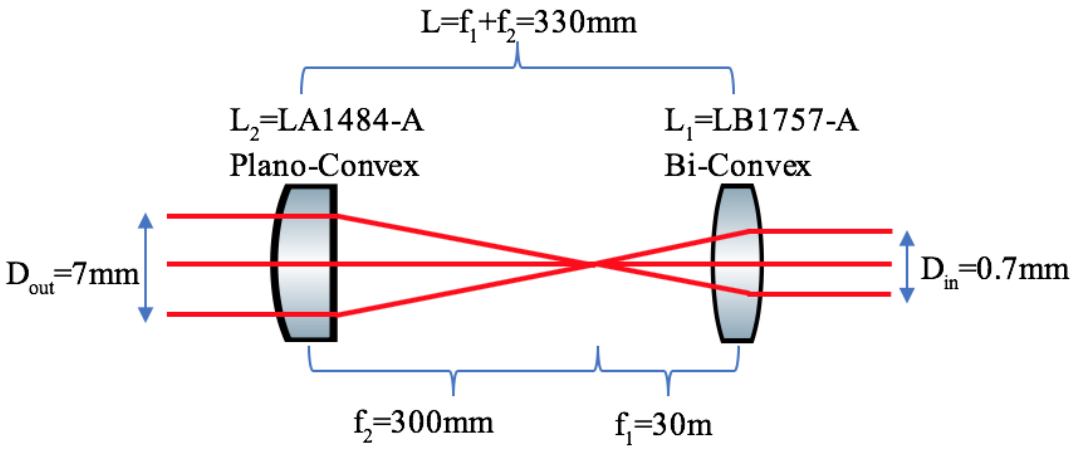

Figure 15 - Keplerian Beam Expansion

In order to expand the beam diameter to approximately 80% of the entrance pupil of the objective lens, the required magnification ratio is

$$m = \frac{D_{\text{out}}}{D_{\text{in}}} = \frac{f_2}{f_1} = \frac{80\% \times 1cm}{0.7mm} = 11.42 \tag{3. 6}$$

where f_1 and f_2 are the focal lengths of the bi-convex and plano-convex lenses, respectively, and D_{in} and D_{out} denote the diameter of the input and output beams. To make the system compact, the shortest possible focal lengths leading to a magnification of 11.42 should be used. Using a bi-convex lens with focal length 30 mm and a plano-convex lens with focal length 300 mm the magnification ratio using equation (3. 6) becomes:

$$m = \frac{D_{\text{out}}}{D_{\text{in}}} = \frac{f_2}{f_1} = \frac{300mm}{30mm} = 10. \tag{3. 7}$$

The distance separating the lenses is, therefore, $L = f_1 + f_2 = 33\ cm$. The accuracy with which the distance between the two lenses is fixed is critical in order or guarantee that the output beam is perfectly collimated. Note, the focal lengths of lenses are limited by what is available from manufacturers.

The new magnification ratio will change the output diameter to approximately 7 mm. This beam diameter is equivalent to filling ~70% of the objective lens aperture, which leaves sufficient margin to avoid beam clamping and provides a theoretical diffraction-limited spot size of $d_{\text{spot}} = 2.2028\ \mu m$ using equation (3. 2).

To implement the Keplerian beam expansion into the setup the laser should be fixed and aligned to the lenses. The first lens, the bi-convex lens, is fixed and the second lens, the plano-convex lens, is moved until near-perfect collimation is achieved. When the distance between the two lenses is greater than 33 cm the output beam diverges very rapidly. On the other hand, if the distance is smaller than 33 cm the output beam converges. The point where the beam doesn't seem to converge or diverge is the point of collimation, which is where the focal points of both lenses coincide. The diameter of a near-perfectly collimated beam is the same whether measured immediately at the output or at a reasonably far distance. The latter will be affected by the finite divergence angle associated with the laser beam. To test the collimation of the beam, mirrors can be used to bounce the beam across the room and achieve a far enough distance. Another method is by using a shearing interferometer (Thorlabs SI100).

Laser alignment could significantly affect the quality and resolution of the reflectivity and Raman spectroscopy measurements. In order to ensure that the beam is perpendicular to the lenses and that the lenses are aligned with each other and the laser, a cage system could be implemented. Furthermore, the He-Ne laser can be mounted into the cage system using a cage system adapter plate. A slight tilt in the laser mounting will be more evident after the beam expansion and even more so when observed through the magnifying objective lens. If there is a tilt in the laser or the cage system the laser beam will not be focused over the whole sample. To further examine if there is a tilt in the setup, at least two irises (apertures) could be used, one in front of the first lens and the other at the very end of the system. This method of testing can be done elsewhere in the setup in front of every element. It is also important to ensure that the lenses are mounted into the cage system with no tilt.

Due to the mismatch between the refractive index of free space and lenses, approximately 4% of the light will be reflected at each surface of the lens. Therefore, uncoated lenses can produce a total light transmission of approximately 92% for visible/near-infrared light [76]. This could lead to ghost images, hazardous reflections, and a reduction in the transmittance of the system. Since this particular system contains many lenses, it is useful to use anti-reflection coatings (ARCs) to maximize the efficiency of light transmittance and prevent the generation of unwanted ghost beams. ARCs will reduce the reflectance of each surface from 4% to 0.5%, which results in 99% transmittance [76]. For a single layer ARC, the index of refraction of the thin ARC film should be equal to

$$n_{ARC} = \sqrt{n_{lens} \times n_{air}}. \quad (3.\ 8)$$

The most suitable ARC spectral range for the excitation arm of the microscope is 350 nm-700 nm since the He-Ne emission occurs in this range.

3.1.6 Beam Routing

A stimulated Raman system consists of two laser sources, a pump laser (He-Ne laser), and a Stokes laser, in our case selected as a super-continuum (SuperK) source with a tunable bandpass filter.Both laser beams are combined using a dichroic mirror (DM), as can be seen

in Figure 16 [77]. The combined beam will then hit the sample after passing through the objective lens. The He-Ne, SuperK and Raman beams will emerge from the sample and propagate to the dichroic mirror. The dichroic mirror has different reflection and transmission properties at different wavelengths, which allow specific wavelengths to completely (~98%) pass through while blocking other wavelengths. Dichroic mirrors separate light spectrally by transmitting and reflecting light as a function of wavelength. A long-pass mirror has a high reflection below the cut-off wavelength and a high transmission above it. Due to the properties of the dichroic mirror (Thorlabs DMLP650R) only the reflections from the SuperK and the Raman signal will pass through the mirror, thus imparting filtering to the reflected beam. The transmission and reflection curves of the dichroic mirror are plotted in Appendix C. The specifications of the mirror are:

Transmission Band ($T_{\text{abs}} > 85\%, T_{\text{avg}} > 90\%$)	685 – 1600 nm
Reflection Band ($R_{\text{abs}} > 90\%, R_{\text{avg}} > 95\%$)	400 – 633 nm

Table 1 - DMLP650R Reflection and Transmission

Where T_{abs} and R_{abs} are the absolute transmission and reflectance respectively, and T_{avg} and R_{avg} are the average transmission and reflectance respectively. For reflectivity measurements a dichroic mirror delivers the highest percentage of laser power onto the sample. Using a crossed-beam geometry for the two beams allows measurement of Raman shifts as small as the sum of two laser linewidths.

Additional beam splitters (BSs) are required to guide the beam into the photodetector, eyepiece and into the spectrometer arm, as can be seen in Figure 16. A beam splitter separates the optical paths of the incident and reflected beams on the sample. There are two common types of beam splitters, the cube and the plate. Due to the structure of a cube beam splitter, it can produce a ghost image that could interfere with the measurements and it can also result in an elliptical beam. On the other hand the beam transmitted from the beam splitter plate will be shifted due to the thickness of the beam splitter, following Snell's law of refraction. This however can be counteracted by using another beam splitter plate in the opposite angle to restore the laser to its original position. The plate beam splitter used here is a 50:50 beam

splitter (BSW26R); the measured transmission and reflectance curves are attached in Appendix D.

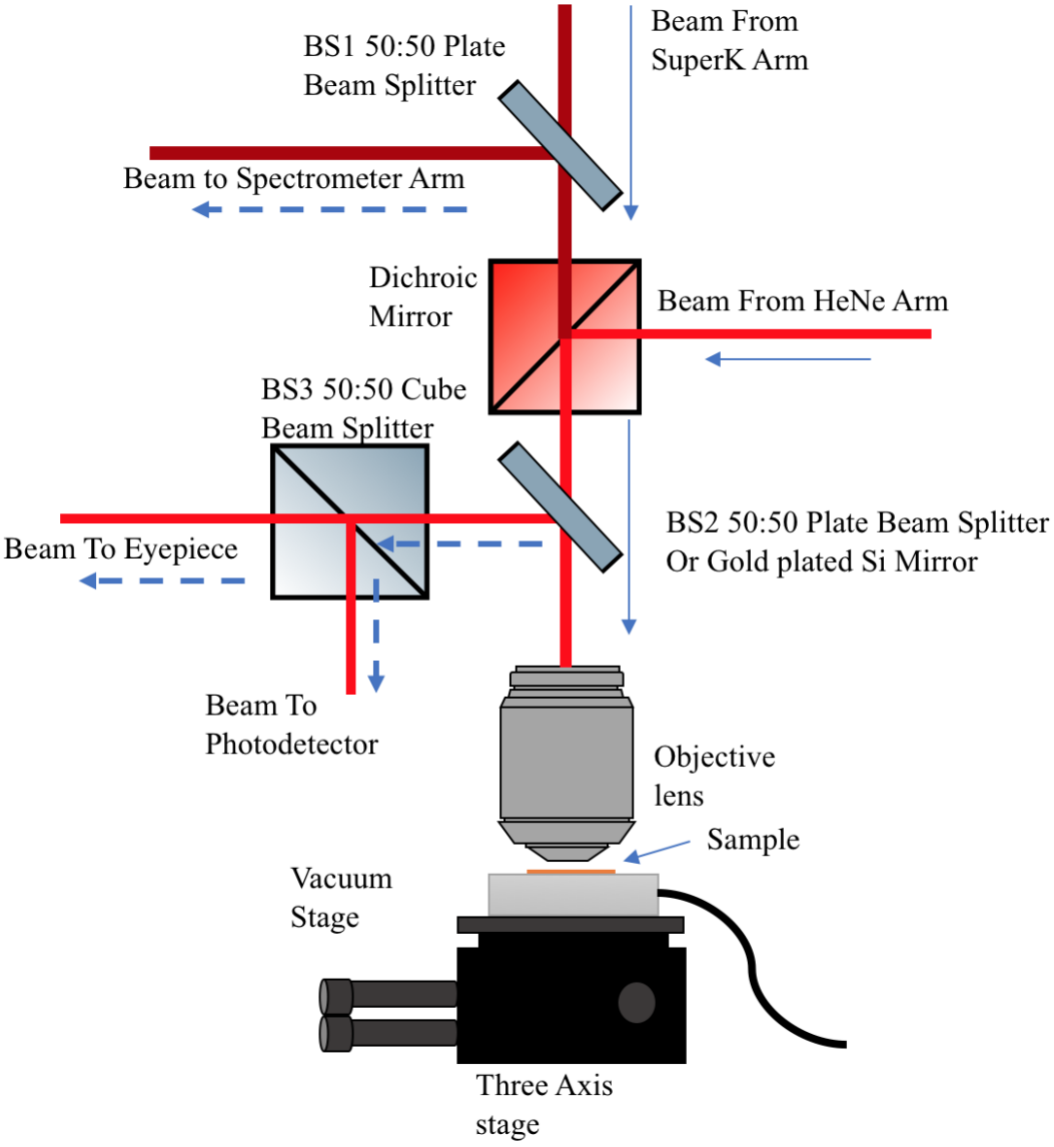

Figure 16 - Beam Routing, Solid lines – Incident beam from SuperK or He-Ne laser, Dashed lines- Reflected Beam for detection

From Figure 16, the routing path of the beam using various beam splitters and a dichroic mirror is sketched. The He-Ne and SuperK beams are combined using the dichroic mirror and then incident on the sample after passing through the objective lens. The beams are then reflected back, as sketched by the dashed arrow in Figure 16, to reach the visual access arm and the spectrometer arm. The visual access arm furthermore splits the beam using

a cube beam splitter for the eyepiece and for the photodetector that is attached to the lock-in amplifier.

The disadvantage of using many beam splitters is that the power collected by the spectrometer or by the photodetector is far less than the original power emerging from the sample due to splitting and dumping some of the light. This poses a problem when trying to find the Raman signal since it is a very weak signal. However, if the spectrometer used is of high efficiency the Raman signal will still be strong enough to be observed. It is beneficial to replace the beam splitter labeled BS2 in Figure 16 with a partial mirror, *e.g.*, a gold-plated silicon piece, when conducting Raman measurements. The reason a perfect mirror is not used instead is to still allow a faint but visible image to be seen through the eye piece, thus viewing and focusing on the sample remains possible. This replacement when needed will double (approximately) the signal routed to the spectrometer arm compared to a beam splitter.

3.1.7 Photodetector

A detector is required to collect the reflectivity measurements as well as the Raman spectroscopy measurements. A photodetector (PD) converts light into current; this is a result of the photons being absorbed in the photodetector. Nonetheless, during the absence of light there is still some current due to the presence of noise. When choosing a photodetector the main concern is the signal-to-noise ratio and the resolution of the signal. For the reflectivity measurements the reflected power is strong, thus easier to collect. Sensitivity plays an important role in the selection of photodetectors. However, in the spectrometer arm the Raman signal is weak, thus needing a more efficient method of gathering the signal. Requirements of the detector include wavelength range of the light, response time and the intensity per unit area.

Photodetectors operate by the transition of an electron from a lower energy level to a higher energy state due to the absorption of photons [78]. Energy transitions are categorized into five types: 1) Photoconductive or photovoltaic: Electrons transition from valence to conduction bands. 2) Photoelectric: Electrons transition from the conduction band to vacuum.

3) Polarization: Electrons transition to virtual energy states as the index of refraction and polarization change. In other words, it uses material that has a polarization sensitive refractive index to detect the photons of a desired linear polarization. 4) Phonon involvement: Electrons reach high levels with the assistance of phonons. 5) Other: Energy is converted to other forms [78].

There are a variety of photodetectors; the most common are photodiodes and photomultiplier tubes (PMT). The photocathodes in a PMT are not uniformly sensitive [78]. This non-uniform behaviour can lead to gain and regional differences in noise and sampling efficiency. On the other hand, a photodiode has uniform sensitivity across the aperture and uniformity will lead to better spatial resolution, *i.e.* minimum separation required to discriminate between two objects. Thus, a photodiode is a suitable choice for our system when it comes to the reflectivity measurements.

Compared to gallium-arsenide and gallium-arsenide-phosphide, silicon has a much better quantum efficiency, ranging from 80 to 90 percent, over the wavelengths of 350 nm to 900 nm [78]. In comparison to other devices PIN silicon photodiodes have the advantage of a higher response speed, lower dark current, lower capacitance, and better linearity. Thus, the lower dark current increases the SNR.

PIN photodiode detectors are ideal because they are cost efficient and easily miniaturized, attributes that are well-suited to our set-up. They are however not as sensitive as avalanche photodiodes (APDs) and PMTs. Photodiodes operate either in the photovoltaic or photoconductive modes. The photovoltaic mode requires a large change of voltage to detect the intensity of light, thus the photoconductive mode is better suited. In the photoconductive mode the increase in the reverse bias current is detected as the photocurrent when a photon is absorbed in the depletion region [78]. Only electron hole-pairs near the depletion region contribute to the photo current. A PIN photodiode incorporates an intrinsic region between doped P and N regions which increases the size of depletion region resulting in a better signal absorption efficiency. Furthermore, it has a lower junction capacitance, reducing the RC time constant, but increases the carrier transit time, which in return limits the response time of the device. Good trade-offs exists between these design goals, although in our set-up speed of operation is not a limiting factor.

The photo-detector selected (Thorlabs PDA100-A) is a silicon-based PIN photodiode for light signals in the spectral range of 400 to 1100 nm, with an electrical bandwidth of 1.5 MHz. This bandwidth is sufficient for our needs (chopped light). It also has internal preamplifier stages with a switchable gain in steps of 7 x 10 dB (low-noise transimpedance amplifier followed by a voltage amplifier). This is especially useful if the signal power is low. This photo-detector also has a $9.8\,mm$ diameter aperture, consequently allowing full beams to be collected. In fact, one of the main reasons a Si APD was not used is due to the small aperture size of the detector thus eliminating the need to use a focusing lens and minimizing the number of required lenses. It is also important to mention that this specific photo-detector was chosen due to the fact that it was available in the lab, however a different photo-detector might be just as efficient. The responsivity of a photodiode can be calculated by finding the ratio between the photocurrent (I_{PD}) and the incident light power (P), written as:

$$R(\lambda) = \frac{I_{\mathrm{PD}}}{P} \tag{3. 9}$$

The responsivity curve versus wavelength of the detector selected is given in Appendix E (range of 0.3 - 0.6 A/W). This photodetector is used for reflectance measurements in our set-up.

The Raman signal is too weak to be collected by the PDA100-A detector. The signal power is in the same range as the noise in the detector thus making it unidentifiable. An intensified CCD camera is used in the spectroscopy arm that can detect down to single photons. This is further discussed in Section 3.1.11.

3.1.8 Lock-in Technique and Light Modulation

In addition to using a low-noise photodiode, a lock-in technique is utilized to enhance the SNR even further. In theory, a lock-in amplifier measures the amplitude of a sinusoidal wave V_0:

$$V_{\mathrm{in}} = V_0 cos(\omega_0 t) \tag{3. 10}$$

where $\omega_0 = 2\pi f_0$. To be able to extract a signal from the lock-in amplifier a reference input voltage is used which is synchronized with the source light. This allows the lock-in amplifier to collect any signal that is synchronized with the modulation and ignore anything else.

In the lock-in amplifier used (Scitec Instruments Ltd. 420 dual lock-in), the noise power is equal to the noise power density times the measurement bandwidth. The noise power density is a result of shot noise which is set by the detector, but the bandwidth of the signal can be controlled. The He-Ne laser beam is intensity-modulated using a chopper (model SR540 chopper controller), and the PD signal is sent to the lock-in amplifier. A narrow-band filter is placed around the reference frequency, *i.e.* the chopper frequency, to limit the bandwidth. The chopper operates at frequency in the range from 400 Hz to 3.7 kHz (specifications given in Appendix F).

The higher the reference frequency the more noise the lock-in amplifier can filter. This is due to the fact that in order to separate noise components from signal it needs to be modulated at what is known as a signal frequency, thus allowing the signal to have a different frequency than that of noise. The lowpass filter which follows the multiplier can consequently reject any frequency components that are more than a fraction of a Hertz away from the signal frequency, thus removing the AC components from the signal. The lowpass filter also serves to narrow the bandwidth of the amplifier. The block diagram of the lowpass filter is seen in Figure 17 [79]. The input amplifier is a voltage amplifier combined with some other filters.

The remaining blocks in the diagram of Figure 17 allow the enhancement and detection of the signal. The reference signal provides the reference frequency and the phase shifter allows synchronization in phase of the reference with the input signal. The phase sensitive detector is a multiplier circuit ($V_{\mathrm{sig}} \otimes V_{\mathrm{ref}}$). Finally the output amplifier is a low frequency amplifier.

The lock-in amplifier is a voltage amplifier and in combination with the photodetector produces an output proportional to the intensity of incident light. It produces a very narrowband signal which automatically follows small changes in the modulating frequency [79]. The optical input is fed to the photodiode as a chopped square signal. The changeable time constant of a lock-in amplifier is the time constant of the lowpass filter τ. Consequently,

the bandwidth of the lowpass filter is BW = 1/(τ). For a low time constant the voltage will respond quickly to changes but it will not be as stable as it is for a larger time constant. Therefore, the time constant should be adjusted to provide a stable and rapid reading. The longer the data collection delay of the lock-in amplifier the better the quality of the signal. The data collection delay should be at least 1.5 fold larger than the time constant. In other words for a 10 ms time constant the data collection delay should be 15 ms. Clearly, the higher the time constant the better the resolution of the signal. Nevertheless, for 100 ms to 300 ms time constants the system yields adequate reflectivity measurements without a large data collection delay time.

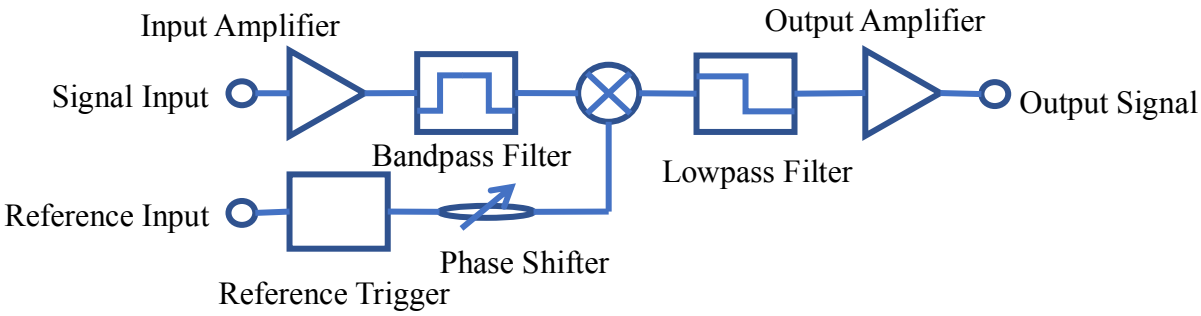

Figure 17 - Lock-in Amplifier block diagram (420 Dual Phase Lock-in)

The gain and sensitivity of a lock-in amplifier are inversely proportional, *i.e.* Gain = 1/Sensitivity. Thus, the higher the sensitivity the smaller the gain. Furthermore, it's important to make sure that the gain is not oversaturating the signal, which could result in a signal cut-off. The lock-in amplifier converts an AC signal into a DC signal using an adjustable narrow bandpass filter. This will result in a phase sensitive bandwidth detection by reducing the phase content falling outside the interest of the bandwidth. The bandpass also modifies the response of the unit so it only detects signals at the reference frequency.

There are two channels in the lock-in amplifier that produce the output. They are in the form of x and y voltages, where

$$X = V_{\text{sig}} cos\theta \tag{3. 11}$$

And,
$$Y = V_{\text{sig}} sin\theta \tag{3. 12}$$

assuming there is no noise or signal shifts The magnitude of the reflectivity R is proportional to V_{sig}:

$$R \sim \sqrt{X^2 + Y^2} = V_{\text{sig}} \tag{3. 13}$$

and,
$$\tan(\theta) = \frac{Y}{X} \tag{3. 14}$$

The values of X and Y should not exceed $\pm\, 1V$ since that's the maximum voltage for the lock-in amplifier, or else the output will be over saturated. After the signal is produced by the lock-in amplifier it is collected by computer data acquisition (DAQ) card for further processing as will be discussed in Section 3.2, Appendix G and Appendix H.

3.1.9 Visual Access

To complement the Raman microscope with visual access to the sample, which is required for alignment to the focused laser spot, a viewing microscope is constructed using the existing objective lens by utilizing a tube lens and an eyepiece as can be seen in Figure 18. When the He-Ne laser is collimated, after passing through beam expansion as described in Section 3.1.5, it is focused using the infinity-corrected objective lens. The laser beam exiting the entrance pupil of the objective lens is collimated, so a tube lens is used to focus the beam and convert it into a real image.

The infinity-corrected property of the objective lens does not limit the focal length of the tube lens because the beam is collimated, so the tube lens can be placed anywhere along the beam at any desired distance without affecting the magnification of the image. Nevertheless, a longer focal length will result in a much taller microscope making it harder to use. The image produced by the tube lens is inverted, thus an eyepiece is used to correct for the inversion. The eyepiece provides further magnification of 10X to the sample without affecting the brightness of it. The distance between the eyepiece and the tube lens is the sum of their focal length as that of the Keplerian beam expansion where the two focal points meet

in the middle. The achromat doublet lens AC254-200-A is suitable as the tube lens for it adequately corrects for chromatic aberration and has a focal length of 200 mm.

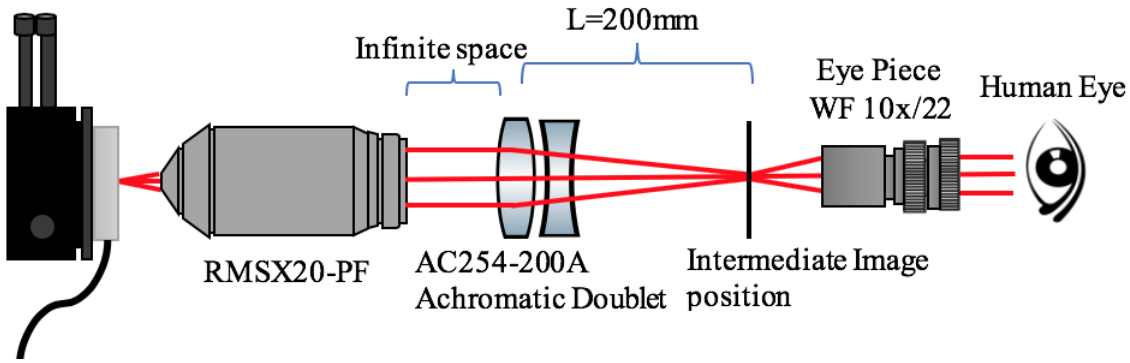

Figure 18 – Visual Access Arm

It is essential to align the focal point of the objective lens with that of the eyepiece in order for the microscope to function properly. First, the exact focal point of the objective lens is found. This is done by placing a mirror under the objective lens instead of the sample. If the mirror is 2.1 mm away from the objective lens (working distance of the latter), then the focal length and object distance are the same. This can be seen using the image formation equation,

$$\frac{1}{f} = \frac{1}{q} + \frac{1}{p} \tag{3. 15}$$

where f is the focal length, p is the object distance and q is the image distance [72]. For a collimated laser beam the image distance q is infinity thus, $p = f = 2.1$ mm. Additionally, the magnification factor is $m = \frac{p}{q} = 0$. It can be observed that the beam size shrinks when the mirror is brought close to the lens until it reaches a point where it expands again. When the beam is collimated the tube lens is added to the system and the focal point of the objective lens is aligned to that of the eyepiece. The distance between the tube lens and eyepiece is the sum of the two focal lengths. With some eyepieces that consists of many lenses the focal point of the system is inside the eye piece.

3.1.10 Supercontinuum Arm

Making the system functional in stimulated Raman measurements requires a pump laser and a secondary source tunable to different wavelengths to coincide with the Stokes wavelengths. The secondary source used here is a supercontinuum source with a tunable bandpass filter (NKT photonics SuperK Extreme Supercontinuum Laser). The supercontinuum produces white light and tunable bandpass filters covering a range of wavelengths from 400 to 1800 nm are available. For the purposes of stimulated Raman in graphene and to measure reflectance responses, a wavelength in the range of 500 to 1100 nm is required. This requires two acousto-optic tunable filters for the supercontinuum: the first covering a range from 400 to 700 nm and the second from 640 to 1100 nm. It is important to note that near the end of the range of an acousto-optic tunable filter the beam quality degrades. Furthermore, the beam characteristics including power and diameter change with wavelength. As a result, the system is optimized in the midpoint of the range and further optimized at various points as needed. The beam is coupled into a polarisation-maintaining single-mode optical fiber. The specification of our fibers are:

Fiber ID	Wavelength Range	Mode Field Diameter (MFD)	NA	Measured at wavelength
FD4-PM	750-1100 nm	5.3 µm	0.12	850 nm
FD1-PM	450-800 nm	3.8 µm	0.12	630 nm

Table 2 - Fiber Specifications

The main purpose of the supercontinuum arm is to deliver a linearly polarized and collimated beam to the sample through the objective lens to conducted stimulated Raman and normalized reflectance measurements. However, there are two problems to solve before sending the beam to the objective lens. Firstly the beam should be linearly polarized in the same orientation as any nanstructures on the sample (*e.g.*, nanoantennas), and secondly the beam should cover approximately 90-70% of the objective lens surface.

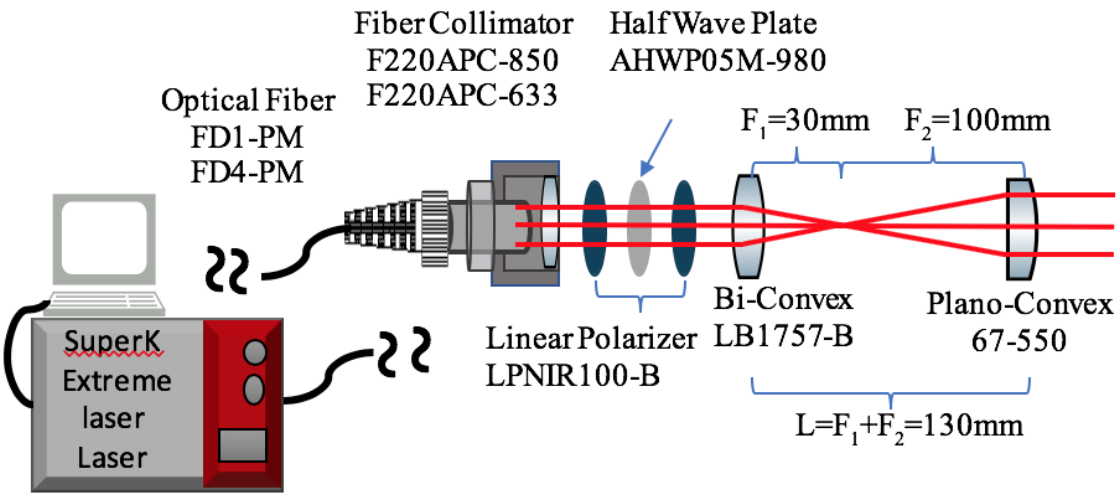

Figure 19 - Super-Continuum Arm

To tackle the issue of polarization a set of polarizers and a half-wave plate are used as can be seen in Figure 19. The first difficulty with the polarization is that the orientation of polarization of the beam exiting the fiber is not precisely known. Thus, the desired polarization is set and fixed using the first polarizer, horizontal in this case, and the fiber is rotated until maximum power is observed from the output of the polarizer. As see in Figure 20, a half wave plate with fast (F) and slow (S) axes as indicated is sandwiched between two polarizers. After fixing the first polarizer the half wave plate is mounted on a rotating mount. The rotations of the mount causes the polarization to rotate to twice the angle of the half wave plate. Thus, a 90º polarization rotation is achieved by rotating the plate in a 45° angle to incoming beam. Finally, the last polarizer is used to further guarantee that the output beam is polarized in the desired direction. Having the half wave plate and the second polarizer in a rotating mount allows the polarization of the beam to be easily changed. The Jones matrix of such a system [80], [81] is:

$$E' = \underbrace{\begin{pmatrix} 0 & 0 \\ 0 & 1 \end{pmatrix}}_{Second\ Polarizer} \overbrace{\begin{pmatrix} \cos\frac{1}{2}\Gamma & -i\sin\frac{1}{2}\Gamma \\ -i\sin\frac{1}{2}\Gamma & \cos\frac{1}{2}\Gamma \end{pmatrix}}^{Half\ wave\ plate\ with\ retardation\ \Gamma} \underbrace{\frac{1}{\sqrt{2}}\begin{pmatrix} 0 \\ 1 \end{pmatrix}}_{\substack{Polarized\ light \\ after\ first\ polarizer}} \tag{3. 16}$$

$$= \frac{1}{\sqrt{2}}\begin{pmatrix} 0 \\ \cos\frac{1}{2}\Gamma \end{pmatrix}$$

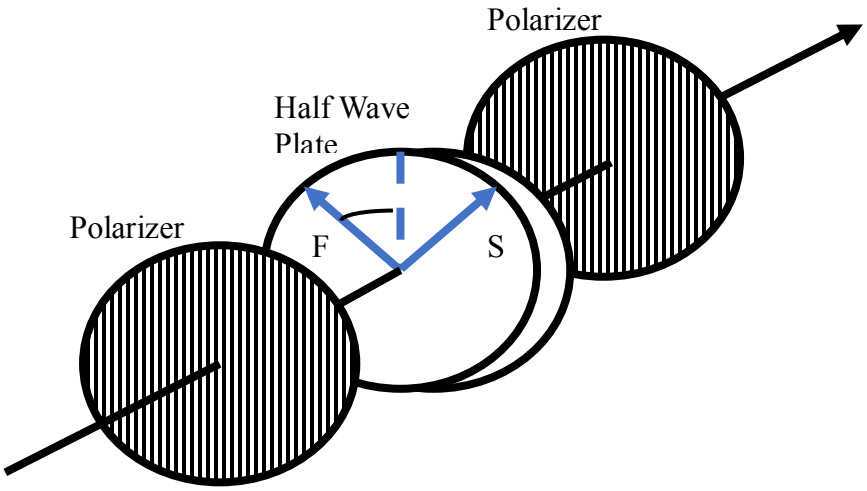

Figure 20 - A half wave plate sandwiched between a pair of polarizers

One must note that the choice of the half-wave plate is limited by the cost and the market available half-wave plates. In this case an ideal half wave plate would have been the Thorlabs SAHWP05M-1700 since it works for a wide range of wavelengths. However, it is 3 times more expensive than the one chosen and the one used still provides satisfactory results for the current work.

As discussed in Section 3.1.6, a dichroic mirror is placed between the primary light source (He-Ne) arm and the supercontinuum arm to combine the two beams. Similarly, to the primary light source arm the supercontinuum beam should be expanded to cover at least 80% of the objective lens aperture. The beam from the supercontinuum is coupled into an acousto-optic tunable filter, which is then coupled into a fiber (FD1-PM or FD4-PM depending on wavelength). The beam from the fiber has a large divergence angle thus a fiber collimator is needed. The numerical aperture of the NIR and IR fiber is 0.12, making the acceptance angle of the fiber [82]:

$$\theta_a = \sin^{-1} NA = 0.1202\, rad \tag{3. 17}$$

The divergence angle is:

$$NA = 0.12 = n \sin \theta_D \;\; \rightarrow \theta_D = 4.753° \tag{3. 18}$$

Referring to Figure 21, given a divergence angle of a beam θ_D, the beam size will change with distance l following:

$$D_{\text{out}} = D_{\text{in}} + l \tan(2 \times \theta_D) \tag{3. 19}$$

For the visible range the fiber collimator F220APC-633 is used. The lens in the fiber collimator is approximately 8.1 mm away from the entrance slit of the fiber and of diameter 7.2 mm. The beam entering should be smaller than the diameter of the fiber collimator lens and using equation (3. 19),

$$\begin{aligned} D_{\text{out}} = D_{\text{in}} + l \tan(2 \times \theta_D) &= 0.0038 \text{ mm} + (8.1 \text{ mm} \times \tan(2 \times 4.753)) \\ &= 1.3601 \text{ mm} \end{aligned} \tag{3. 20}$$

This complies with the requirement of the beam size being smaller than that of the entrance aperture of the fiber collimator lens.

Similar to finding a fiber collimator for the visible range the calculations are repeated for the NIR fiber. The fiber collimator F220APC-850, the lens is approximately 8.55 mm away from the entrance slit of the fiber and of diameter 7.2mm. Thus, the beam entering should be smaller than the diameter of the lens and using equation (3. 19) we find:

$$\begin{aligned} D_{\text{out}} = D_{\text{in}} + l \tan(2 \times \theta_D) & \\ = 0.0053 \text{ mm} + (8.55 \text{ mm} \times \tan(2 \times 4.753)) & \\ = 1.4286 \text{ mm} & \end{aligned} \tag{3. 21}$$

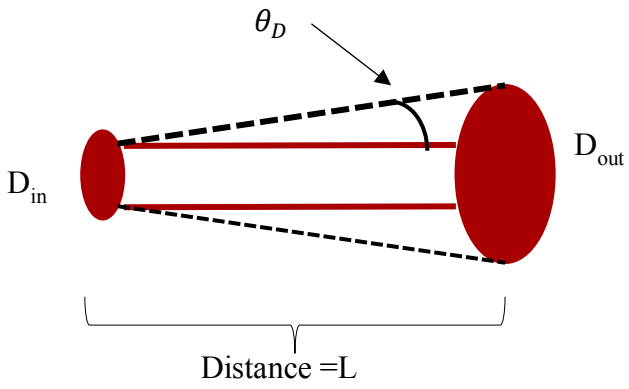

Figure 21 - Beam Diameter over a certain distance

The fiber collimator F220APC-633 has an output diameter of $D_{in} = 2.41$ mm. Thus, as previously seen in Section 3.1.5, to cover 80% of the objective lens surface the required beam magnification according to equation (3. 6) is:

$$m = \frac{80\% \times 1 \text{ cm}}{2.41 \text{ mm}} = 0.33195 \tag{3. 22}$$

$$m = \frac{f_2}{f_1} = \frac{100}{30} = 0.333 \tag{3. 23}$$

where f_1 and f_2 are the focal lengths of the bi-convex (ThorlabsLB1757-B) and plano-convex (Edmund Optics 67-750) lenses, respectively. The new magnification ratio will change the output diameter to be approximately 7.95 mm. Similarly, the fiber collimator F220APC-850 has an output diameter of $D_{\text{in}} = 2.06$ mm. Using the same lenses, the output diameter when the second fiber collimator is used is approximately 6.79 mm. The most suitable anti-reflection coating spectral range for the supercontinuum arm is 650 to 1050 nm since it's the targeted range for this arm.

3.1.11 Spectroscopy Arm

The Raman signal reflected back from the microscope is directed to a third arm in the system dedicated for spectroscopy. To analyze the spectrum of the Raman signal, a monochromator or a spectrometer is used. A spectrometer has an entrance slit and an exit slit and is composed

of a diffraction gratings and a motorized rotating stage. The grating diffracts light of different wavelengths into different directions. As the grating is rotated by the motorized stage in front of the input slit, different wavelengths will be directed towards the output slit. A photodetector can register the output power as a function of time. According to the rotation speed, delay, and the grating, different time slots can be mapped to the corresponding wavelength which was then directed to the output slit and onto a form of detector, such as photodiode or CCD camera.

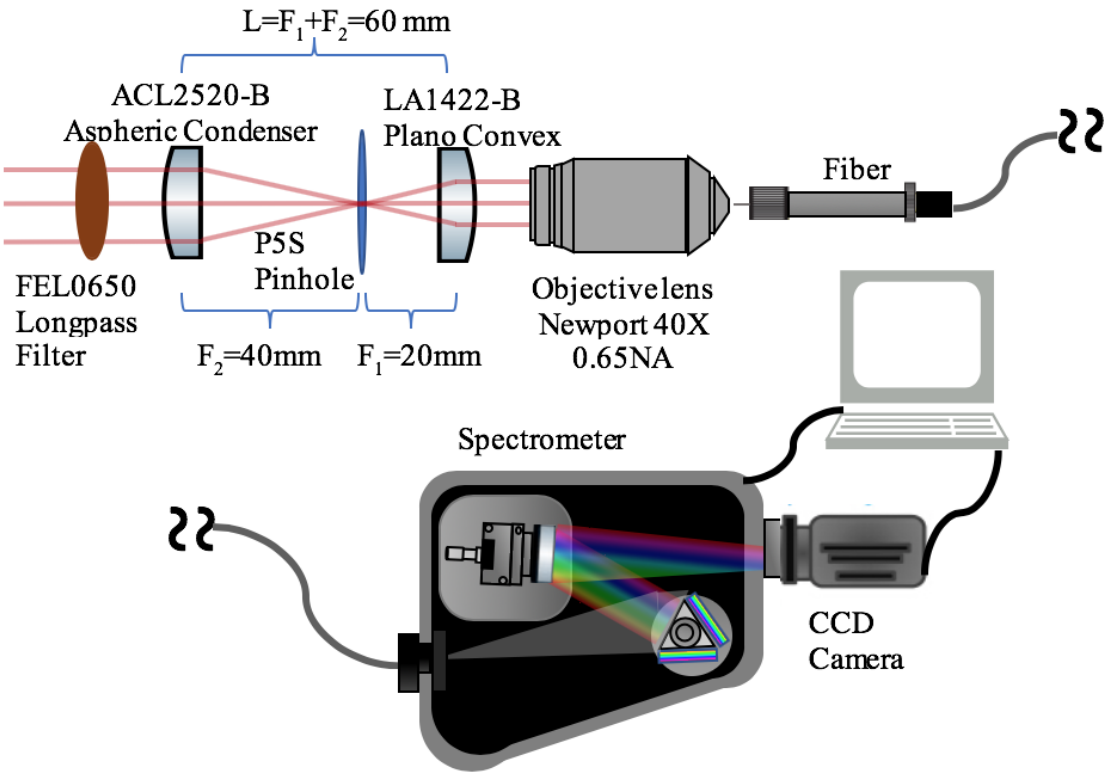

Figure 22 - Spectrometry Arm

3.1.11.1 Laser Rejection Filter

The (elastic) Rayleigh scattering from illumination by the He-Ne laser or supercontinuum source is many orders of magnitudes brighter than the Raman peaks. Consequently, a filter is used to eliminate as much of this spectral content as possible from the Raman signal. The beam is first passed through a long pass filter in order to reject any other wavelengths but the

Raman bands which are redshifted with respect to the pump laser. The filter used is the FEL0650 and it cuts off at 650 nm.

To further clean the signal from unwanted beams, such as ghost beams and stray light, and provide a higher spatial resolution, a confocal scheme may be employed. To do so the Raman beam is focused and passed through a small, *e.g.* 5 μm diameter, pinhole as a spatial filter. Note that only the beams originated at the laser spot on the sample surface will be focused to the pinhole. Thus, the spatial resolution will be primarily determined by the diffraction-limited spot size produced by the objective lens. The reflection of the laser spot itself is already blocked by the longpass filter. Similar to covering the objective lens with an entrance pupil, in order to avoid clamping the beam and causing diffraction, the pinhole has to be slightly under-filled, for example by covering approximately 4 μm in diameter.

To reduce spherical aberration when focusing the beam onto the 5 μm pinhole, an aspheric condenser lens (Thorlabs ACL2520-B) is used as opposed to a bi-convex lens. A wavelength of 700 nm corresponds to the strongest Raman peak of graphene if excited by a He-Ne at 632.8 nm [6]. Thus, assuming a wavelength of 762 nm for the beam and a 4 μm spot size the numerical aperture is:

$$d_{\text{spot}} = \frac{1.22\lambda}{NA} \quad \xrightarrow{\text{yields}} \quad NA = \frac{1.22 \times 762\ \text{nm}}{4\ \mu\text{m}} = 0.23241 \tag{3. 24}$$

$$NA = \frac{D_{\text{in}}}{2f} \quad \xrightarrow{\text{yields}} \quad f = \frac{8.67\ \text{mm}}{2 \times 0.23241} \cong 18.65\ \text{mm} \tag{3. 25}$$

Clearly, a larger focal length will increase the spot size.

3.1.11.2 Beam Contraction and Fiber Coupling

As can be seen in Figure 22, after the beam passes through a filter and an aspheric condenser the beam is focused through a pinhole. The beam is then collimated using a plano-convex lens. The collimated beam is followed by an objective lens (Newport 40X 0.65NA) with an aperture diameter of 5 mm. The input beam is the same collimated beam focused on the first objective lens with $D_{\text{in}} = 7$ mm, as in Section 3.1.5. Hence, to cover 80% of the objective lens surface the beam magnification according to equation (3. 6) is:

$$m = \frac{80\% \times 5 \text{ mm}}{7 \text{ mm}} = 0.5714 \tag{3. 26}$$

$$m = \frac{f_2}{f_1} = \frac{20}{40} = 0.5 \tag{3. 27}$$

where f_1 and f_2 are the focal lengths of the aspheric condenser and plano-convex lenses (Thorlabs LA1422-B), respectively. The new magnification ratio will change the output diameter to approximately 3.5 mm. Similarly to the other arms it is useful to use anti-reflection coatings (ARCs) on the elements to maximize the efficiency of light transmittance and prevent the generation of unwanted ghost beams. The most suitable ARC spectral range for this arm of the microscope is 650 to 1050 nm since the Raman signal is in that range.

Finally, the Raman signal entering the objective lens needs to be focused into a multimode fiber having a 62.5 μm core diameter. Thus, for an objective lens with numerical aperture of 0.65 the spot size at the focal distance of 4.5 mm according to equation (3. 2) is:

$$d_{\text{spot}} = \frac{1.22\lambda}{NA} = 1.31 \text{ μm} \tag{3. 28}$$

The fiber is mounted on a fiber chuck on a stage and is moved until the optimal coupling position is found using a spectrometer or power meter on the other end. The fiber is then coupled into the spectrometer which uses a CCD camera as a detector and is controlled using a computer. The fiber is placed on a stage to allow fine tuning of the coupling. Note that a large core fiber results in easier coupling but also allows more stray light to enter the system.

3.1.11.3 Spectrometer

For a spectrometer to measure Raman signals efficiently it should operate in "single-photon" mode. This means that photons incident on the detector are converted to electrons that are counted by different methods. The main purpose of a spectrometer is to study electromagnetic spectra, or the wavelength composition of light, which it does by the aid of diffraction grating and a detector at the other end. The detector of choice for Raman spectroscopy is some form of CCD camera. The spectrometer used here is the Princeton Instruments IsoPlane SCT320 spectrometer with a CCD resolution of 0.08 nm.

The beam enters the spectrometer through a slit, this slit determines the resolution of the image. The smaller the slit width the higher the resolution but also the higher the chance of not collecting the incident light. After the beam enters it is reflected using a mirror onto the diffraction grating. Most spectrometers have more than one grating setting with different blaze angle. The higher the blaze angle the smaller the spectral range but the higher the resolution. Light reflected from the diffraction grating splits into multiple beams along different directions based on wavelength. This allows the CCD camera to collect the different beams into a spectrum. The CCD used is also from Princeton instruments and is the PI-MAX4: 1024×256. The wavelength range of the CCD is from 200 nm to 900 nm and has a 26×26 μm pixel size.

3.1.11.4 CCD Camera

CCD cameras are a popular choice for Raman spectroscopy. The use of cooling increases the sensitivity [78]. The cooler the system the more sensitive it becomes. The Princeton PI-Max4 CCD camera used in our set-up allows the camera to be cooled up to -20 ℃ electronically.

A CCD is an array of metal-insulator-semiconductor (MIS) or metal-oxide-semiconductor (MOS) pads held at a positive potential that have the ability to detect, store and transfer charge [65], [78]. Each pad creates a well that attracts photoelectrons and holds them in the region of positive potential. The basic idea of photodetection here is detecting a photon in silicon by generating an electron-hole pair. When a photon hits a silicon one of three

things can happen, the photon passes through the silicon, the photon reflects back or the photon is absorbed in the silicon if the energy is higher than the silicon band gap. The incident photon should provide enough energy to exceed the band gap of silicon at 1100 nm. Longer wavelength photons pass through the silicon without detection, however for Raman measurements of graphene the range is between 200 to 1100 nm which is the detection range of the CCD.

The most common structure of CCDs is a MOS capacitor formed by a metal or a polysilicon gate above the dielectric and a semiconductor below [78]. The MOS capacitor is charged by the photogenerated carriers. The gate is also biased to place the semiconductor into inversion. In equilibrium the electrons, minority carriers, would invert the silicon under the gate, however for CCD this never occurs because instead it transfers the accumulated carrier from the well before the well fills up. The potential well are detectors that collect and hold the photoelectrons produced by incoming photons. Each well forms an array and each column of well corresponds to a different wavelength. When a photon is absorbed an electron-hole pair is created and it is stored in the gate until a charge is transferred. To transfer change the MOS structure is positioned next to other MOS structures[65], [78]. Charge is then transferred by either using three sets of clocked gates or an asymmetric well structure.

The biggest noise source in CCDs is the thermal generation of minority carriers [78], however other sources of noise include cosmic rays, transfer inefficiency and fluctuation in the generation of carriers. Another source of noise is stray light from other regions of the lab entering either the fiber or the entrance slit. More advanced spectrometer systems have different functions that can reduce the background noise, apply flatfield subtraction and remove cosmic rays, this will be further discussed in Section 3.2.3.

3.2 Software

To increase the efficiency of the microscope during data collection multiple LabVIEW codes were created and utilized. The piezo controller, lock-in amplifier and supercontinuum laser were all be controlled using LabVIEW, while the spectrometer is controlled using LightField. The Piezo controller controls the movement of the stage and the lock-in amplifier utilizes a DAQ card that acquires the information and sends it to the user. This section will discuss and outlines the basic concepts of these codes and how they operate.

3.2.1 Piezo Controller and Lock-in Amplifier

To collect and send data to the optical setup, LabVIEW is utilized. The LabVIEW code receives and sends data to the Piezo controlled stage (Thorlabs MDT630B) and it collects data from the lock-in amplifier using a DAQ card (model CB-37f-HVD). The piezo controller (Thorlabs BPC303) is a 3-channel controller, however the third channel being the z axis is fixed with the objective lens at the focal point, thus only 2-channels (X and Y) are controlled. The code consists of multiple nested loops where it scans $30\ \mu m$ in one direction and then moves one step (assigned by the user) in the next, consequently a $30 \times 30\ \mu m$ scan is completed in a raster scanning manner. Every time the stage moves one step, it collects data from the DAQ card which reads its measurements from the lock-in amplifier readings that are obtained through the photodetector. The code specifications are further discussed in Appendix G.

3.2.2 Supercontinuum control

Another code was constructed to control the SuperK laser while also obtaining areal scans of the desired area. The SuperK Extreme laser has an external RF driver and two different filter boxes. The filter boxes have three fiber delivery system that deliver the signal either through free space, but with a large divergence angle or through a fiber. The desired laser wavelength 400-1100 nm is split over two different filter boxes. The first from 400-700 nm and the second

from 640-1100 nm. The laser and RF filter need to be turned on physically using a switch and a key. Following that the laser can be fully controlled using the NKT photonics software or LabVIEW including turning on the emission and the RF power. The code moved the stage in one step size and then scanned the full desired wavelength range of the desired filter box. The movement of the stage is similar of that of Section 3.2.1. The code specifications are further discussed in Appendix H.

3.2.3 Spectrometer control

For the spectrometer arm the software Lightfield was provided by Princeton instruments. There are a few features in the software that have proven to be useful in the data collection process. The exposure time, the time between the start of the acquisition and end of the acquisition, allows for a more sensitive and more accurate measurements. Initially one starts with a higher exposure time until the signal is optimized to be high enough for exposure, 20 seconds was needed for this study. Furthermore, the intensifier gain can be used to intensify the signal if it's too weak. The number of exposure and the exposures per frames can also be used to obtain a more accurate response that can later be averaged out.

One of the most useful features that are applied before acquisitions are the background subtraction and the flatfield correction. The background correction is used when the light source is turned off to obtain the average background noise and remove it from the response signal. An ideal sensor would be uniformly illuminated and have all pixels producing identical signals in a flat uniform manner. However, real sensors don't behave that way due to variations of random noise, dark current and gain. Thus, flatfield correction normalizes and adjusts the image so the variations in the pixels is accounted for. The relation between flatfield and background correction is $(\text{raw} - \text{background})/\text{flatfield}$. Finally, another function is the cosmic ray removal which removes high localized spikes after the data is collected and before its stored.

3.3 Image of Optical setup

In Figure 23 One can see the optical setup as a whole in the lab. This setup is collated to the sketch seen in Figure 12 and explained throughout chapter 3. Notice how a cage system was used to ease the alignment of lenses to each other, to the lasers and other components in the setup.

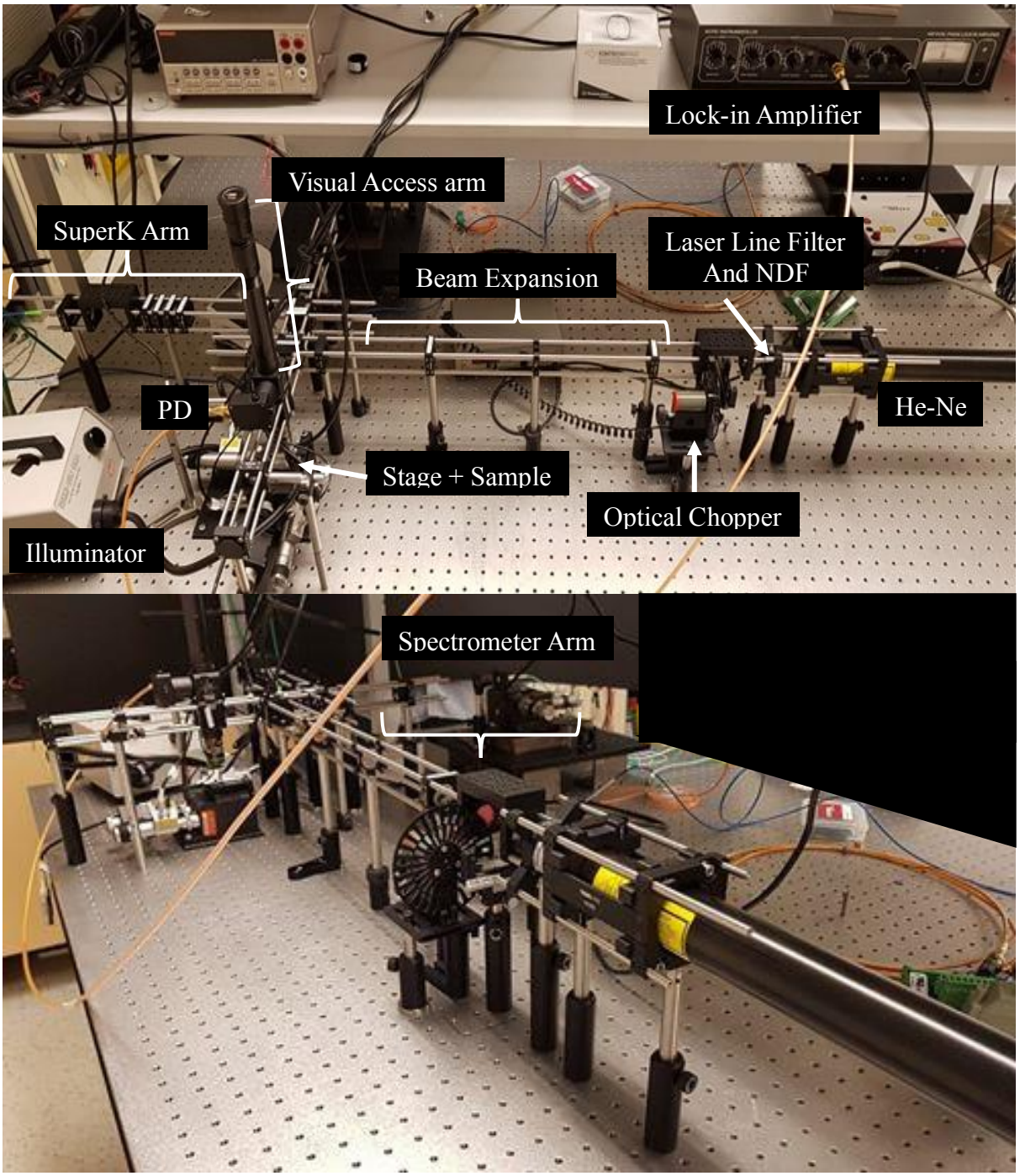

Figure 23 – Image of optical setup in the lab. The system continues to another room where the spectrometer is located.

Chapter 4 – Results and Measurements

4.1 Device Structures

In this study arrays of gold monopole nanoantennas of different resonant frequencies are fabricated on graphene to explore Raman enhancement of graphene. CVD grown graphene is a single layer of graphite with a 2-D honeycomb lattice structure (as described in Chapter 2). The devices, purchased from Graphene Supermarket, consist of single layer CVD hexagonal Boron Nitride film covering a 285 nm-thick thermally-grown silicon-dioxide layer on a 500 nm thick single crystal silicon substrate (p-doped) as sketched in Figure 24. The silicon was grown on an R-plane 500-nm-thick sapphire substrate. Fabrication of the nanoantenna structures is achieved via electron-beam (e-beam) lithography, evaporation and lift-off on CVD grown graphene. The structures consist of multiple arrays of 22 nm thick rectangular gold nanorods of different lengths l, and widths w. The nanoantennas are arranged over the surface following pitch p and q. The nanoantennas were fabricated by Anthony Olivieri.

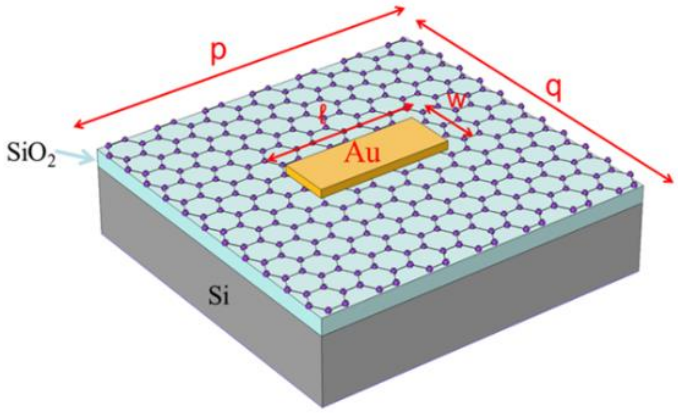

Figure 24 - Nanoantenna structures of length l, width w, thickness t and pitch p and q [52].
DOI:https://doi.org/10.1103/PhysRevB.91.201408

The graphene SiO_2/Si wafers are first annealed at a temperature of 200 ℃ in ambient conditions for two hours. The first step in fabricating the structures is to use a generic mask for nanoantennas to create alignment marks. To create the alignment marks a photosensitive bi-layer composed of LOR1A and of S1805 is spin-coated on to the sample and used as a positive resist. After the bi-layer resist is spun into the wafer and the mask is applied by inserting the wafer into a mask aligner. This is followed by exposing the wafer to UV light for 4.5 seconds while in the mask is placed on top of the wafer (the S1805 layer is sensitive to

UV light). This is followed by developing the wafer using Microposit MF-321 Developer for two minutes and 50 seconds.

The developing process will create a pattern engraved into the two resist layers. A layer of 22 nm gold is then deposited on the patterned wafer and developed bi-layer resist, then removed using a lift-off process by dipping the wafer in PG remover for 20 min. It is then cleaned using acetone and IPA, and is ready for e-beam lithograph. E-beam lithography is the process of writing patterns into thin films of electron sensitive material by using a finely focused electron beam [83]. The combination of electrical scanning and interferometrically-monitored mechanical motion of the substrate allow for very complicated patterns to be generated with great precision.

To prepare the wafer for the e-beam lithography a bi-layer of ploy(methyl methacrylate) PMMA is spun into the wafer (PMMA is an e-beam sensitive polymer). The first layer is of lower density PMMA of 495k molecular weight (MW) covered by higher density layer of 950k MW PMMA, with the lower layer having larger thickness. Both layers were baked at 180℃ for one hour and cooled to room temperature before any further handling. The implementation of a bi-layer of high molecular weight (HMW) and low molecular weight (LMW) PMMA is essential because it results in a desirable undercut pattern profile after developing as sketched in Figure 25c and d. This is due to the high MW layer developing less rapidly. An undercut prevents the formation of structure along the resist sidewalls when the metal is deposited as sketched in Figure 25a and b resulting in a thicker metal layer around the edges of the structures.

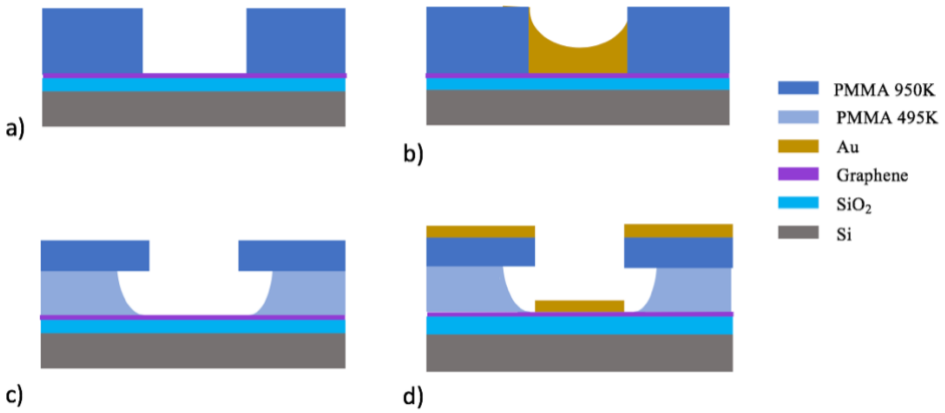

Figure 25 – a) One layer of PMMA on the wafer after e-beam exposure. b) Deposition of gold on one layer of PMMA a wing like structure appears. c)Bi-layer PMMA with a more dense PMMA on top after e-beam exposure. d) Deposition of gold on a bi-layer PMMA, the desired nanoantenna pattern is observed

After cooling, the wafer is loaded into the e-beam lithography system, and the desired pattern designed using Raith e-line layout software is uploaded. The alignment marks are used to align the wafer to the e-beam layout and a 30kV acceleration voltage is applied with an aperture of 10 μm, where higher voltage means higher resolution. The e-beam will thus expose all the areas of the wafer containing nanoantenna structures. The sample is then unloaded and baked for one hour at 95 ℃. It is then developed using a mixture of Methyl isopropyl ketone (MIPK) and Isopropyl alcohol (IPA) at a ratio of 1:3 at 20 ℃. The e-beam breaks the molecular chains in PMMA and the developing process removes everything from the regions where the chains of molecules were broken. This will create a pattern which allows the deposition of gold using evaporation in a 22nm thick layer. Finally, the wafer is placed in an acetone bath at 40℃ which is sonicated at 30 kHz for one minute to remove the excess gold from all the areas of the wafer except for the desired nanoantenna structures.

Each nanoantenna is part of an array covering an area of $20 \times 20\ \mu m^2$, which contains 40×40 nanoantennas uniformly distributed with an average pitch of p = q = 500 nm along both directions. The length of the nanoantennas varies from 50 to 180 nm and their widths from 30 to 45 nm in step sizes of 10 and 5 nm, respectively, following the layout map shown in Figure 26. The layout creates a combination of different nanoantenna sizes that will resonate at different wavelengths. The different resonant wavelengths will ensure that some arrays with overlap spectrally and enhance the graphene Raman signal at the desired wavelength.

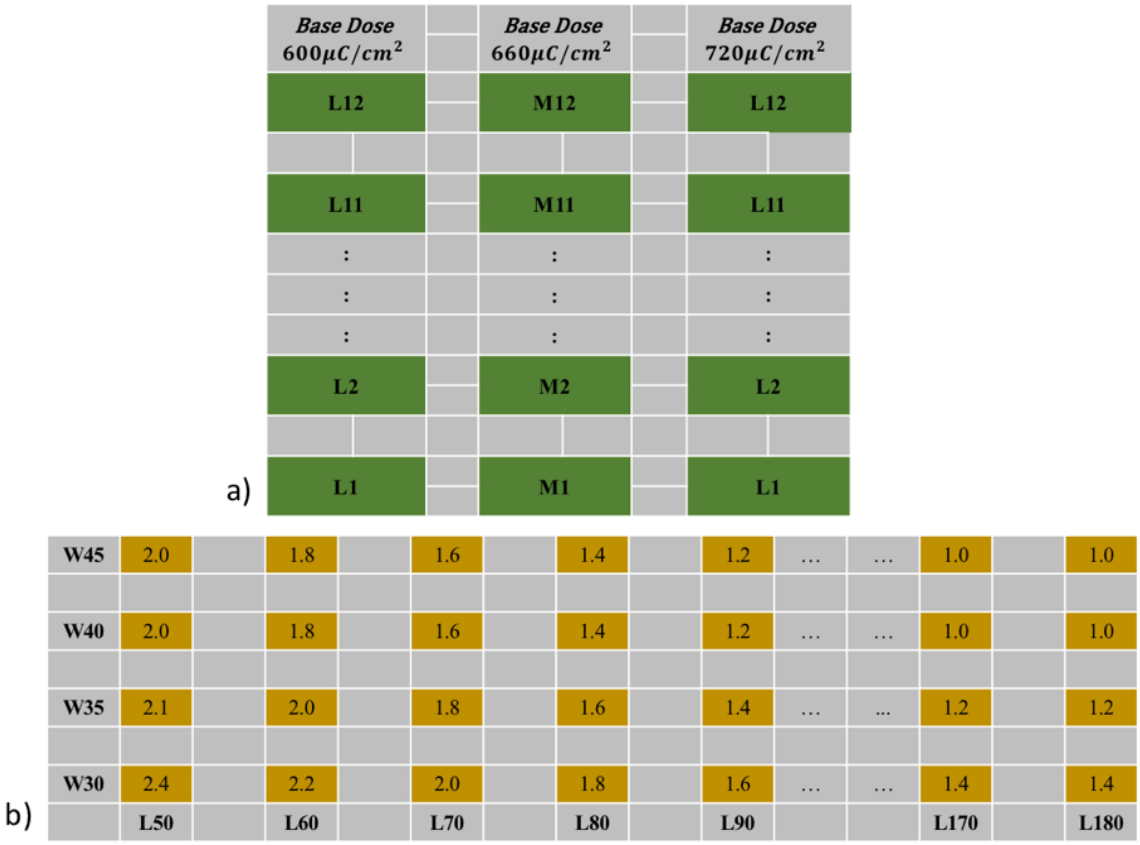

Figure 26 – a) Layout of nanoantenna arrays on the wafer. There are three different sets of arrays with different base dose factor. b) Layout of one nanoantenna array with the base factor coefficient in each array w and l are the desired width and length respectively.

Different dose factors (DFs) were used to carry out the e-beam exposure, also yielding different antenna geometries and sizes. The dose is determined in part by the exposure time and the beam current, and consists of the number of electrons per unit area delivered. If the dose is too high the pattern is severely distorted and if it's too low the pattern is not of high accuracy, the correct dose is found through experimentation. Figure 27 shows a SEM image of a well-formed nanoantenna. Comparing the length and width to the designed ones reveals a 6 to 8 nm increase in these dimensions, which is taken into consideration when designing the layout of the structures.

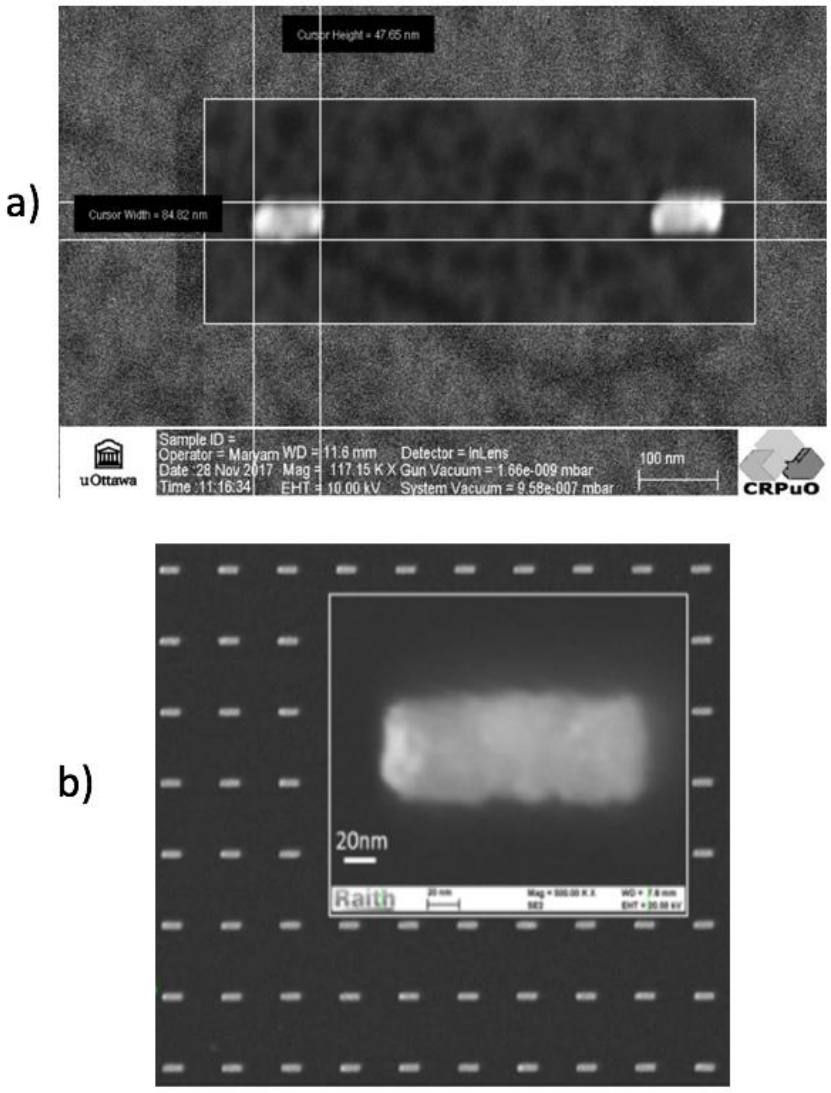

Figure 27 – a) SEM image of fabricated array 5C Layout structure, $w_{designed} = 40\ nm$ *,* $w_{experimental} = 48\ nm$ *and* $l_{designed} = 90\ nm$ *,* $l_{experimental} = 84.82\ nm$*. b) A close up of a single nanoantenna at magnification 500X*

Furthermore to evaluate the quality of the fabricated devices an atomic force microscope (AFM) was used to measure the roughness of the sample as well as the thickness of the nanoantennas. As can be seen from Figure 28 the surface is roughness (arithmetic average of the absolute value of the surface height deviation measured from the mean plane) for the area off the nanoantenna, labeled in green, is $R_a = 0.896$ nm. Another way is to characterise roughness is to measure R_q which is the root mean square average of the height deviation measured from the mean image plane, in this case on the nanoantenna $R_q = 1.113$ nm. Similarly, the roughness on the nanoantenna, labeled in red, $R_a = 2.202$ nm and

$R_q = 3.011$ nm. One can also note that the thickness of the nanoantennas from Figure 29 is approximately $t_{experimental} = 23.185$ nm with the surface roughness taken into account which compares reasonably well with the designed value $t_{designed} = 22$ nm.

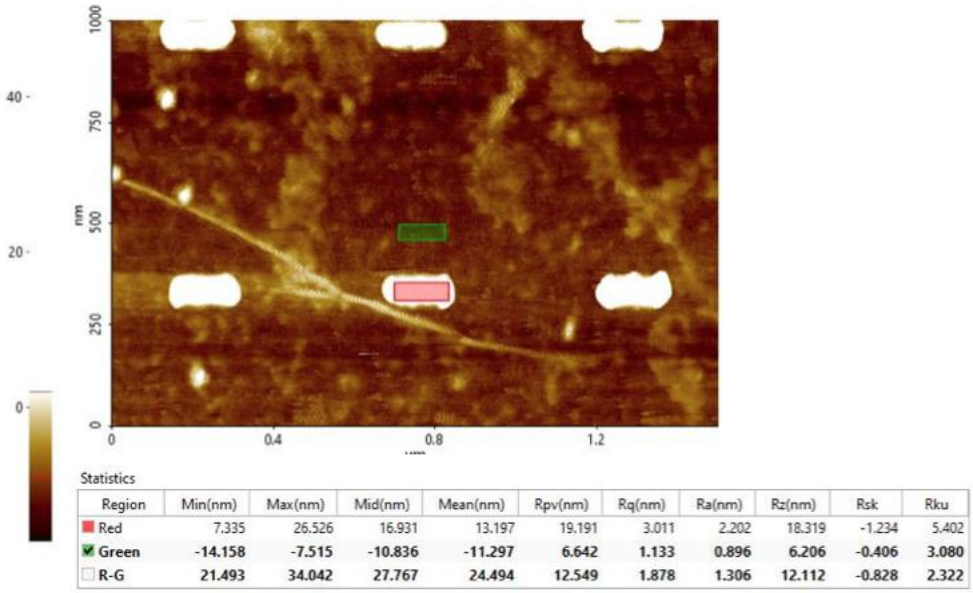

Figure 28 -AFM line cut and surface roughness

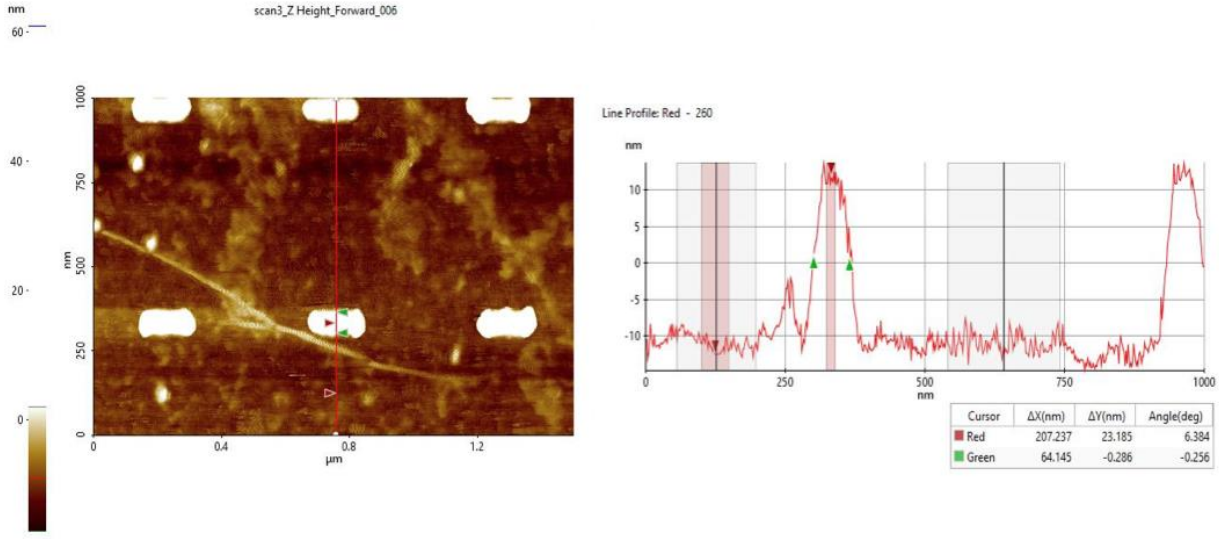

Figure 29 -AFM Surface thickness

4.2 Experimental Procedure

The optical setup described in Chapter 3, was used to obtain various measurements. It is designed with the intent to conduct three different measurements with slight or no alterations required. Currently all arms of the optical setup are functioning efficiently and effectively separately and have not be tested as a whole system. One can obtain normalized reflectance graphs, spontaneous and stimulated Raman spectra. Here we describe the methods and the results obtained for the reflectance responses and the spontaneous Raman scattering – the stimulated Raman experiments are relegated to future work.

4.2.1 Normalized Reflectance Response Experimental Procedure

Similar to classical antennas, the spectral resonance of an optical antenna depends on the geometry of the structure. Antenna length, width and thickness are all known crucial parameters in nanomonopoles, nanodipoles, and nanobowties [34]. The optical system used to obtain normalized reflectance responses is shown in Figure 30.

The source used to measure the reflectance responses is the super continuum source. The super continuum source is tuned to the desired wavelength or wavelength range using the LabVIEW code discussed in Section 4.2.2. Using the tunable filter, three different wavelengths are used to couple into the fiber and align the beam in the optical system. A few wavelengths are used to optimise the coupling efficiency since the beam divergence and behaviour changes as the wavelength changes. This is due to the optical fiber and components in the setup exhibiting wavelength dependence. Thus, multiple wavelengths result in the best beam profile and focus possible over the entire wavelength spectrum used.

The half wave-plate and the polarizers are used to ensure that the laser beam is polarized in the same direction as the nanoantenna in the arrays placed on the stage since they are polarization sensitive. After the beam is expanded, collimated and focused it is incident onto the sample. The reflected signal is then collected by the photodetector and sent to the computer through the lock-in amplifier. The measurements can be completed by scanning

over a $30 \times 30\ \mu m^2$ area including the substrate and finding the ratio of the reflectance form the nanoantennas to that from the substrate, which takes around 30 hours, with minimal to no system variations over the time period, depending on the time delay in data acquisition. Alternatively an average of five or more points on the nanoantenna array and off the nanoantenna array can be used to find the ratio between the two reflectance's which can take 20 minutes or less.

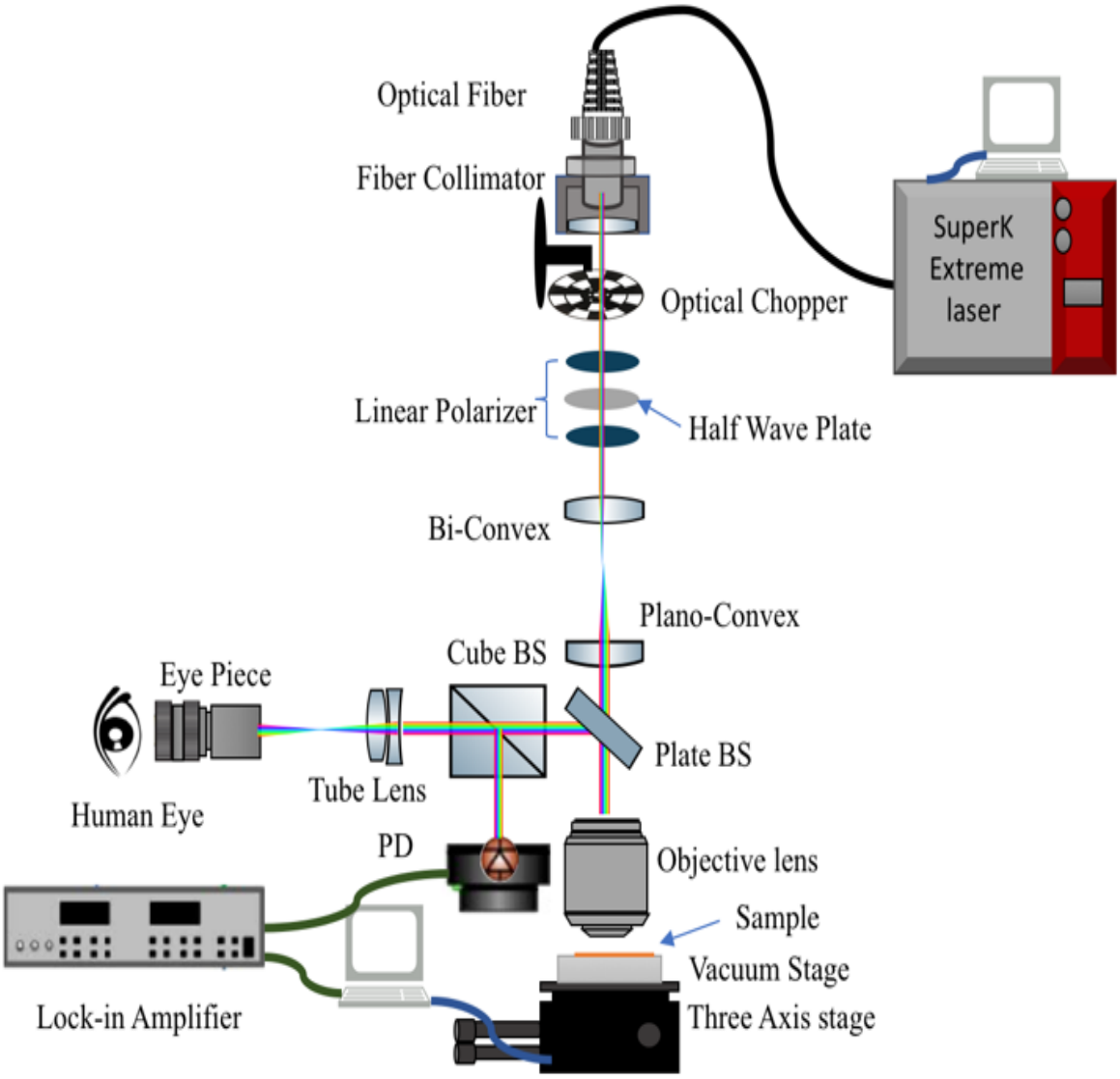

Figure 30 – Normalized Reflectance Optical setup

4.2.2 Spontaneous Raman Experimental Procedure

This part of the setup works like a classical spontaneous Raman spectroscopy system by using the pump He-Ne laser only (the Stokes laser arm is unused). The He-Ne laser polarization is first aligned to that of the nanoantennas. The beam from the laser is guided through the optics to the objective lens and consequently onto the sample. The spontaneously emitted Raman signal passes through the spectrometer arm and eventually into the spectrometer and camera for detection and analysis. The dichroic mirror and longpass filter are used to block the He-Ne beam from entering the spectrometer and saturating it; however, they can be removed to align the optics in the spectrometer arm and ensure that the beam couples into the fiber. Once a Raman signal is detected, the coupling to the fiber can be re-optimised (the Raman wavelength is sufficiently different from the He-Ne laser wavelength to causing a slight shift in the light path and focal points).

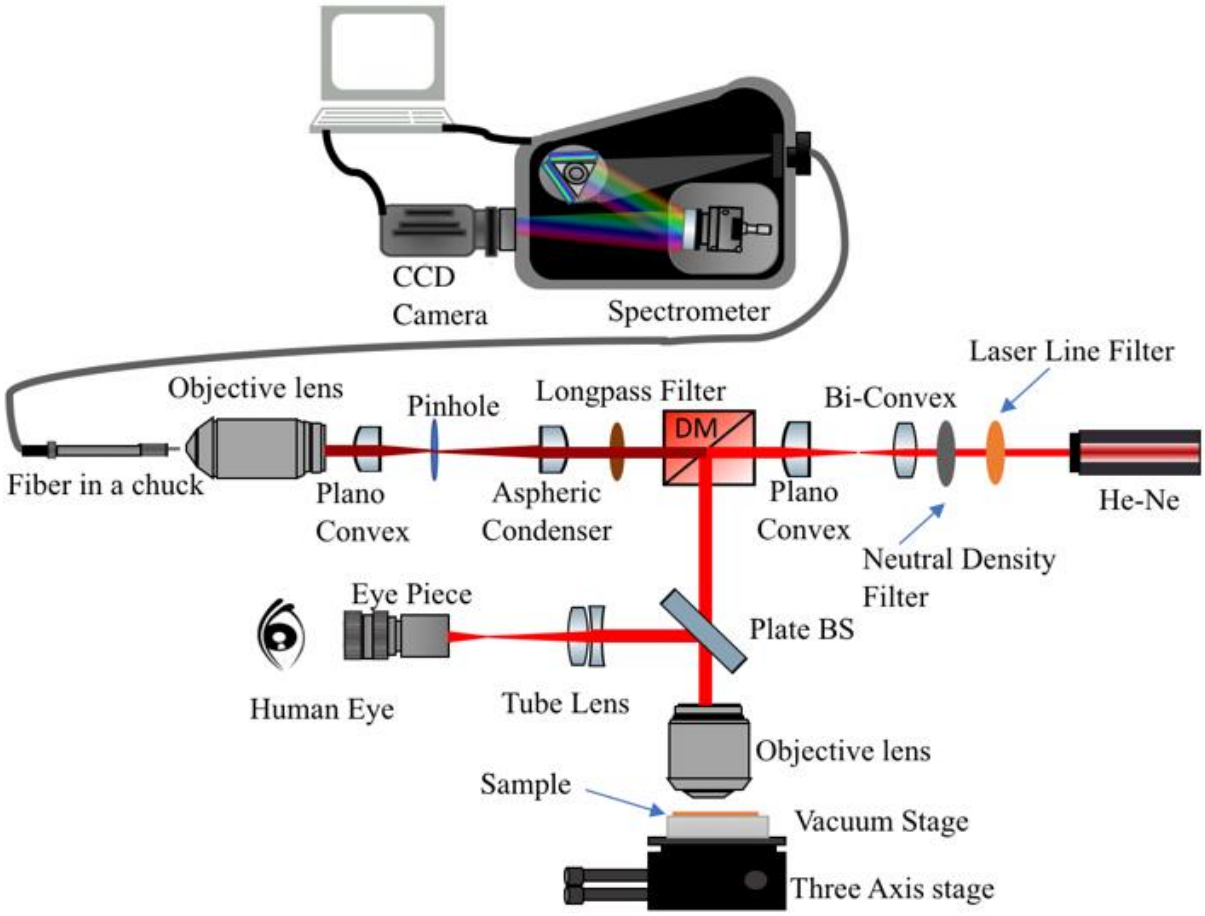

Figure 31 - Spontaneous Raman optical setup. BS: beam splitter, DM: Dichroic Mirror

4.2.3 Stimulated Raman Experimental Procedure

The final objective of the optical setup is to produce stimulated Raman scattering (SRS). SRS enhances the scattered signal because its scattered light is a few magnitudes higher than that of spontaneous Raman scattering. The process uses two light sources, a pump at a constant frequency ω_p and a Stokes at scanned frequency ω_s combined to amplify the Stokes Raman signal when incident on the sample. The He-Ne light is used as the pump source and the tunable super continuum source as the Stokes source. The experimental procedure of the stimulated Raman setup uses all aspects of the setup, as seen in Figure 12 in Section 3.1, with the exception of the photodetector since the spectrometer is the detection tool needed for the Raman signal.

4.3 Normalized Reflectance Responses

4.3.1 Introduction and Initial Quality Measurements

Nanometallic structures are essential to the conversion of light to SPPs localized to ultra-small volumes. Such structures can provide highly enhanced fields, strong confinement and high surface sensitivity, so they are of interest in many applications, including plasmon-enhanced nonlinear optics [3], [6], [52], [84]. The nanoantenna geometrical length (l) and width (w) are varied, while keeping the thickness $t = 22$ nm fixed as well as the vertical and horizontal distance (p, q) between the nanoantennas in a 2-D array to change the spectral position of the resonance. Before acquiring the normalized reflectance response it is essential to quantify the quality of the beam and of the reflectance obtained.

Figure 32 shows an area scan of a $l \times w = 15 \times 15$ μm^2 square gold patch 100 nm in thickness fabricated by e-beam lithography, metal evaporation and lift-off on a Si wafer fabricated by a PhD candidate Maude Amyot-Bourgeois. The scatter image (a) is the result of obtaining data from the photodetector and moving the stage over an area of 30×30 μm^2 containing the square. Furthermore the two bottom images (b and c) show the line-cuts along the horizontal and vertical axes. As further analysis, the reflectance ratio obtained experimentally can be compared with the theoretical results, as discussed further below.

From Figure 32b one can approximate the $1/e^2$ Gaussian beam diameter by finding the derivative of the line cut [85]. This derivative is Gaussian fitted and can be seen in Figure 33 for the right and left sides of the knife edge. From these plots one can deduce the $1/e^2$ beam diameter by finding the maximum of the Gaussian fit and dividing it by e^2. Using both edges results in a beam diameter of approximately:

$$6.825\ \mu\text{m} - 5.369\ \mu\text{m} = 1.456\ \mu\text{m} \text{ and } 20.44\ \mu\text{m} - 18.56\ \mu\text{m} = 1.88\ \mu\text{m} \quad (4.1)$$

By observing Figure 32 it is evident that the beam diameter or the spot size appears to be different in the x and y directions. This is due to the energy diffracted into the shadow

region when incident rays are parallel to the surface of an edge, vertex or corner [86]. Thus, the knife edge technique is polarization sensitive and thus one cannot deduce the beam diameter in both directions by examining a singular polarization. Balanis [86] discussed that the normalized amplitude pattern produced by an incident hard polarization (parallel to the edge) is almost isotropic (radiating in all directions), which in turn blurs the image. In this case, the beam is horizontally polarized, meaning that a circular beam may appear elliptical in a line scan along the y-direction as a result of diffraction from the edges. A theoretical and experimental comparison of the reflectance from the gold structure is calculated below.

1) Reflectance – Theoretical

The experimental reflectance measurements of a thick gold film (100 nm) on silicon are compared to theory using the computed reflections from the air-Au and air-Si systems. The complex refractive index for gold is $n_{Au} = 0.18377 - j3.41313$ [87] and the complex refractive index of silicon is $n_{si} = 3.882 - j0.019$ [88] at the wavelength of 632.8 nm. Using the Fresnel reflection equation, the reflection coefficient in air from these systems are:

$$r_{Au} = \frac{n_{Au} - n_{air}}{n_{Au} + n_{air}} = \frac{0.18377 - j3.41313 - 1}{0.18377 - j3.41313 + 1} = 0.818590 - j0.53054 \quad (4.2)$$

$$R_{Au} = |r_{Au}|^2 = 0.9436 \quad (4.3)$$

$$r_{Si} = \frac{n_{Si} - n_{air}}{n_{Si} + n_{air}} = \frac{3.882 - j0.019 - 1}{3.882 - j0.019 + 1} = 0.5903 - j0.00159 \quad (4.4)$$

$$R_{Si} = |r_{Si}|^2 = 0.3485 \quad (4.5)$$

Thus, the ratio of the reflectances is,

$$R_{Theoretical} = \frac{R_{Au}}{R_{Si}} = 2.7076 \quad (4.6)$$

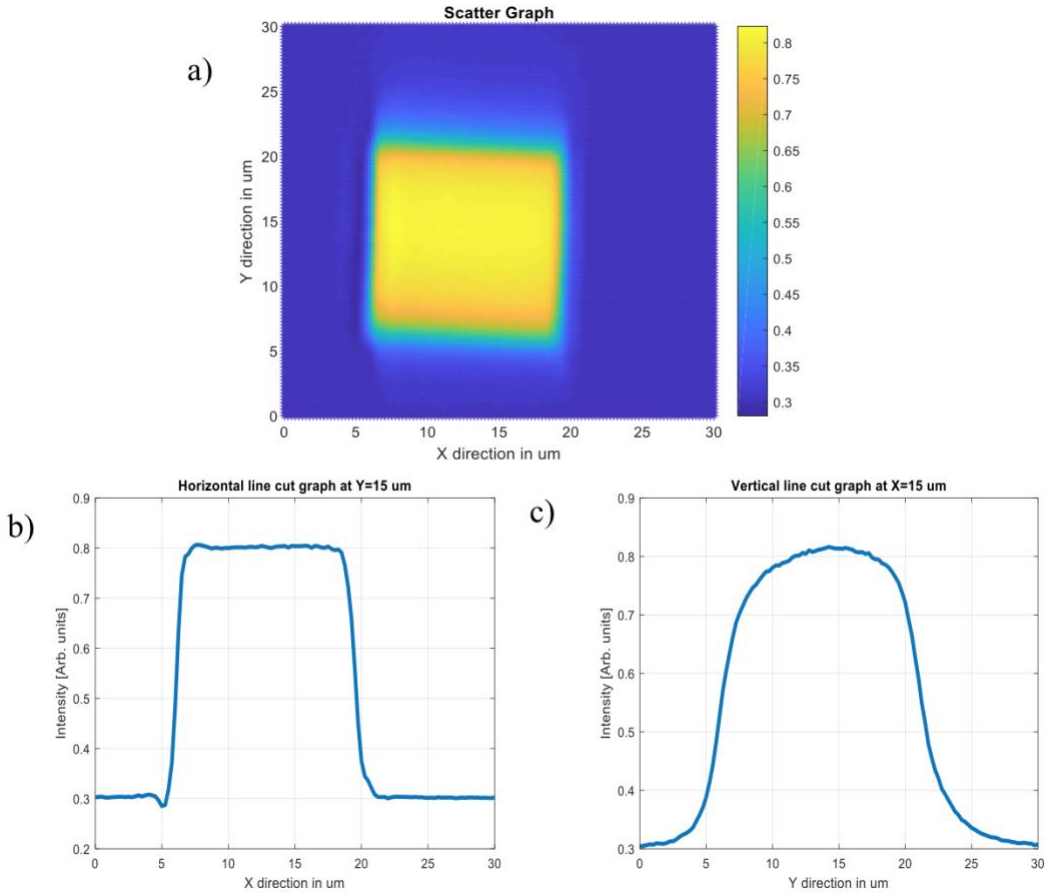

Figure 32 – (a) Area scan of a 15 *μm* × 15 *μm gold square; (b) Horizontal line cut graph at Y =* 15 *μm; (c) Vertical line cut graph at X =* 15 *μm.*

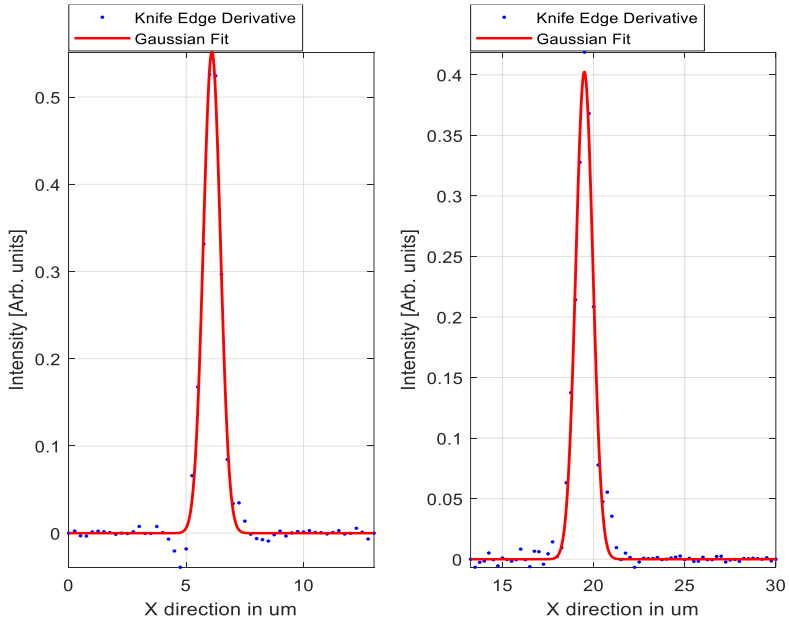

Figure 33 – Derivative of the line-cut (also known as the knife edge) along the x-axis seen in Figure 32

2) Reflectance – Experimental

After completing the setup, an areal scan of a thick gold layer (100 nm) on silicon was measured as seen previously in Figure 32. The higher amplitudes are due to a stronger reflection from the gold film, and the lower ones from silicon. Thus, the reflectance of gold and silicon are approximately

$$R_{Au-Experimental} = \left|r_{Au-Experimental}\right|^2 = \frac{0.797 + 0.7884}{2} = 0.7927 \quad (4.\ 7)$$

$$R_{Si-Experimental} = \left|r_{Si-Experimental}\right|^2 = \frac{0.3181 + 0.3078}{2} = 0.31295 \quad (4.\ 8)$$

Forming the ratio of the reflectance from the Au surface to the Si surface yields:

$$R_{Experimental} = \frac{R_{Au}}{R_{Sub}} = 2.533 \quad (4.\ 9)$$

Comparing the theoretical and experimental ratios, yields the error in our measurements which is:

$$\%\ \text{Error} = \left|\frac{\text{Experimental} - \text{Theoretical}}{\text{Theoretical}}\right| \times 100 = 6.4\% \quad (4.\ 10).$$

In the next section, measurements as the design parameters of the nanoantennas are varied is carried out by varying one design parameter at a time and measuring the response of the antennas. Results are presented for monopole antennas in Sections 4.3.2 and 4.3.3.

4.3.2 Length

The fabricated nanoantenna arrays are very useful to enhance light-graphene interaction. This can be concluded from the strong resonance observed from the reflectance measurements obtained for nanoantennas on graphene, as shown in Figure 34. The normalized measurements shown are reflectance ratios of $R_{\text{antenna}}/R_{\text{substrate}}$. One can deduce that for nanoantennas of fixed width and thickness, the resonance wavelength shifts to longer wavelengths as the length of the nanoantennas increases. The shift is expected by correspondence to classical antennas,

where resonance occurs when the antenna length is roughly half a wavelength. Increasing the length thus increases the wavelength at which the antenna is resonant.

From Figure 34 it is seen that nanoantenna arrays containing antennas longer than 114 nm and a width of 47 nm, have a very small reflectance ratio. Figure 36 shows this more clearly by showing that nanoantennas longer than 114 nm do indeed resonate at 950 nm and somewhere beyond 1050 nm, however, the resonance ratio is low and the signal is noisy. This suggests that Raman scattering will not be enhanced significantly when using such nanoantenna arrays. It is worth noting that as the nanoantennas become longer the distance between them in the horizontal axis also becomes smaller but the distance between them in the vertical axis will stay the same. This means that using the laser in the vertical polarization would change the pitch p and q of the nanoantennas. Thus, even the antennas that follow a square geometry instead of rectangular will have a shift in their resonance when the polarization is changed by $90°$ degrees. The effects of changing the pitch of the nanoantenna on the reflectance is investigated in more detail in [34], where the authors concluded by simluation that changing the pitch and making it smaller would increasing the coupling between adjacent antennas, thus the response. For a square pitch were $p = q$ a red shift would occur.

Theoretical reflectance ratios were computed by Saba Siadat Mousavi (a PhD candidate in our lab) to compare with the measurements of Figure 34. She adopted the same nanoantenna thickness and width, allowing the length to vary, and disposes them onto SiO_2 on Si, neglecting the graphene. The neglect of graphene is due to the lack of computational power to achieve the required model accuracy for the one atom thick graphene layer. One can see from Figure 35 that the theoretical resonance response follows the same trend as the measured experimental response. There is a slight shift in the resonance frequency which can be explained by the neglect of graphene in the model and by possibly different optical parameters for the nanoantennas metal (Au) compared to the bulk values. Furthermore, the fabricated nanoantennas are not perfect, they have slightly rounded the corners as can be seen in Figure 27, and slight variations in length.

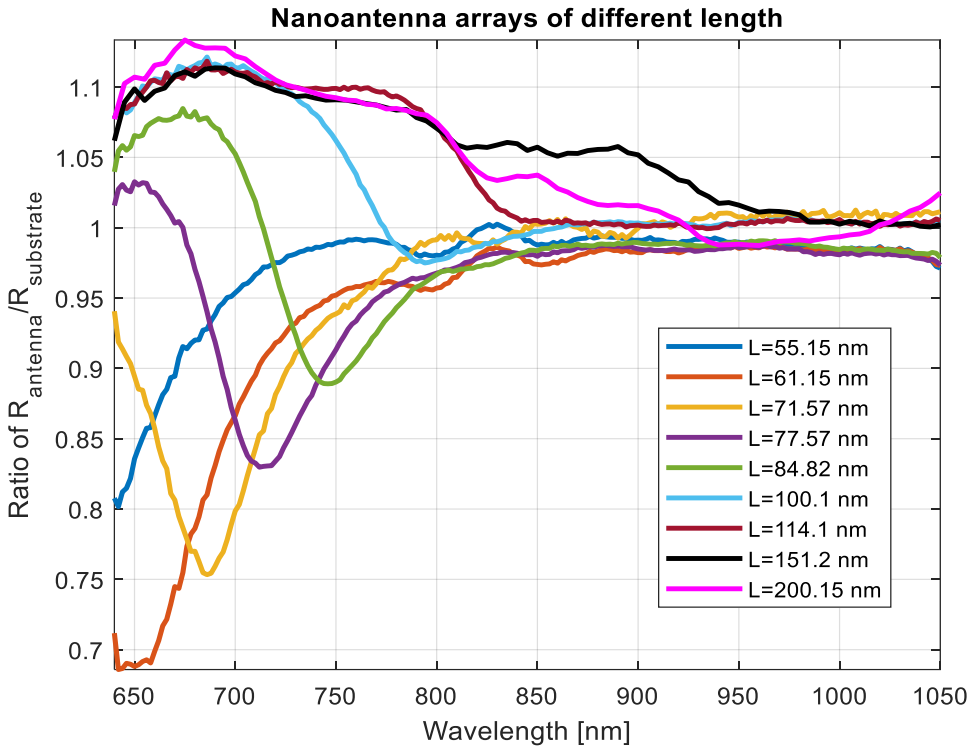

Figure 34 - Normalized reflectance response of arrays of nanoantennas of differing length. The width and thickness of the nanoantenna are w=47.65 nm and t= 22 nm. The Ratio on the y-axis is the $R_{Au}/R_{substrate}$.

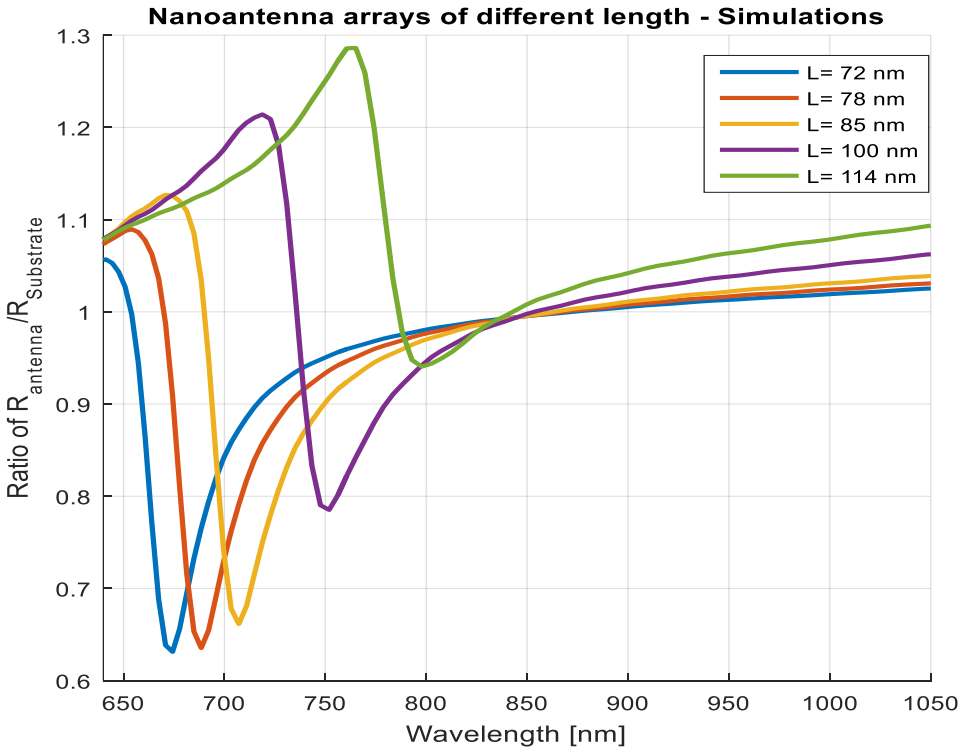

Figure 35 - Theoretical results of change of length and fixed width=47 nm and thickness of t=22 nm obtained using Lumerical by Saba Mousavi

One can briefly described how the simulation process was carried out according to Saba Mousavi using Lumerical. An infinite array is constructed by repeating the array cells along x and y with pitch p and q, respectively in accordance to the actual design discussed in Section 4.1. An x-polarized plane wave with magnitude 1V/m illuminates the array from the top normal to the incidence. The FDTD method is used with $0.5 \times 0.5 \times 0.5\ \text{nm}^3$ mesh in the region around the nanoantennas was used for the simulations. Palik's material data is used [89]. The reflectance plane was located 2.5 µm above the interface. The mesh dimensions revealed a ~2% error, which was considered acceptable considering the structural response of the structure. The transmittance was calculated to be,

$$T(f) = \int_s Re\{P^m(f)\} \cdot ds \,/\, \int_s Re\{P^s(f)\} \cdot ds \tag{4. 11).}$$

Where $P^{m,s}$ is the Poynting vector at the monitor and source location, f is the frequency and S is the surface of the reference plane [34]. Then the reflectance can be calculated from the same equation by changing S to the reflectance plane R.

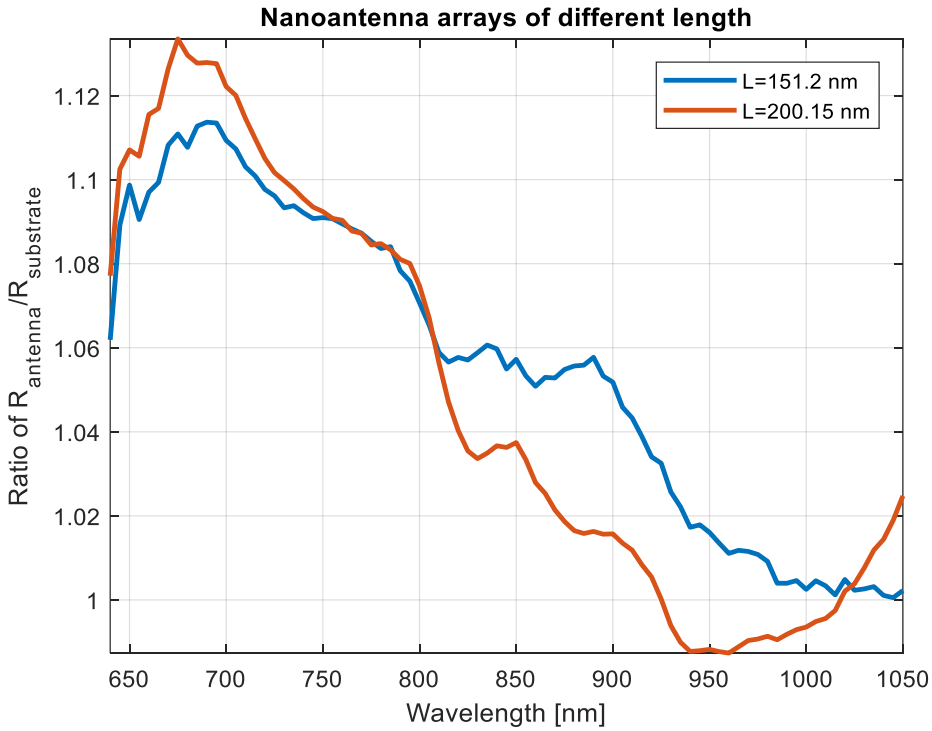

Figure 36 – Two nanoantennas arrays of antennas longer than 114nm. The Ratio on the y-axis is the $R_{Au}/R_{substrate}$.

4.3.3 Width

The width of the nanoantennas is a second design parameter. Considering the systems response to changes in width w, shown in Figure 37, one notes that increasing the latter blue-shifts the reflectance resonances. Furthermore, it is evident that the amount of shift decreases as $\Delta w/w$ decreases. This trend is a result of the n_{eff} decreasing with an increase of width. Thus using the relation $\lambda_{\text{res}} = 2L_{\text{eff}}n_{\text{eff}}$ that was discussed in equation 2.19 previously, this will cause a blue shift in the resonance wavelengths. The same points about pitch discussed in Section 4.3.2 apply here. Additionally, to compare the experimental results to theory, Saba Mousavi produced computations as a function of width in a similar manner as done in Section 4.3.2, as seen in Figure 38. Comparing the theoretical and experimental results, it can be observed that theory and experiment follow the same trends. However, as mentioned earlier, the lack of graphene in the computations, the rounded antenna corners and the slight variation in the width can alter the exact resonance position.

Another important thing to mention is that if the polarization were changed in the other (perpendicular) direction, the nanoantennas would still resonate. However, since the length and width are transposed the nanoantennas would be shorter and wider, resulting in them resonating at a short wavelength (650 nm). This means that all nanoantennas will resonate even in the opposite polarization of the design.

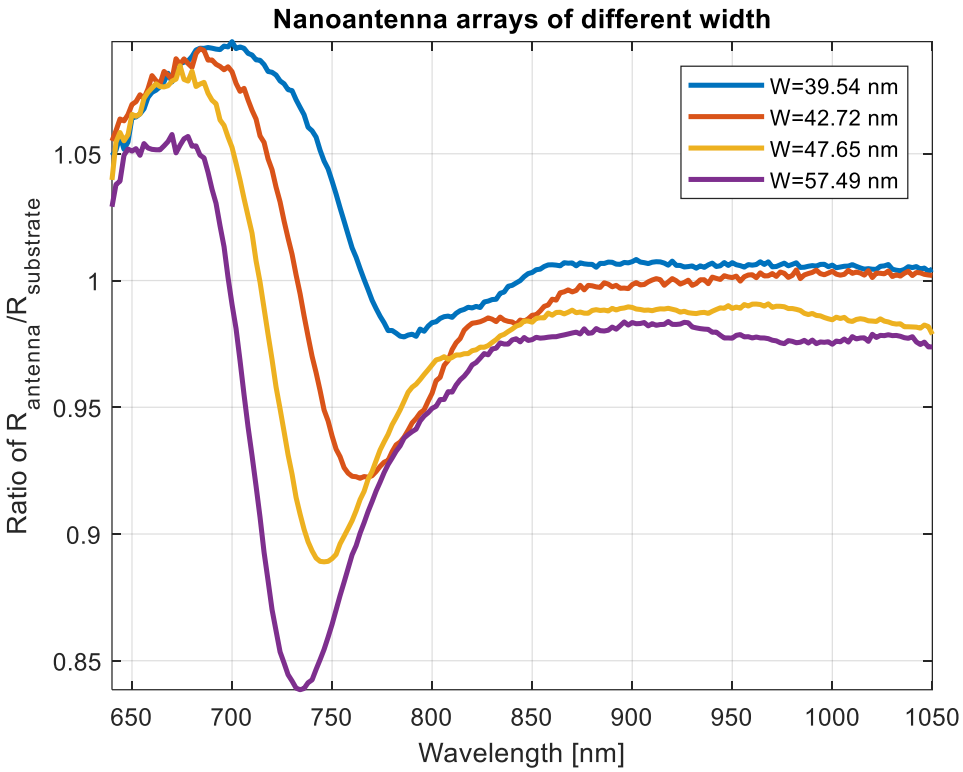

Figure 37 - Normalized reflectance response of arrays of nanoantennas of differing width [3]. The length and thickness of the nanoantenna are l=84.82 nm and t= 22 nm. The Ratio on the y-axis is the $R_{Au}/R_{substrate}$

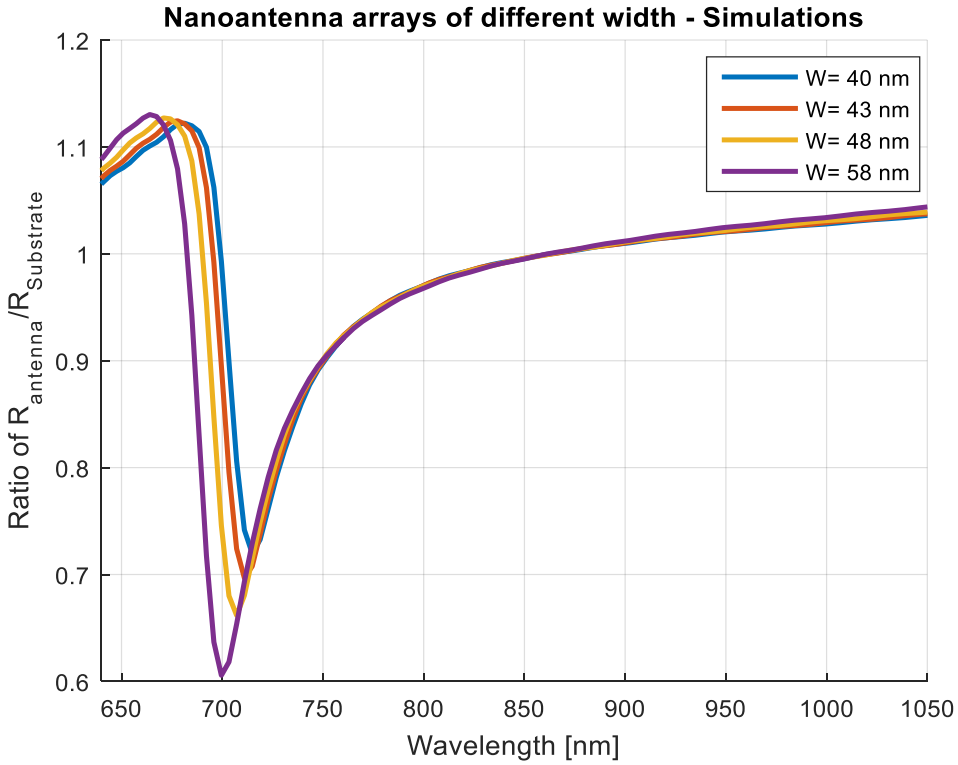

Figure 38 - Theoretical results of change of width and fixed length=85 nm obtained using Lumerical by Saba Mousavi

Another example of an area scan for nanoantenna of length $l = 84.82$ nm and width $w = 42.72$ nm at a wavelength of 760 nm can be seen in Figure 39. If one compares the substrate to the nanoantenna array intensity it is equivalent to that of Figure 37. Thus, one can conclude that this nanoantenna array does in fact resonate at 760 nm since the intensity of the nanoantenna is lower than that of the substrate.

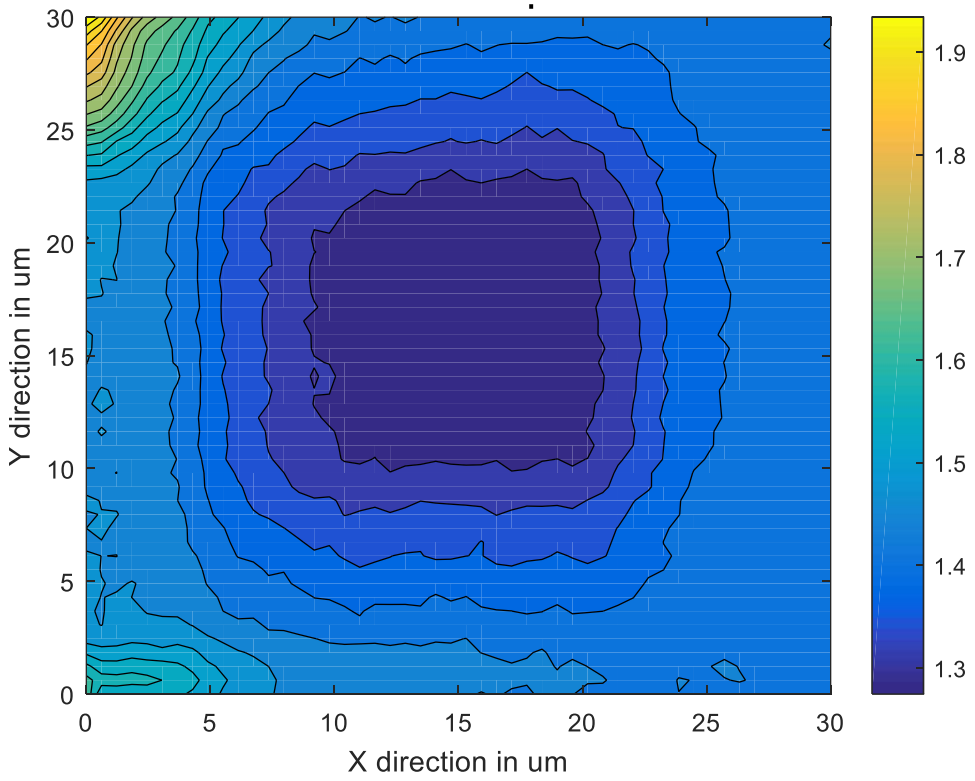

Figure 39 – Area scan nanoantenna array at 760 nm, of nanoantennas of length 84.82 nm and width 42.72 nm

4.4 Spontaneous Raman Measurements

This part of the work focuses on the spontaneous Raman spectrum obtained from the optical setup for nanoantennas on graphene. We compare our results to those obtained with a commercial WiTec Alpha 300A Raman spectrometer system. The first part of this section compares graphene and Silicon Raman peaks, as discussed in Sections 2.1 and 2.4. The second part determines the enhancement in graphene Raman scattering due to overlapping metallic nanostructures of different geometries.

4.4.1 Graphene on Si

Whilst building the optical setup, the optics in the spectrometer arm were aligned to the He-Ne light. As a result, trying to find the Raman signal of graphene initially was challenging due to the mismatch of the focal points, reflectance angles and the weakness of the signal. The Raman scattering from Si however known to have a much higher strength than the graphene D, 2D and G peak. Therefore, the most efficient way to optimise alignments in the set-up (particularly coupling the fiber to the focal point on the sample) is to start with the Si peak.

The Si-Si bonds are widely recognized as producing a sharp and intense peak at $\sim 520\ \mathrm{cm}^{-1}$ Raman shift. Si also has a higher-order silicon peak (2-Si) near $970\ \mathrm{cm}^{-1}$. The two silicon peaks can be seen in Figure 40, labeled Si and 2-Si, respectively, as obtained from our optical setup. At this step one can adjust the coupling of the fiber to the objective lens to attain a near-optimal system that is coupled to the Raman signal of the sample as opposed to the reflected pump laser line.

Finally, to acquire maximum Si power, the focal point of the laser spot on the sample is moved iteratively until a maximum signal is reached. This is due to the fact that different wavelengths focus at different points (pump laser versus Raman signal). The WiTec system required the same adjustments to the focal point as in our constructed system, After maximizing the Si signal the graphene G and 2D peak started appearing as can be seen in Figure 41. The Si and graphene Raman shifts for an excitation wavelength of 632.8 nm are:

$525.1\ \text{cm}^{-1} \rightarrow 654.55\ \text{nm}$, $952.3\ \text{cm}^{-1} \rightarrow 673.38\ \text{nm}$, $1599\ \text{cm}^{-1} \rightarrow 704.04\ \text{nm}$, and $2655\ \text{cm}^{-1} \rightarrow 760.58\ \text{nm}$. Comparing this to data obtained using the WiTec tool (also used by Ghamsari *et al.*, [6]) as shown in Figure 41 suggests that the results are in agreement.

Following the same approach to optimise acquisition of the Si Raman signal, we optimised the acquisition of the graphene Raman signal. Thus, the piezo stage was utilized to allow for finer movements. This was required because the device comprises many layers, thus different layers have different focal points. Furthermore, graphene is very thin, thus requiring a more precise focusing approach. It was found that from the point of maximum silicon peak intensity to maximum graphene peak intensity the difference in focal height (z direction) is about $5.8\ \mu\text{m}$ towards the top of the sample. It's important to note that during these measurements our main attention was on the 2D peak. This is due to the fact that all carbon material exhibit a peak at $1599\ \text{cm}^{-1}$ but only graphene does at $2655\ \text{cm}^{-1}$. The graphene Raman peaks after optimising the signal acquisition can be seen in Figure 42.

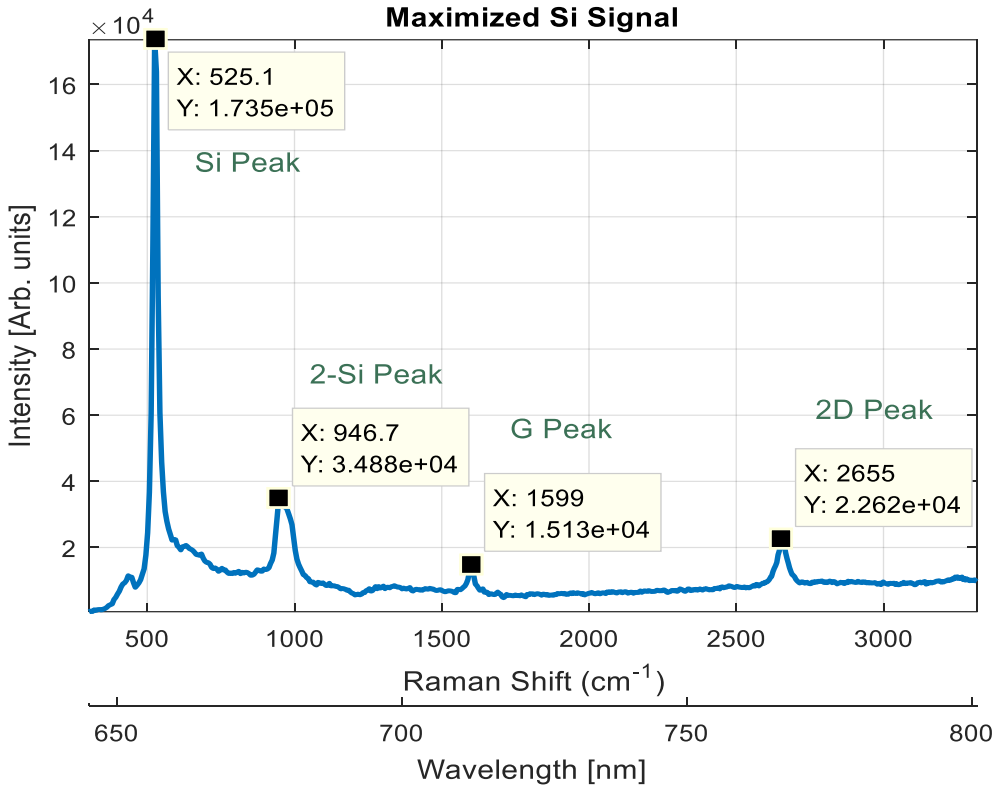

Figure 40 – Raman signal of graphene and Si when the Si signal is maximized by changing the focus of the laser

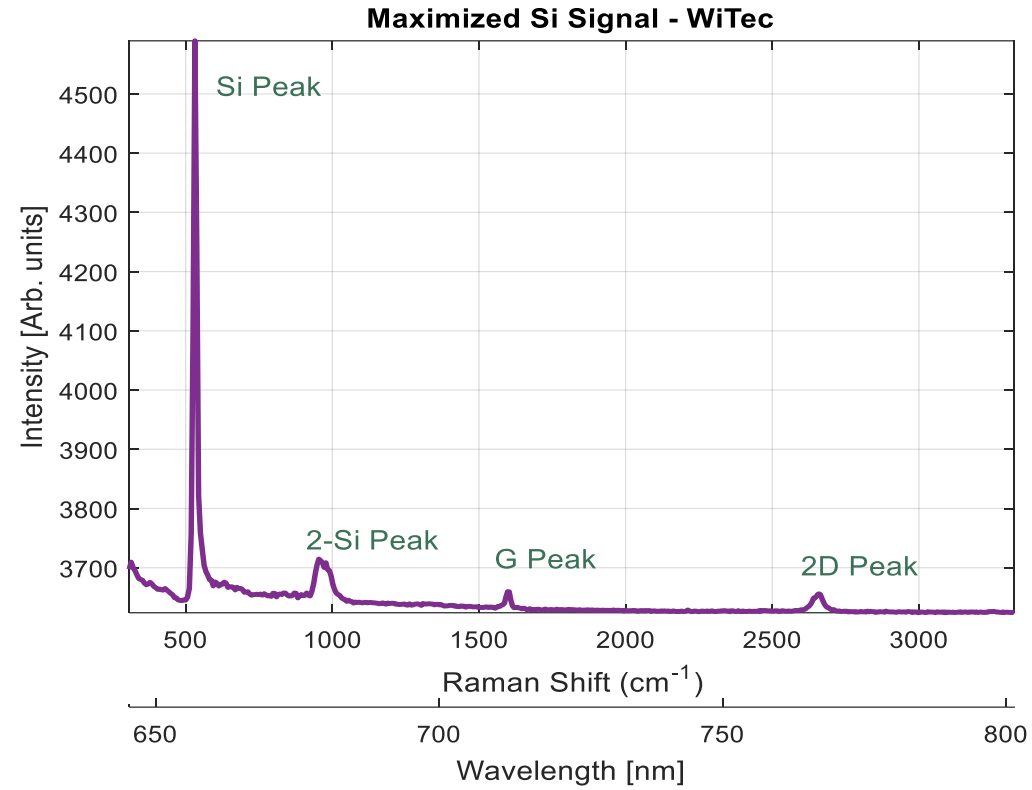

Figure 41 - Raman signal when Si is maximized by changing the focus, obtained using the WiTEC system

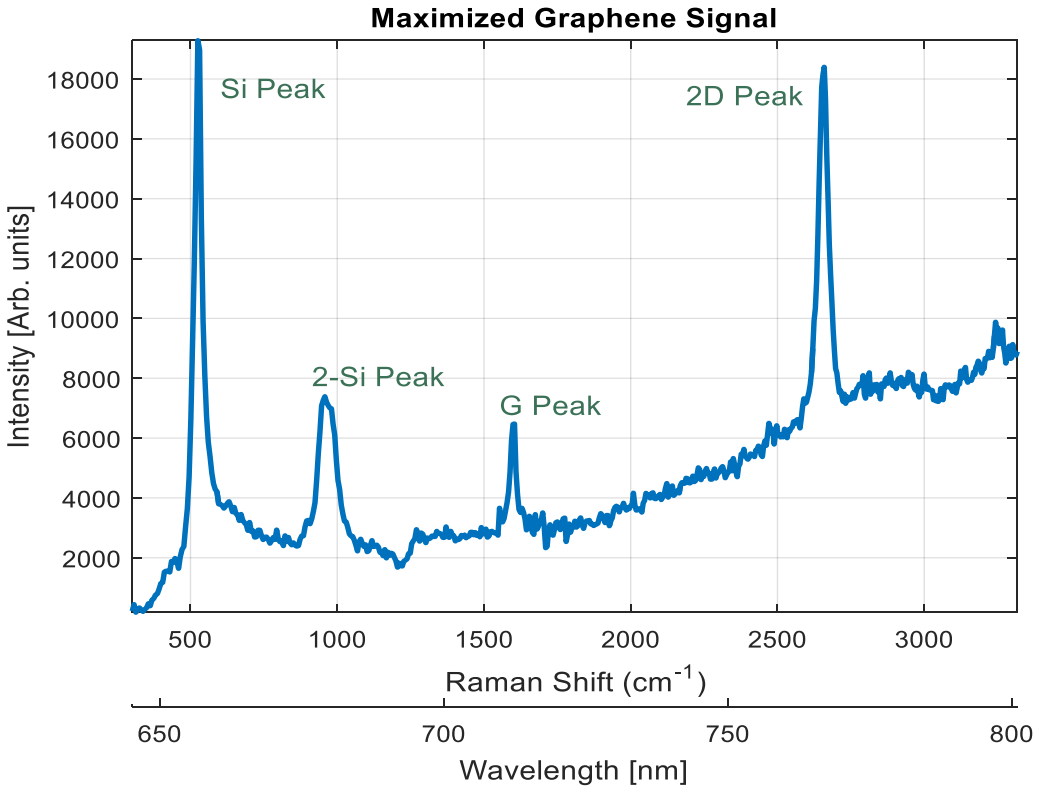

Figure 42 - Raman signal of graphene and Si when the graphene signal is maximized by changing the focus of the laser

As previously done, the Raman spectrum obtained from the setup can be compared to that obtained using the WiTec instrument by comparing Figure 42 with Figure 43. During the WiTec measurements the signal acquisition optimisation was based on maximizing the G and 2D peaks simultaneously. Note that the intensity bars will change based on number of pixels, gate time and the post processing calculations, thus they are only used for ratio observation and not for comparison purposes since the units are arbitrary.

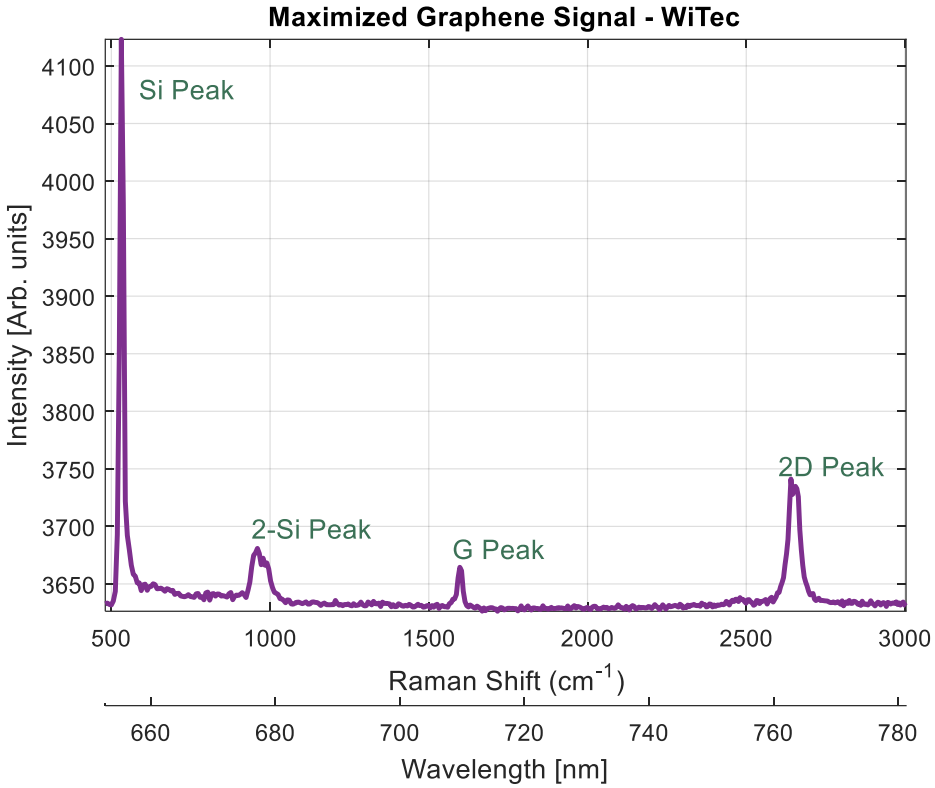

Figure 43- Raman signal when graphene is maximized by changing the focus, obtained through WiTEC

To have an efficient and comparable Raman microscope to commercial ones, the integration time should be fairly short. This allows the adjustment of the focal point and fiber coupling more rapidly with an almost instantaneous spectrum response. If the response time is longer than 1 second the system is lacking in speed.

The comparison of the shape and Raman shift of the four peaks can be seen in Figure 44, Figure 45, Figure 46 and Figure 47. From which one can conclude that the experimental results agree with the WiTec results.

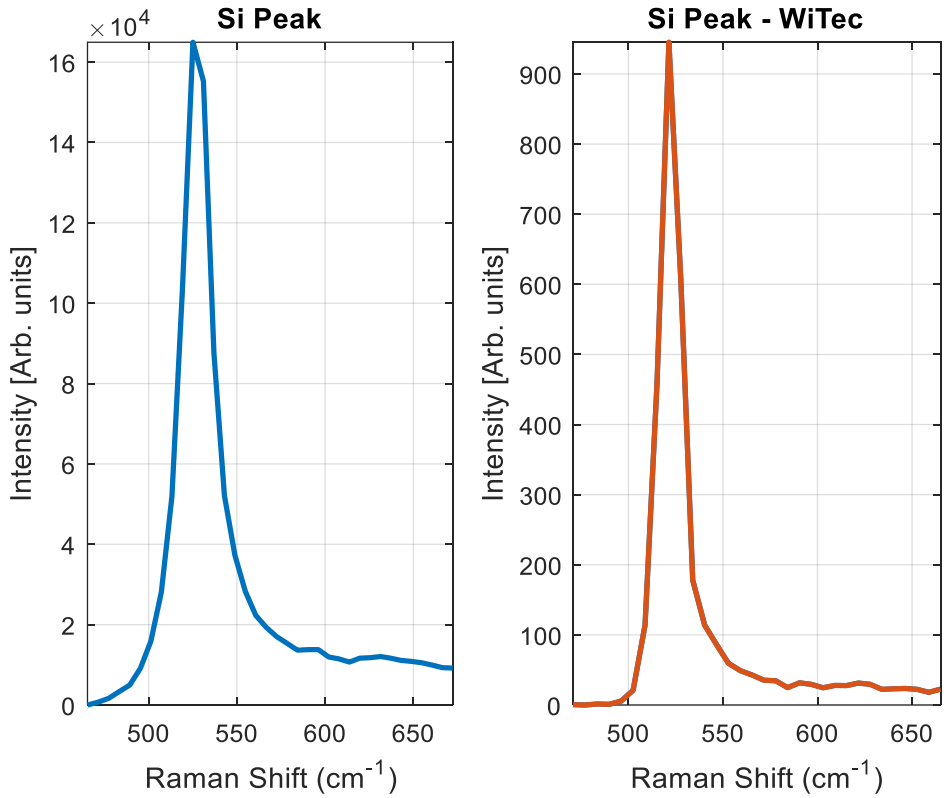

Figure 44 - Comparing Si peak obtained from WiTech with that obtained from this built setup

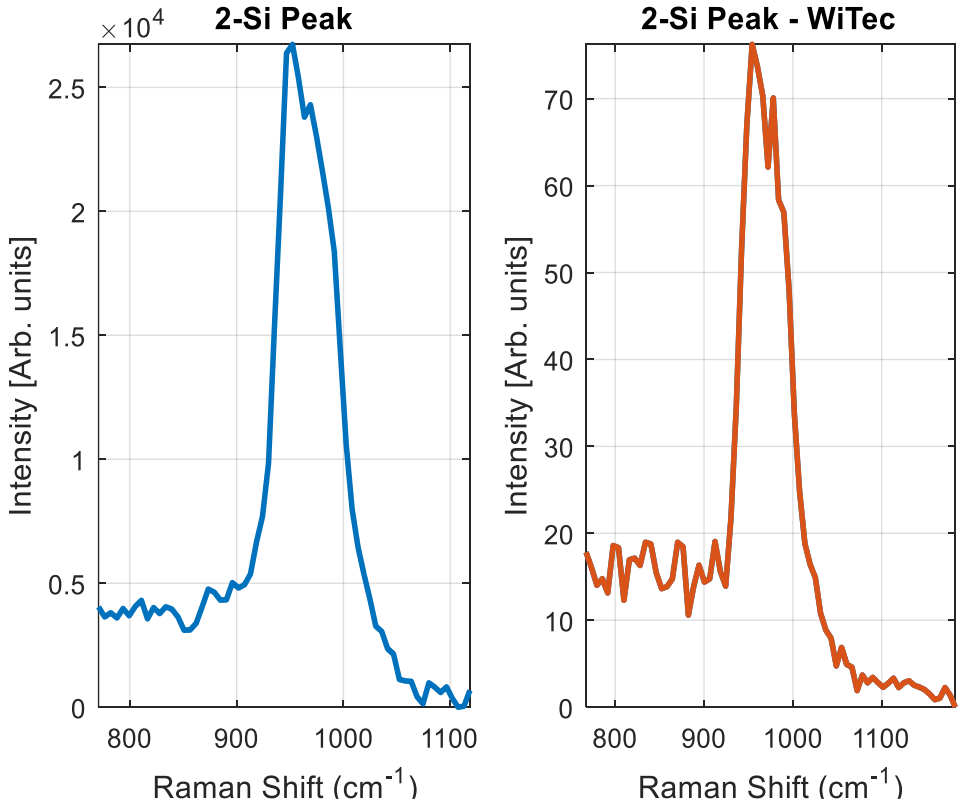

Figure 45 - Comparing 2-Si peak obtained from WiTech with that obtained from this built setup

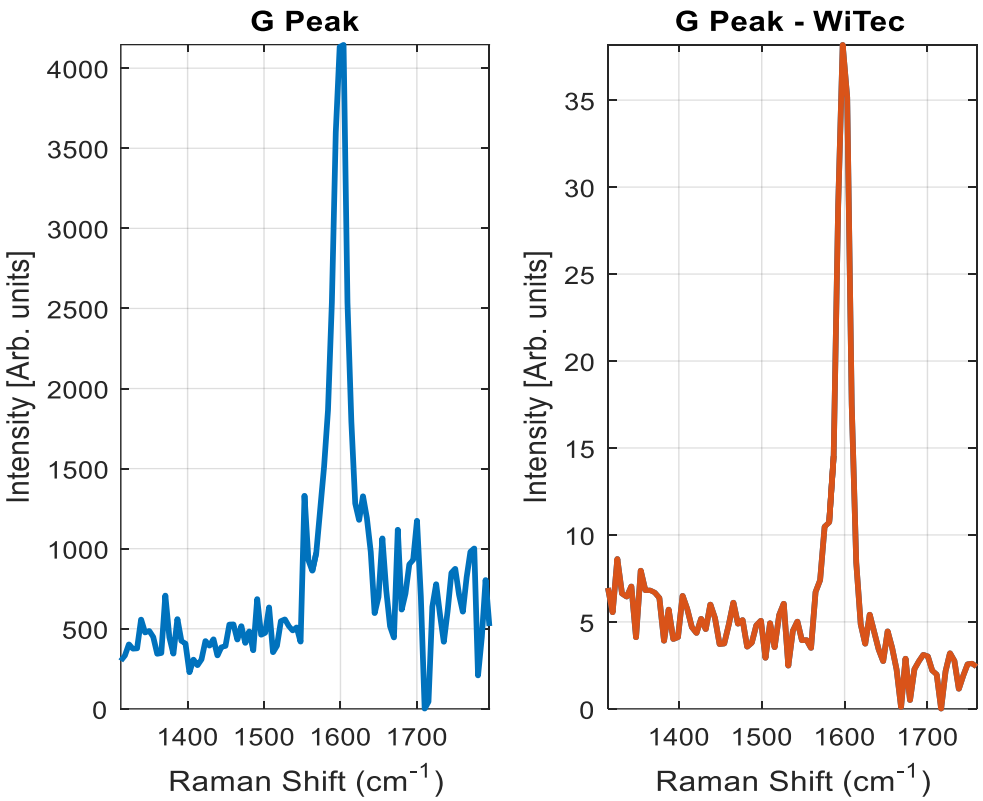

Figure 46 - Comparing graphene G peak obtained from WiTech with that obtained from this built setup

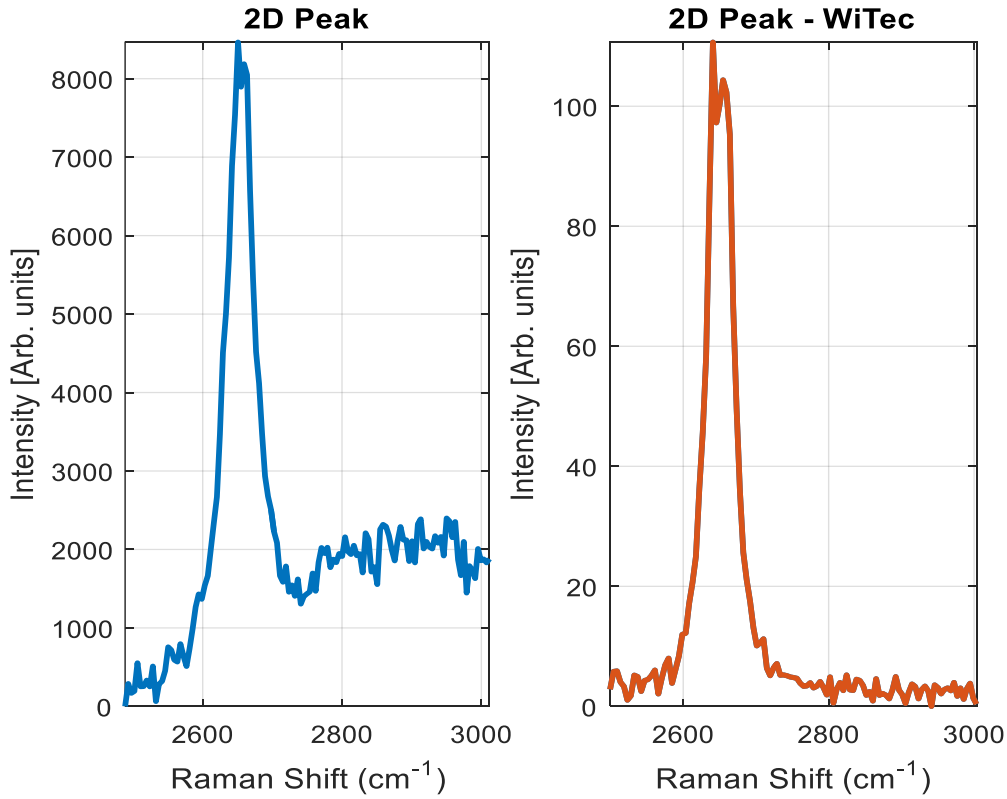

Figure 47 - Comparing graphene 2D peak obtained from WiTech with that obtained from this built setup

For graphene, the ratio of the intensity of the 2D peak to that of the G peak should be:

$$\frac{I_{2D}}{I_G} \cong 2 \qquad (4.\ 12).$$

which is indeed observed by comparing Figure 46 with Figure 47. As previously discussed [38], the D peak from graphene is only seen when there are impurities or imperfections in a carbon material. Others have also noticed that imperfections occur more prominently in samples that have gone through the process of fabrication and annealing. The D peak was observed around the regions bearing fabricated nanoantennas, as seen in Figure 48. The figure only shows one row of the CCD camera since the signal is very week and would be overpowered by the Si Peak, and averaging all the rows will reduce the visibility. The peak was found at wavelength 691 nm or Raman shift 1331 cm^{-1} as the literature would suggest for graphene.

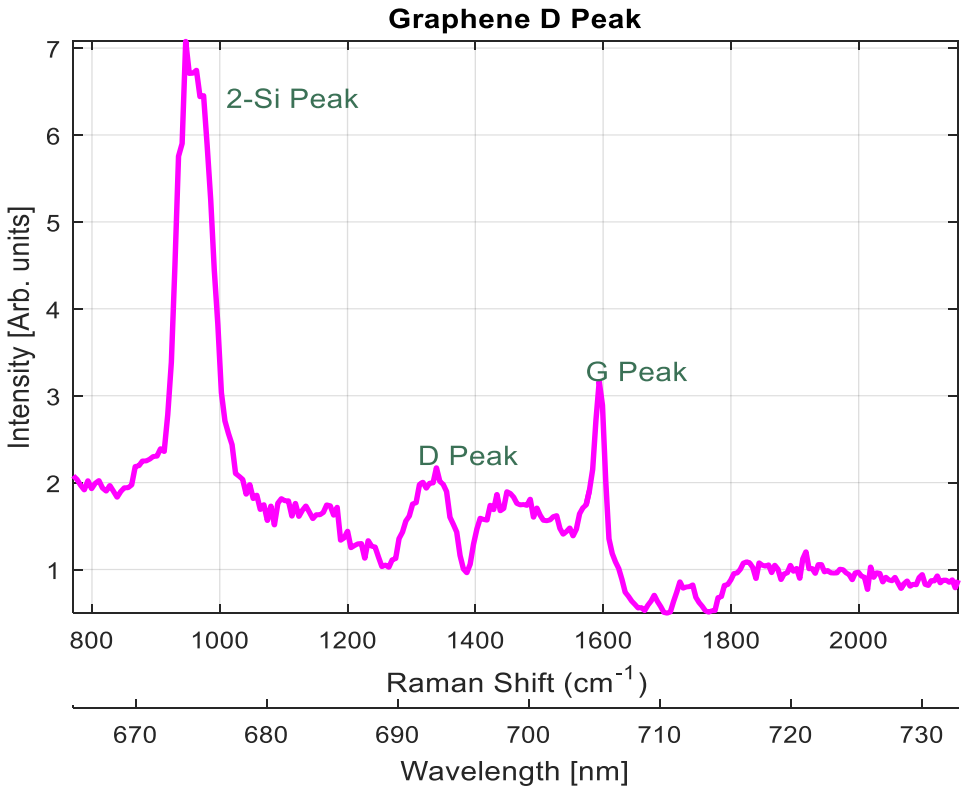

Figure 48 - The graphene D peak near the nanoantenna region

The last quality and verification check conducted was testing a sample that only contained Si without the addition of graphene to prove that the signals seen previously were in fact a result of graphene. The expected spectrum would contain the two Si peaks without any other peaks in the spectrum. This can be seen in Figure 49.

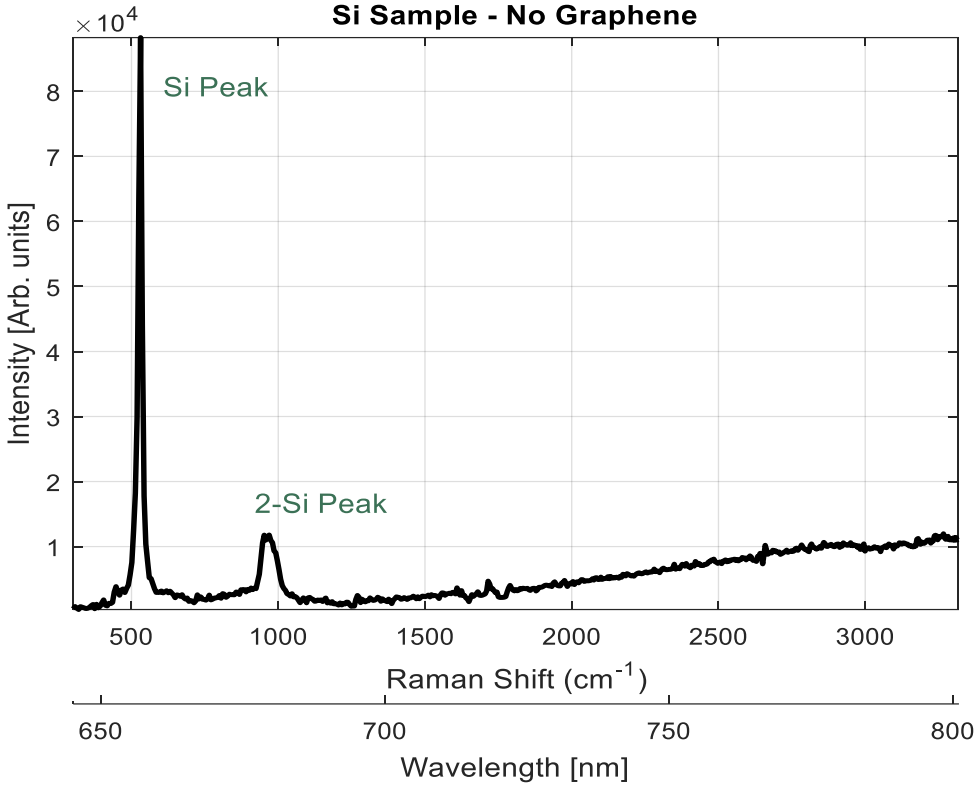

Figure 49 - Raman signal of a silicon sample without the presence of graphene

4.4.2 Nanoantenna Enhancement per Array of Graphene Raman Peak

The final part of this study is showing the effect of metallic nanostructures on the graphene Raman signal. Nanoantennas with varying lengths and widths were used to show such effects, (signal enhancement), on the graphene 2D peak. Here we investigate the case where the nanoantennas resonate in coincidence with the Stokes emission (2D peak), following Ghamsari *et al*. [6], as opposed to the more common approach of aligning the nanoantennas spectrally with the pump laser.

Figure 50 is a representative spectrum of the effect of metallic nanostructures. As the nanoantenna resonance wavelength approaches 760 nm (the wavelength of the 2D peak for a pump laser at 632.8 nm), a broad feature appears in the spectrum over the range of 650 to 700 nm, due to the high reflectivity of metals, Au in this case, and multiple Raman signals at different wavelengths. When measuring nanoantennas that are either very long or very short the spectrum looked more like that of Figure 42 because the nanoantenna resonance was further from the 2D Raman shift as Figure 34 and Figure 37 would suggest.

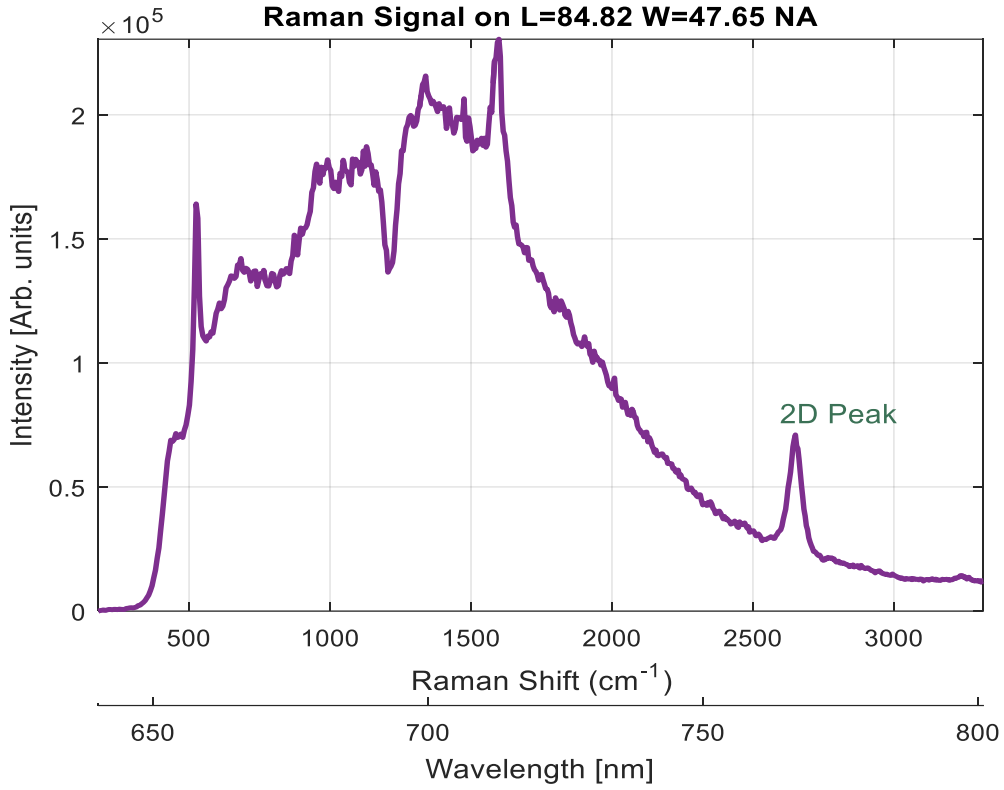

Figure 50 - Nanoantenna spectrum from 645 to 800 nm ; NA=Nanoantenna

Eight arrays of nanoantennas of different lengths but fixed width of $w = 47.65$ nm were utilized to reveal different enhancement factors, as shown in Figure 51 and Figure 52. If one compares those two figures to Figure 34 it is clear that as the optical resonance of the nanoantennas approach 760 nm the enhancement factor increases. It can be seen that for nanoantennas of lengths 84.82 nm and 100.1 nm that the base to peak intensity is from 0.8 to 5.2. Thus, the maximum enhancement factor seen is approximately 6.5 compared to graphene without nanoantenna structures. Furthermore, another way to represent the enhancement factor as a function of length and wavelength is seen in Figure 53.

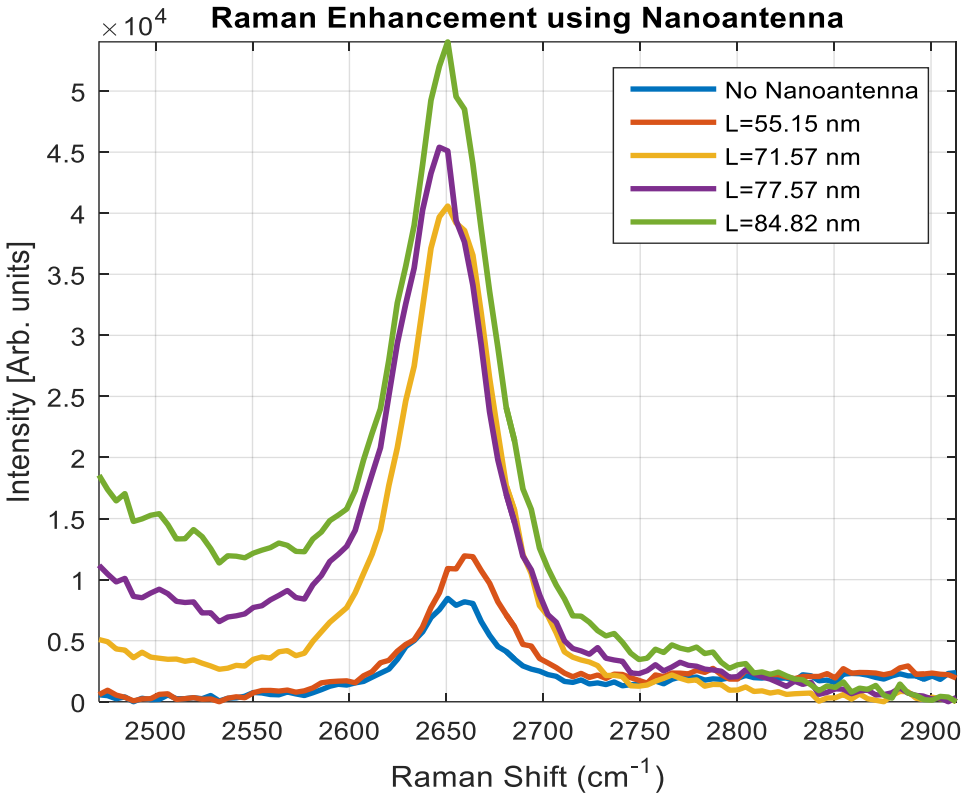

Figure 51 - Nanoantennas of different lengths L=xx nm and fixed width w=47.65 nm

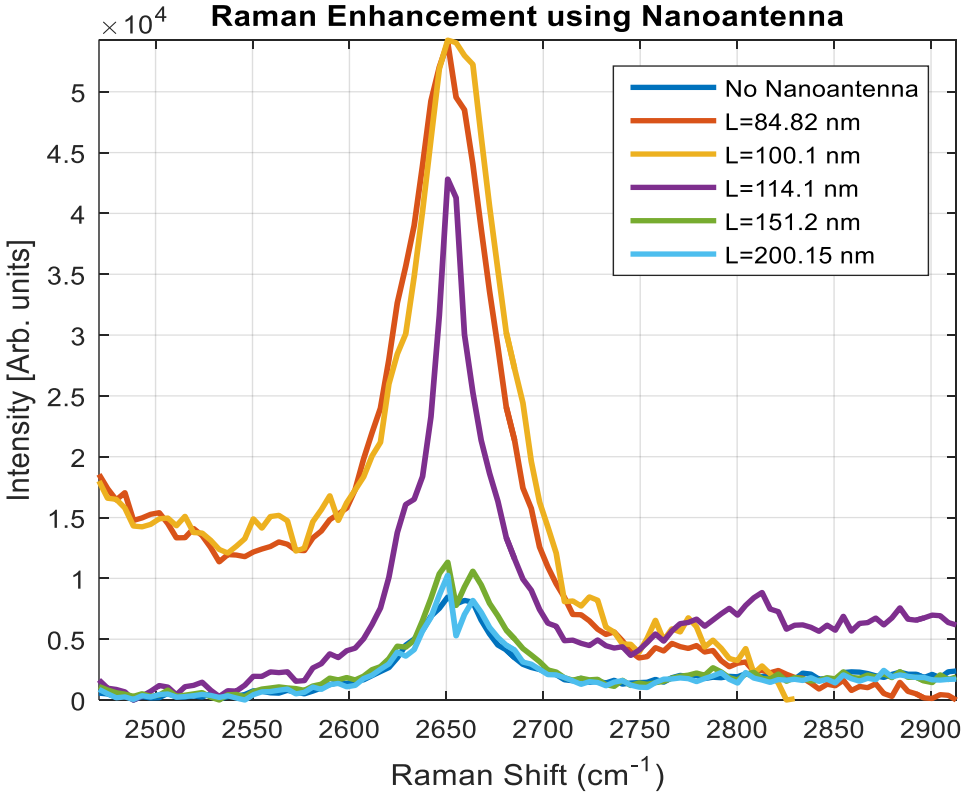

Figure 52 - Nanoantennas of different lengths L=xx nm and fixed width w=47.65 nm

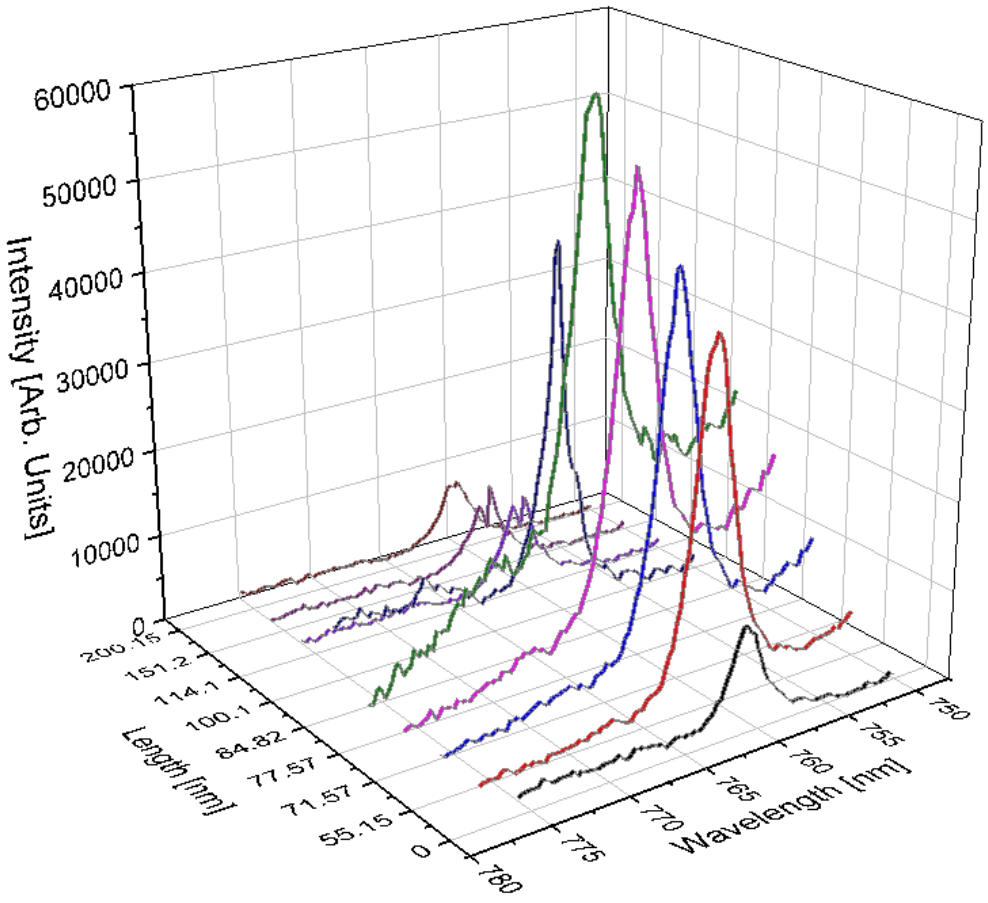

Figure 53 - Nanoantennas of different lengths L=xx nm and fixed width w=47.65 nm

Comparing the two longest nanoantenna 2D spectra to the bare graphene spectrum it is clear that they provide little to no enhancement as seen in Figure 54. Furthermore, it was seen in Figure 36 that longer nanoantennas have a very small resonance ratio and those may not provide enhancement. Also these nanoantennas resonate somewhere near 950 nm and longer, thus much further than 760 nm. A final observation is that when using longer nanoantennas or when using no nanoantennas the 2D peak splits resolves into two peaks in accordance to the literature [38]. However, it was observed that the two peaks are more prominent for multilayer graphene or when it has impurities. Cancado *et al*. suggested that the two peaks arise from the convolution of an infinite number of peaks [38]. The two peaks have been assigned the nomenclature 2D(1) and 2D(2) at 760.24 nm and 762.38 nm. It is important to mention that the granularity of the wavelength is a step size of $0.3\overline{3}$ nm.

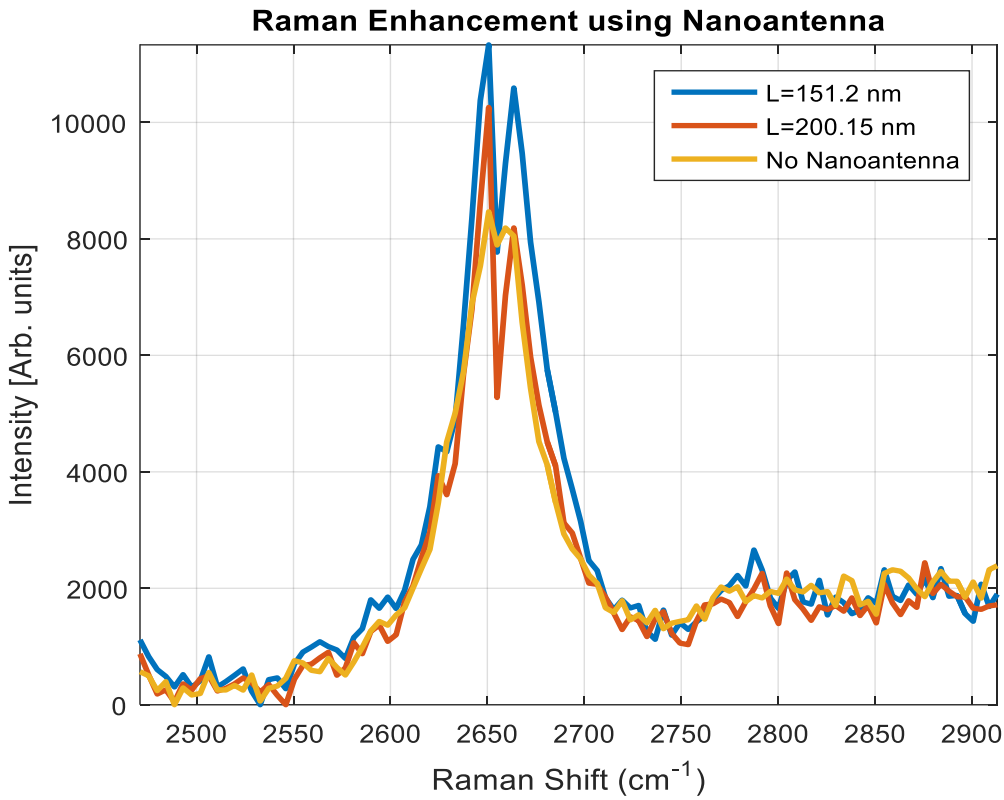

Figure 54 - Nanoantennas of longer length and fixed width w=47.65 nm with comparison to lack of nanoantennas

Four arrays of nanoantennas of different widths but fixed length were utilized to investigate the enhancement factors as shown in Figure 55. The length of the nanoantennas was selected as the one that showed the highest enhancement factor, $L = 84.82$ nm. It can be seen that for a width of $W = 42.72$ nm the enhancement factor is approximately 8.2 that of bare graphene without nanoantennas. This observation also agrees with Figure 37, suggesting that this array resonates closest to 760 nm.

Thus it is clear that the nanoantennas create enhancement in the 2D peak. The nanoantennas of dimensions $L = 84.82$ nm and $W = 42.72$ nm produced the largest enhancement factor of up to ~ 8.2 and is the set that that resonates closest to 760 nm as expected. The enhancement factor as a function of nanoantenna length and width is plotted in Figure 56 and Figure 57 respectively. Furthermore, comparing the enhancement factors from the work of Ghamsari *et al.* [6], it is evident that for the similar structures they only observed an enhancement factor or 2-3 using the Witec instrument. Thus, one can argue that the designed and constructed Raman microscope provided better enhancement through nanoantennas.

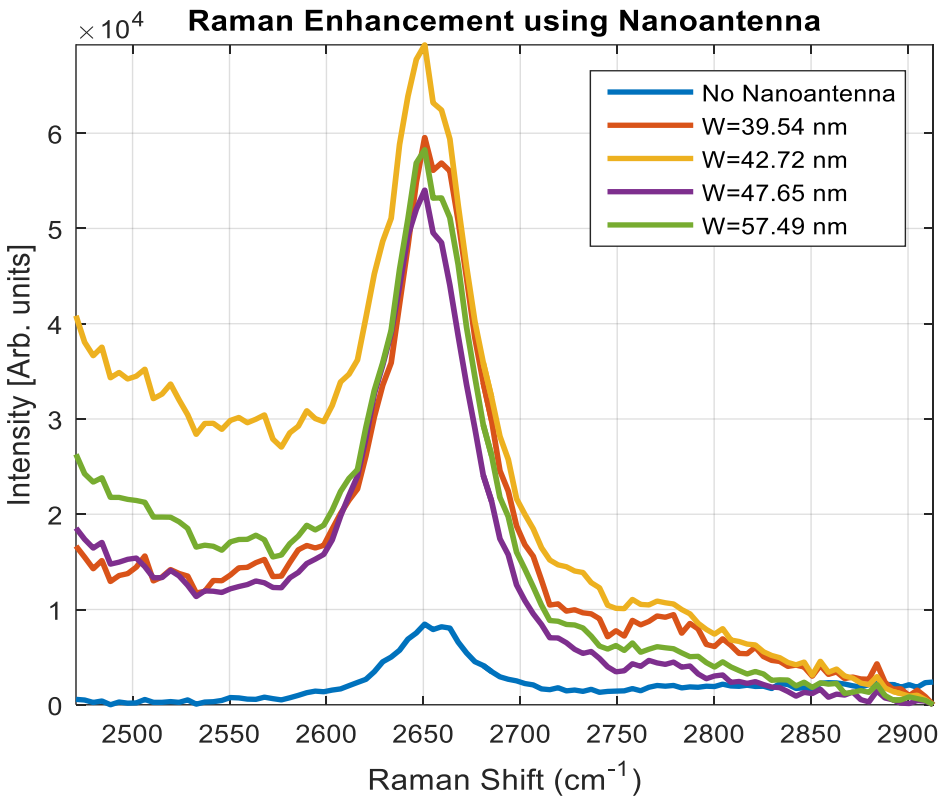

Figure 55 – Nanoantennas of different width w=xx nm and fixed length L=84.82 nm

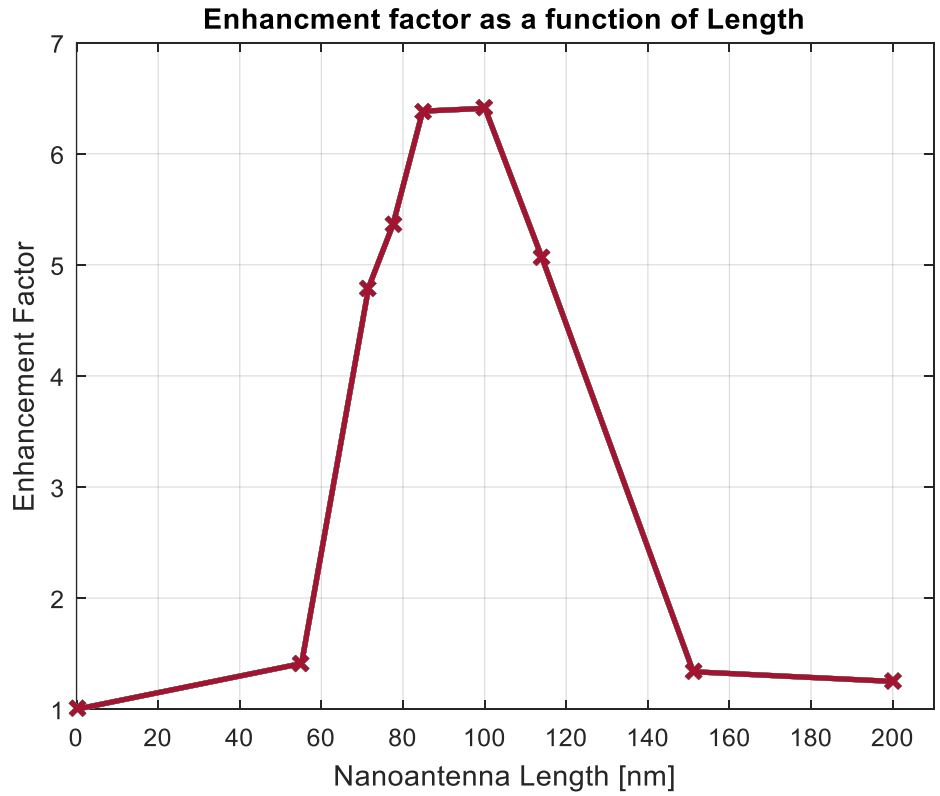

Figure 56 – Enhancement factor curve as a function of length and width W=47.65 nm

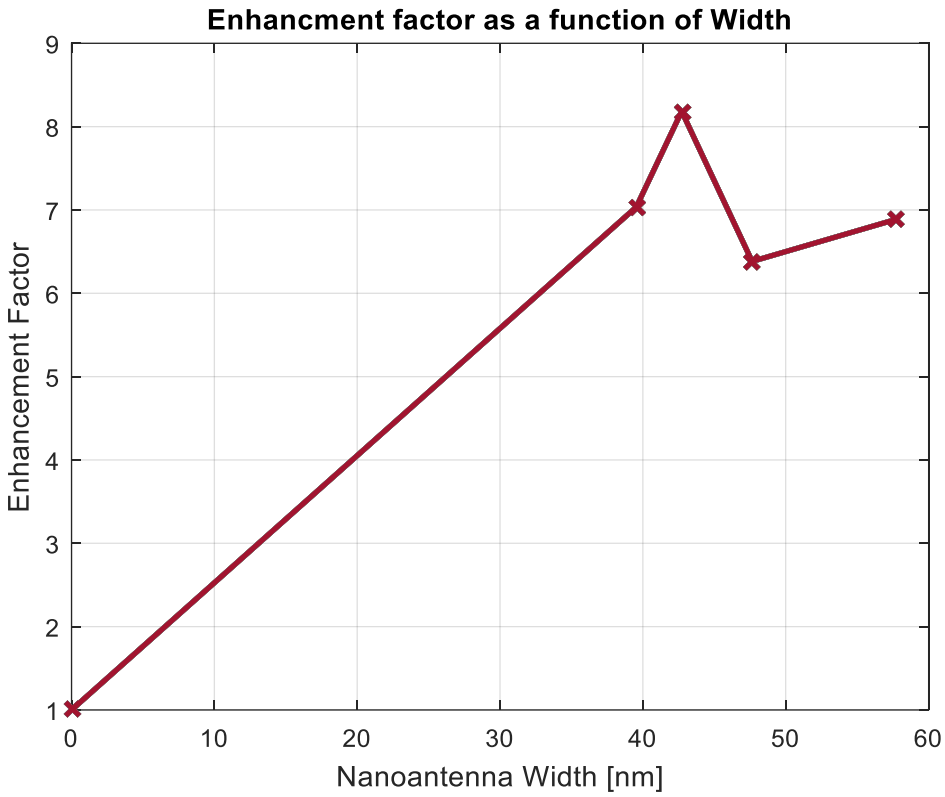

Figure 57 - Enhancement factor curve as a function of width and length L=84.82 nm

4.4.3 The Scattering Gain

The overall size of the nanoantenna's are not factored directly when calculating the enhancement. In plasmonic most applications require an array of nanostructures. Thus, from the enhancement factors of the nanoantenna arrays one should consider the enhancement per unit cell. Since nanoantennas are essentially antennas the plasmonic enhancement is equivalent to the scattering gain S_G [6]. This can be defined as the ratio of effective scattering cross-section A_{eff} and the geometric cross section A_g:

$$\mathrm{S_G} = \frac{\mathrm{A_{eff}}}{\mathrm{A_g}} = \frac{(\varepsilon - 1)\mathrm{A_0}}{\mathrm{A_g}} = \frac{\left(\frac{\mathrm{P_1}}{\mathrm{P_0}} - 1\right)\mathrm{A_0}}{\mathrm{A_g}} \tag{4. 13}$$

Where, P_0 is the Raman radiated power from an un-patterned array and P_1 and from a unit cell of antenna array A_0. This can be calculated for an array of dimensions $l = 84.82$ nm and $w = 42.72$ nm as,

$$S_G = \frac{\left(\frac{P_1}{P_0} - 1\right) A_0}{A_g} = \frac{(8.2 - 1) \times 500\ \text{nm} \times 500\ \text{nm}}{42.72\ \text{nm} \times 84.82\ \text{nm}} = 496.75 \quad (4.\ 14)$$

Figure 58 shows the scattering cross section as a function of length for the 2D peak. It is evident that the scattering cross section gain is as high as 350 for a single nanoantenna. Similar, Figure 59 shows the scattering cross section as a function of width for the 2D peak. Thus, it is evident that the maximum scattering cross section achieved is 496.

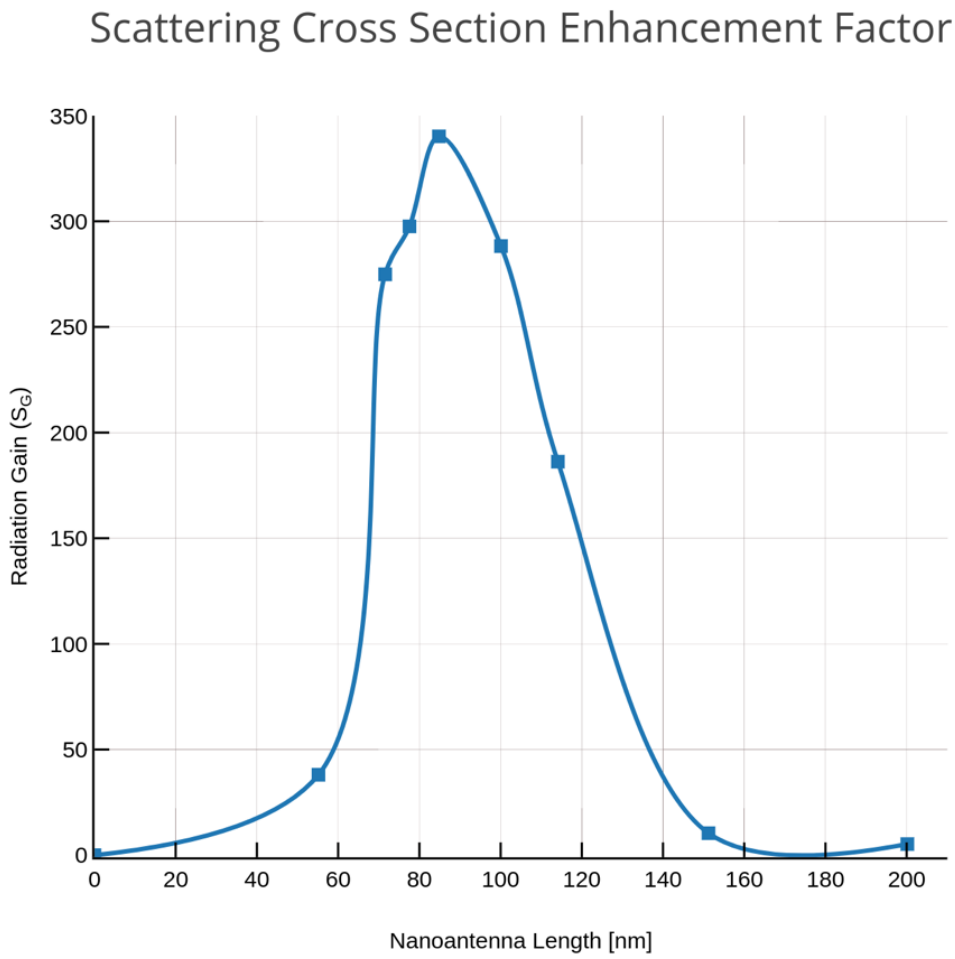

Figure 58 – Scattering Cross section enhancement for different length nanoantennas with width w=47.65 nm

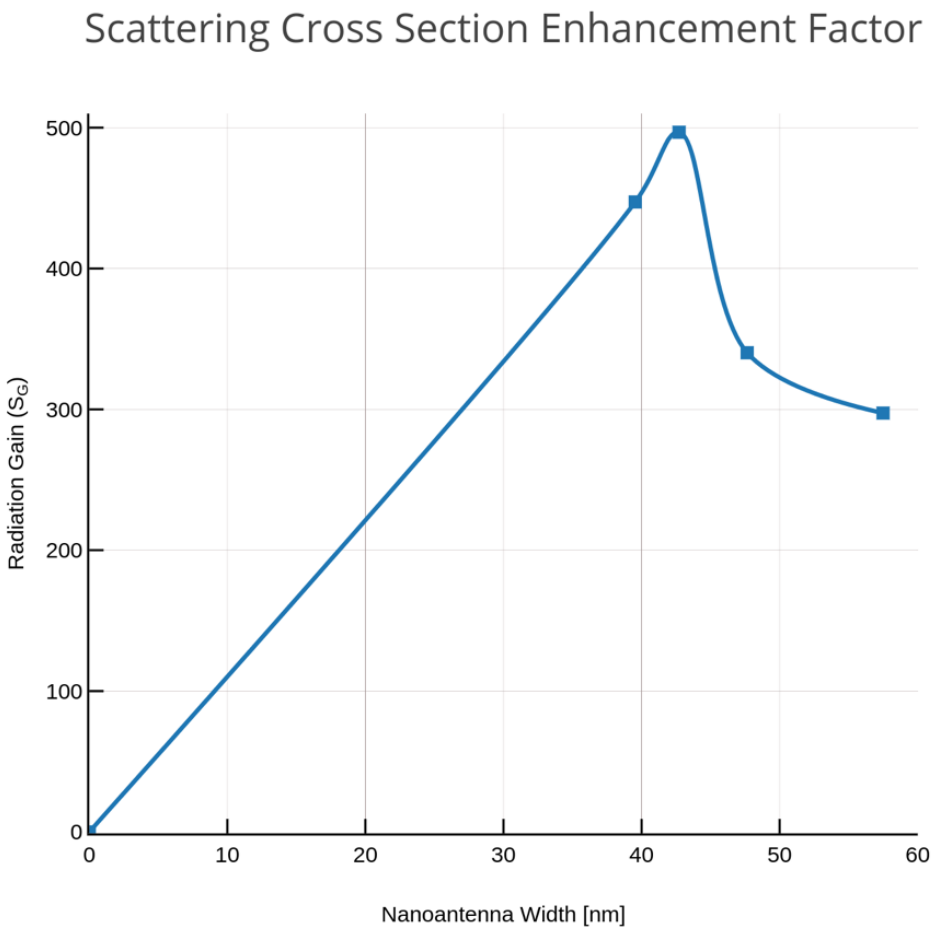

Figure 59 - Scattering Cross section enhancement for different width nanoantennas with length l=84.82 nm

Chapter 5 – Conclusion

5.1 Thesis Conclusion and Contributions

In conclusion, all arms of the spectroscopy tool were shown to work effectively and efficiently for the fabricated devices, demonstrating the usefulness of the tool. The devices used comprise arrays of rectangular Au nanoantennas of length *l*, width *w* and thickness *t*, on graphene on SiO_2/Si. The antennas are arranged over the surface following pitch *p* and *q*. Fabrication was achieved using e-beam lithography, evaporation and lift-off on CVD grown graphene.

The stimulated Raman arm was utilized to conduct reflectance measurements on different nanoantennas of different geometries. It was seen that for a constant width, as the length increases the optical resonance shifts towards a higher wavelength. Alternatively, as the width increases and the length remains constant the resonance moves towards shorter wavelengths. It was concluded that a nanoantenna of dimensions $l = 84.82$ nm and $w = 42.72$ nm resonated closest to the wavelength of 760 nm. The significance of $760\ nm$ rests in the second part of the thesis - this is the wavelength of the 2D Raman peak of graphene for an excitation wavelength of 632.8 nm.

The constructed system is capable of capturing Raman scattered signals from both Si and graphene with high accuracy and comparable quality to a commercial WiTec Raman microscope. The G and 2D peaks for graphene were visible at $1599\ \text{cm}^{-1}$ and $2655\ \text{cm}^{-1}$ respectively, which is equivalent to ~ 704.1 nm and ~ 760.6 nm for an excitation wavelength of 632.8 nm.

Finally, enhancement of the Raman scattering was achieved by exploiting surface plasmon polaritons on nanoantennas to enhance the interaction between graphene and light. The enhancement was established exclusively by the resonant Stokes emission overlapping spectrally and spatially with Au nanoantennas. It was found that as the optical resonance of the antenna approaches 760 nm the enhancement factor for the 2D signal became larger. The enhancement factor for nanoantennas of dimensions $l = 84.82$ nm and $w = 42.72$ nm was approximately 8.2 per antenna array compared to bare graphene and a scattering cross section

gain of ~500. This scattering cross is higher than the one obtained by Ghamsari *et al*., which was approximately 160 [6].

The initial idea and design of the optical setup was acquired from Behnood Ghamsari. However, during my construction of the setup there was significant addition and removal of components as deemed necessary. The structures were fabricated by Anthony Olivieri and designed by myself following Ghamsari's *et al*. [6]. Lastly, the simulations were provided by Saba Saidat and the Witec measurements were acquired with the assistance of Jaspreet Walia. All other results shown in this thesis were obtained by myself including the reflectance measurements, SEM measurements, Raman measurements and Raman enhancement measurements.

The tool constructed can be used for a wide range of applications and can be shared amongst researchers in the lab thus serving as a tool beneficial to several projects. In conclusion, the novelty of this work can be summarized as follows,

- The construction of a new functioning setup for spontaneous and stimulated Raman scattering measurements.
- The construction of a setup for normalized reflectance measurements.
- Acquired normalized reflectance measurements from nanoantennas on graphene.
- Successfully measured enhanced Raman scattering from graphene using nanoantenna arrays with a scattering gain of ~ 500.

5.2 Future Work

After constructing the spectroscopy tool and showing its effectiveness for reflectance measurements and enhanced spontaneous Raman scattering, the next step is to exploit the full utility of the tool to conduct stimulated Raman measurements. Furthermore, there are a plethora of devices to conduct stimulated and spontaneous Raman experiments on, ranging from, but not exclusive to, different shapes of metallic nanostructures on graphene to different materials or substrates. Another useful and easy addition is the utilization of a notch filter to explore the anti-Stokes signals emitted from the device. The extension of the optical setup to add more pump laser sources can also prove to be beneficial for other Raman applications, or one can utilize the supercontiumm source with filtering as a pump instead of a probe.

References

[1] G. V. P. Kumar, "Plasmonic nano-architectures for surface enhanced Raman scattering: a review," *J. Nanophotonics*, vol. 6, no. 1, p. 064503, 2012.

[2] M. I. Stockman, "Nanoplasmonics: past, present, and glimpse into future," *Opt. Express*, vol. 19, no. 22, pp. 22029–22106, 2011.

[3] B. G. Ghamsari and P. Berini, "Surface plasmon near-field back-action and displacement of enhanced Raman scattering spectrum in graphene," *J. Opt. (United Kingdom)*, vol. 18, no. 7, 2016.

[4] F. H. L. Koppens, D. E. Chang, and F. J. García De Abajo, "Graphene plasmonics: A platform for strong light-matter interactions," *Nano Lett.*, vol. 11, no. 8, pp. 3370–3377, 2011.

[5] F. J. G. De Abajo, "Graphene plasmonics: Challenges and opportunities," *ACS Photonics*, vol. 1, no. 3, pp. 133–152, 2014.

[6] B. G. Ghamsari, A. Olivieri, F. Variola, and P. Berini, "Enhanced Raman scattering in graphene by plasmonic resonant Stokes emission," *Nanophotonics*, vol. 3, no. 6, pp. 363–371, 2014.

[7] K. Kneipp, H. Kneipp, I. Itzkan, R. R. Dasari, and M. S. Feld, "Surface-enhanced Raman scattering and biophysics," vol. 14, pp. 597–624, 2002.

[8] A. Otto, I. Mrozek, H. Grabhorn, and W. Akemann, "Surface Enhanced Raman Scattering," *J. Phys. Condens. Matter*, vol. 4, no. 5, p. 1143, 1992.

[9] M. Fleischmann, P. J. Hendra, and a. J. McQuillan, "Raman spectra from electrode surfaces," *J. Chem.Soc, Chem. Commun.*, no. 80, pp. 80–81, 1973.

[10] D. L. Jeanmaire, M. R. Suchanski, and R. P. Van Duyne, "Resonance Raman Spectroelectrochemistry. I. The Tetracyanoethylene Anion Radical," *J. Am. Chem. Soc.*, vol. 97, no. 7, pp. 1699–1707, 1975.

[11] M. Fleischmann, P. J. Hendra, and A. J. McQuillan, “Raman spectra of pyridine adsorbed at a silver electrode,” *Chem. Phys. Lett.*, vol. 26, no. 2, pp. 163–166, 1974.

[12] D. L. Jeanmaire and R. P. Van Duyne, “Surface raman spectroelectrochemistry: Part I. Heterocyclic, aromatic, and aliphatic amines adsorbed on the anodized silver electrode,” *J. Electroanal. Chem.*, vol. 84, no. 1, pp. 1–20, 1977.

[13] R. P. Van Duyne, “Laser excitation of Raman scattering from adsorbed molecules on electrode surfaces,” in *Chemical and biochemical applications of lasers*, 4th ed., 1979, pp. 101–85.

[14] C. L. Haynes, C. R. Yonzon, X. Zhang, and R. P. Van Duyne, “Surface-enhanced Raman sensors: Early history and the development of sensors for quantitative biowarfare agent and glucose detection,” *J. Raman Spectrosc.*, vol. 36, no. 6–7, pp. 471–484, 2005.

[15] F. W. King, R. P. Van Duyne, and G. C. Schatz, “Theory of Raman scattering by molecules adsorbed on electrode surfaces,” *J. Chem. Phys.*, vol. 69, no. 10, pp. 4472–4481, 1978.

[16] a. M. Weiner, D. E. Leaird, G. P. Wiederrecht, and K. a. Nelson, “Femtosecond multiple-pulse impulsive stimulated Raman scattering spectroscopy,” *J. Opt. Soc. Am. B*, vol. 8, no. 6, p. 1264, 1991.

[17] Z.-Q. Tian and B. Ren, “Adsorption and Reaction At Electrochemical Interfaces As Probed By Surface-Enhanced Raman Spectroscopy,” *Annu. Rev. Phys. Chem.*, vol. 55, no. 1, pp. 197–229, 2004.

[18] A. J. McQuillan, “The discovery of surface-enhanced Raman scattering,” *Notes Rec. R. Soc.*, vol. 63, no. 1, pp. 105–109, 2009.

[19] R. Aroca, *Surface-enhanced Vibrational Spectroscopy*. John Wiley & Sons, 2006.

[20] E. C. Le Ru, E. Blackie, M. Meyer, and P. G. Etchegoint, “Surface enhanced raman scattering enhancement factors: A comprehensive study,” *J. Phys. Chem. C*, vol. 111,

no. 37, pp. 13794–13803, 2007.

[21] L. Gunnarsson, S. Petronis, B. Kasemo, H. Xu, J. Bjerneld, and M. Käll, "Optimizing nanofabricated substrates for surface enhanced Raman scattering," *Nanostructured Mater.*, vol. 12, no. 5, pp. 783–788, 1999.

[22] H. X. Xu, E. J. Bjerneld, M. Käll, and L. Börjesson, "Spectroscopy of single hemoglobin molecules by surface enhanced Raman scattering," *Phys. Rev. Lett.*, vol. 83, pp. 4357–4360, 1999.

[23] L. Novotny and N. Van Hulst, "Antennas for light," *Nat. Photonics*, vol. 5, no. 2, pp. 83–90, 2011.

[24] P. Bharadwaj, B. Deutsch, and L. Novotny, "Optical Antennas," *Adv. Opt. Photonics*, vol. 1, no. 3, p. 438, 2009.

[25] L. Novotny, "Effective wavelength scaling for optical antennas," *Phys. Rev. Lett.*, vol. 98, no. 26, pp. 1–4, 2007.

[26] J. Wessel, "Surface-enhanced optical microscopy," *J. Opt. Soc. Am. B*, vol. 2, no. 9, pp. 1538–1541, 1985.

[27] L. Tang *et al.*, "Nanometre-scale germanium photodetector enhanced by a near-infrared dipole antenna," *Nat. Photonics*, vol. 2, no. 4, pp. 226–229, 2008.

[28] J. Alda, J. M. Rico-García, J. M. López-Alonso, and G. Boreman, "Optical antennas for nano-photonic applications," *Nanotechnology*, vol. 16, no. 5, 2005.

[29] S. Nie and S. R. Emory, "Probing Single Molecules and Single Nanoparticles by Surface-Enhanced Raman Scattering Probing Single Molecules and Single Nanoparticles by Surface-Enhanced Raman Scattering," vol. 1102, no. 1997, 2009.

[30] K. Kneipp, Y. Wang, H. Kneipp, L. T. Perelman, and I. Itzkan, "Single molecule detection using surface-enhanced Raman scattering (SERS)," *Phys. Rev. ...*, vol. 78, no. 9, pp. 1667–1670, 1997.

[31] A. Hartschuh, H. Qian, A. J. Meixner, N. Anderson, and L. Novotny, “Tip-Enhanced optical spectroscopy of single-walled carbon nanotubes,” in *Tip Enhancement*, Elsevier, 2007, pp. 157–176.

[32] N. Anderson, A. Hartschuh, and L. Novotny, “Chirality changes in carbon nanotubes studied with near-field Raman spectroscopy,” *Nano Lett.*, vol. 7, no. 3, pp. 577–582, 2007.

[33] K. B. Crozier, A. Sundaramurthy, G. S. Kino, and C. F. Quate, “Optical antennas: Resonators for local field enhancement,” *J. Appl. Phys.*, vol. 94, no. 7, pp. 4632–4642, 2003.

[34] S. S. Mousavi, P. Berini, and D. McNamara, “Periodic plasmonic nanoantennas in a piecewise homogeneous background,” *Opt. Express*, vol. 20, no. 16, p. 18044, 2012.

[35] Y. Shao, J. Wang, H. Wu, J. Liu, I. A. Aksay, and Y. Lin, “Graphene based electrochemical sensors and biosensors: A review,” *Electroanalysis*, vol. 22, no. 10, pp. 1027–1036, 2010.

[36] V. Chabot, D. Higgins, A. Yu, X. Xiao, Z. Chen, and J. Zhang, “A review of graphene and graphene oxide sponge: Material synthesis and applications to energy and the environment,” *Energy Environ. Sci.*, vol. 7, no. 5, pp. 1564–1596, 2014.

[37] L. M. Malard, M. A. Pimenta, G. Dresselhaus, and M. S. Dresselhaus, “Raman spectroscopy in graphene,” *Phys. Rep.*, vol. 473, no. 5–6, pp. 51–87, 2009.

[38] A. C. Ferrari and D. M. Basko, “Raman spectroscopy as a versatile tool for studying the properties of graphene,” *Nat. Nanotechnol.*, vol. 8, no. 4, pp. 235–246, 2013.

[39] M. Allen, “Honeycomb carbon -- A study of graphene,” *Am. Chem. Soc.*, p. 184, 2009.

[40] S. Reich and C. Thomsen, “Raman spectroscopy of graphite,” *Philos. Trans. R. Soc. A Math. Phys. Eng. Sci.*, vol. 362, no. 1824, pp. 2271–2288, 2004.

[41] A. C. Ferrari *et al.*, "Raman spectrum of graphene and graphene layers," *Phys. Rev. Lett.*, vol. 97, no. 18, pp. 1–4, 2006.

[42] Q. Bao and K. P. Loh, "Graphene photonics, plasmonics, and broadband optoelectronic devices," *ACS Nano*, vol. 6, no. 5, pp. 3677–3694, 2012.

[43] F. Wang *et al.*, "Gate Variable Optical Transitions in Graphene," *Science*, vol. 320, no. 5873, pp. 206–9, 2008.

[44] R. Zan, U. Bangert, Q. Ramasse, and K. S. Novoselov, "Evolution of gold nanostructures on graphene," *Small*, vol. 7, no. 20, pp. 2868–2872, 2011.

[45] J. Le Xie, C. X. Guo, and C. M. Li, "Construction of one-dimensional nanostructures on graphene for efficient energy conversion and storage," *Energy Environ. Sci.*, vol. 7, no. 8, p. 2559, 2014.

[46] G. Goncalves, P. A. A. P. Marques, C. M. Granadeiro, H. I. S. Nogueira, M. K. Singh, and J. Grácio, "Surface modification of graphene nanosheets with gold nanoparticles: The role of oxygen moieties at graphene surface on gold nucleation and growth," *Chem. Mater.*, vol. 21, no. 20, pp. 4796–4802, 2009.

[47] P. V. Kamat, "Graphene-based nanoarchitectures. Anchoring semiconductor and metal nanoparticles on a two-dimensional carbon support," *J. Phys. Chem. Lett.*, vol. 1, no. 2, pp. 520–527, 2010.

[48] K. Jasuja and V. Berry, "Implantation and Growth of Dendritic Gold Nanostructures on Graphene Derivatives: Electrical Property Tailoring and Raman Enhancement," vol. 3, no. 8, pp. 2358–2366.

[49] Z. Li, Z. Cheng, R. Wang, Q. Li, and Y. Fang, "Spontaneous formation of nanostructures in graphene," *Nano Lett.*, vol. 9, no. 10, pp. 3599–3602, 2009.

[50] L. Scarabelli, M. Coronado-Puchau, J. J. Giner-Casares, J. Langer, and L. M. Liz-Marzán, "Monodisperse gold nanotriangles: Size control, large-scale self-assembly, and performance in surface-enhanced raman scattering," *ACS Nano*, vol. 8, no. 6, pp.

5833–5842, 2014.

[51] A. M. Funston, C. Novo, T. J. Davis, and P. Mulvaney, “Plasmon coupling of gold nanorods at short distances and in different geometries,” *Nano Lett.*, vol. 9, no. 4, pp. 1651–1658, 2009.

[52] B. G. Ghamsari, A. Olivieri, F. Variola, and P. Berini, “Frequency pulling and line-shape broadening in graphene Raman spectra by resonant Stokes surface plasmon polaritons,” *Phys. Rev. B - Condens. Matter Mater. Phys.*, vol. 91, no. 20, pp. 1–5, 2015.

[53] S. Heeg *et al.*, “Polarized plasmonic enhancement by Au nanostructures probed through raman scattering of suspended graphene,” *Nano Lett.*, vol. 13, no. 1, pp. 301–308, 2013.

[54] Q. Hao *et al.*, “Surface-enhanced raman scattering study on graphene-coated metallic nanostructure substrates,” *J. Phys. Chem. C*, vol. 116, no. 13, pp. 7249–7254, 2012.

[55] X. Li, W. C. H. Choy, X. Ren, D. Zhang, and H. Lu, “Highly intensified surface enhanced raman scattering by using monolayer graphene as the nanospacer of metal film-metal nanoparticle coupling system,” *Adv. Funct. Mater.*, vol. 24, no. 21, pp. 3114–3122, 2014.

[56] Y. Zhao, W. Zeng, Z. Tao, P. Xiong, Y. Qu, and Y. Zhu, “Highly sensitive surface-enhanced Raman scattering based on multi-dimensional plasmonic coupling in Au-graphene-Ag hybrids,” *Chem. Commun.*, vol. 51, no. 5, pp. 866–869, 2015.

[57] B. Liu, C. Tang, J. Chen, Q. Wang, M. Pei, and H. Tang, “Dual-band light absorption enhancement of monolayer graphene from surface plasmon polaritons and magnetic dipole resonances in metamaterials,” *Opt. Express*, vol. 25, no. 10, pp. 12061–12068, 2017.

[58] M. Khorasaninejad *et al.*, “Highly enhanced raman scattering of graphene using plasmonic nano-structure,” *Sci. Rep.*, vol. 3, pp. 1–7, 2013.

[59] G. Sarau *et al.*, "Enhanced Raman Scattering of Graphene using Arrays of Split Ring Resonators," *Adv. Opt. Mater.*, vol. 1, no. 2, pp. 151–157, 2013.

[60] S. Nouri, N. Ferdows, B. Z. Maryam, B. Samaneh, and H. Sepideh, "Field Enhancement in Metamaterial Split Ring Resonator Aperture Nano-Antenna with Spherical Nano-Particle Arrangement," 2018.

[61] A. Urich, A. Pospischil, M. M. Furchi, D. Dietze, K. Unterrainer, and T. Mueller, "Silver nanoisland enhanced Raman interaction in graphene," *Appl. Phys. Lett.*, vol. 101, no. 15, 2012.

[62] M. Grande *et al.*, "Fabrication of doubly resonant plasmonic nanopatch arrays on graphene," *Appl. Phys. Lett.*, vol. 102, no. 23, 2013.

[63] W. Fan, Y. H. Lee, S. Pedireddy, Q. Zhang, T. Liu, and X. Y. Ling, "Graphene oxide and shape-controlled silver nanoparticle hybrids for ultrasensitive single-particle surface-enhanced Raman scattering (SERS) sensing," *Nanoscale*, vol. 6, no. 9, pp. 4843–4851, 2014.

[64] M. Kerker, D.-S. Wang, and H. Chew, "Surface enhanced Raman scattering (SERS) by molecules adsorbed at spherical particles," *Appl. Opt.*, vol. 19, no. 19, p. 3373, 1980.

[65] R. L. Mccreery, *Raman spectroscopy for chemical analysis*. 2000.

[66] M. Moskovits, "Surface-enhanced spectroscopy," *Rev. Mod. Phys.*, vol. 57, no. 3, pp. 783–826, 1985.

[67] P. L. Stiles, J. A. Dieringer, N. C. Shah, and R. P. Van Duyne, "Surface-Enhanced Raman Spectroscopy," *Annu. Rev. Anal. Chem.*, vol. 1, no. 1, pp. 601–626, 2008.

[68] J. Dyer, "the Raman," vol. 33, no. 5, pp. 2375–2383, 1986.

[69] D. Voigt, E. C. Schilder, R. J. C. Spreeuw, and H. B. Van Linden van den Heuvell, "Characterization of a high-power tapered semiconductor amplifier system," *Appl.*

Phys. B Lasers Opt., vol. 72, no. 3, pp. 279–284, 2001.

[70] H. E. Keller, *Objective Lenses for Confocal Microscopy*. 2006.

[71] R. Heintzmann and G. Ficz, "Breaking the resolution limit in light microscopy," *Methods Cell Biol.*, vol. 114, no. 4, pp. 525–544, 2013.

[72] D. J. Brady, "Geometric Imaging," in *Optical Imaging and Spectroscopy*, John Wiley & Sons, 2009, pp. 11–50.

[73] M. M. Yang, W. J. Coleman, C. M. Silva, and M. R. Dilworth, "High resolution imaging microscope," *Biotechnol. alia*, vol. 4, no. May 2014, pp. 1–20, 1998.

[74] B. E. Saleh and M. C. Teich, "Ray Optics," in *Fundamentals of photonics*, New York: Wiley, 2009, pp. 1–35.

[75] I. Powell, "Design of a laser beam line expander," *Appl. Opt.*, vol. 26, no. 17, p. 3705, 1987.

[76] H. K. Raut, V. A. Ganesh, A. S. Nair, and S. Ramakrishna, "Anti-reflective coatings: A critical, in-depth review," *Energy Environ. Sci.*, vol. 4, no. 10, pp. 3779–3804, 2011.

[77] M. D. Morris and C. E. Buffett, "Inverse Raman and Raman Gain Spectra of Liquids and Solutions," in *Spectroscopy and Its Chemical Aplications*, 1982, pp. 519–531.

[78] R. A. Yotter and D. M. Wilson, "A review of photodetectors for sensing light-emitting reporters in biological systems," *IEEE Sens. J.*, vol. 3, no. 3, pp. 288–303, 2003.

[79] J. H. Scofield, "Frequency-domain description of a lock-in amplifier," *Am. J. Phys.*, vol. 62, no. 2, pp. 129–133, 1994.

[80] A. Yariv and P. Yeh, "Polarization of Light waves," in *Optical Waves in Crystals*, John Wiley & Sons, 1984, pp. 54–64.

[81] A. Yariv and P. Yeh, “Jones Calculus and its Application to Birefringent Optical Systems,” in *Optical Waves in Crystals*, John Wiley & Sons, 1984, pp. 121–147.

[82] B. E. Saleh and M. C. Teich, “Fiber Optics,” in *Fundamentals of photonics*, John Wiley & Sons, 2009, pp. 325–362.

[83] R. F. W. Pease, “Electron beam lithography,” *Contemp. Phys.*, vol. 22, no. 3, pp. 265–290, 1981.

[84] G. Vampa *et al.*, “Plasmon-enhanced high-harmonic generation from silicon,” *Nat. Phys.*, vol. 13, no. 7, pp. 659–662, 2017.

[85] M. A. de Araújo, R. Silva, E. de Lima, D. P. Pereira, and P. C. de Oliveira, “Measurement of Gaussian laser beam radius using the knife-edge technique: improvement on data analysis,” *Appl. Opt.*, vol. 48, no. 2, p. 393, 2009.

[86] C. A. Balanis, “Geometrical Theory of Diffraction: Edge Diffraction,” in *Advanced Engineering Electromagnetic*, John Wiley & Sons, 1989, pp. 765–777.

[87] P. B. Johnson and R. W. Christy, “Optical constants of the noble metals,” *Phys. Rev. B*, vol. 6, no. 12, pp. 4370–4379, 1972.

[88] D. E. Aspnes and A. A. Studna, “Dielectric functions and optical parameters of Si, Ge, GaP, GaAs, GaSb, InP, InAs, and InSb from 1.5 to 6.0 eV,” *Phys. Rev. B*, vol. 27, no. 2, pp. 985–1009, 1983.

[89] E. D. Palik, *Handbook of optical constants of solids Academic Press*. New York: Academic Press, 1985.

[90] Thorlabs, “HNL100R, HNL100L, HNL150R, HNL150L, HNL225R, HNL210L. Red HeNe Laser System User Guide,” 2017.

[91] Thorlabs, “Ø1" Laser Line Filter, CWL = 632.8 ± 0.6 nm, FWHM = 3 ± 0.6 nm. FL632.8-3.”

[92] Thorlabs, “Longpass Dichroic Mirror, 50% Transmission/Reflectance at 650 nm -

DMLP650R."

[93] Thorlabs, "UVFS Plate Beamsplitter, Coating: 350 - 1100 nm. BSW25, BSW26, BSW26R, and BSW27."

[94] Thorlabs, "PDA100A Si Switchable Gain Detector User Guide," pp. 1–16, 2015.

[95] "Model SR540 optical chopper," 2009.

Appendices

The appendices section includes information that can be useful for the reader but are not important enough to include in the main body of this thesis work. This section is mainly specifications of the used equipment.

A. He-Ne laser: HNL210L

The He-Ne laser specification supplied by Thorlab are seen in Table 3 [90].

Item #	HNL210L	HNL225R
Wavelength	632.8 nm	
Min Output Power (TEM_{00}, 633 nm)	21.0 mW	22.5 mW
Min Polarization Ratio	500:1	Random
Beam Diameter (TEM_{00}, $1/e^2$ points + 3%)	0.70 mm	
Beam Divergence (TEM_{00}, + 3%)	1.15 mrad	
Mode Purity (TEM_{00})	>95%	
Longitudinal Mode Spacing	257 MHz	
Max Noise (RMS) (30 Hz to 10 MHz)[4]	0.5%	
Max Drift with Respect to Mean Power, Over 8 hr	±2.0%	
Max Mode Sweeping Contribution	1%	
Beam Pointing Stability (25 °C)		
From Cold Start	<0.20 mrad	
After 15 min Warm-up	<0.03 mrad	
Operating Voltage (±100 V)	3800 VDC	
Operating Current (±0.1 mA)	6.5 mA	
Max Starting Voltage	10 kVDC	

Physical/Mechanical Characteristics	HNL210L	HNL225R
Max Warm-up Time (95% power)	20 min	
Expected Operating Lifetime	>40,000 hr	
Storage Lifetime	Indefinite (Hard-Sealed)	
Static Alignment	Center to Outer Cylinder within ±0.01". Parallel to outer Cylinder within ±1 mR	
Laser Head Weight	2.6 lbs (1.2 kg)	

Environmental	HNL210L	HNL225R
Temperature, Operating	-40 to 70 °C	
Temperature, Non-operating	-40 to 150 °C	
Altitude, Operating	0 to 10,000 ft	
Altitude, Non-Operating	0 to 70,000 ft	
Relative Humidity (non-condensing)	0 to 100%	
Shock	25 g for 11 ms, 100 g for 1 ms	

Safety	HNL210L	HNL225R
CDRH/IEC 60825-1 Class	IIIb/3B	

Table 3- HNL210L He-Ne laser specifications

B. Laser Line Filter: FL632.8-3

The transmittance curve of the laser line filter obtained from Thorlabs as seen in Fig. 1 [91].

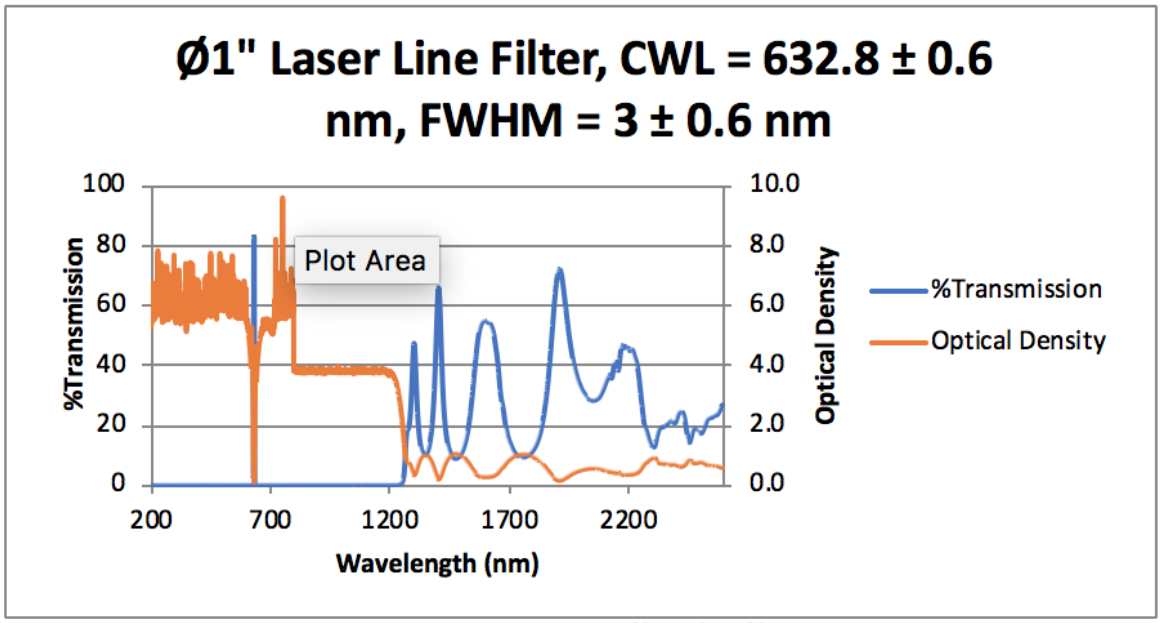

Fig. 1 -Transmittance of laser line filter

C. Dichroic Mirror: DMLP650 R

The transmittance and reflectance curves of the dichroic mirror obtained from Thorlabs as seen in Fig. 2 [92].

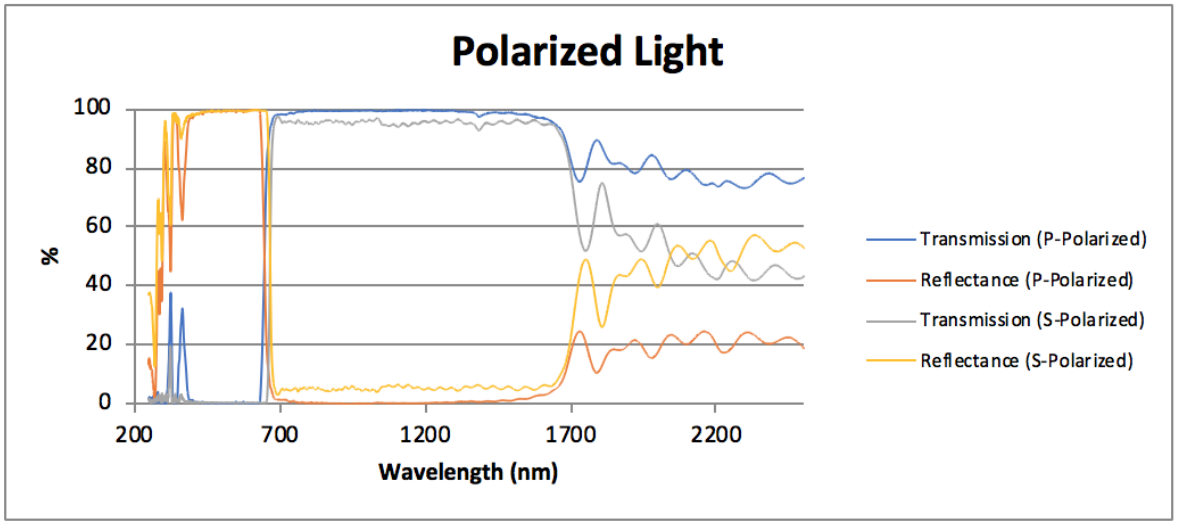

Fig. 2 - Transmittance and reflectance curves of the dichroic mirror

D. Beam Splitter: BSW26

The transmittance and reflectance curves of the beam splitter obtained from Thorlabs as seen in Fig. 3 [93].

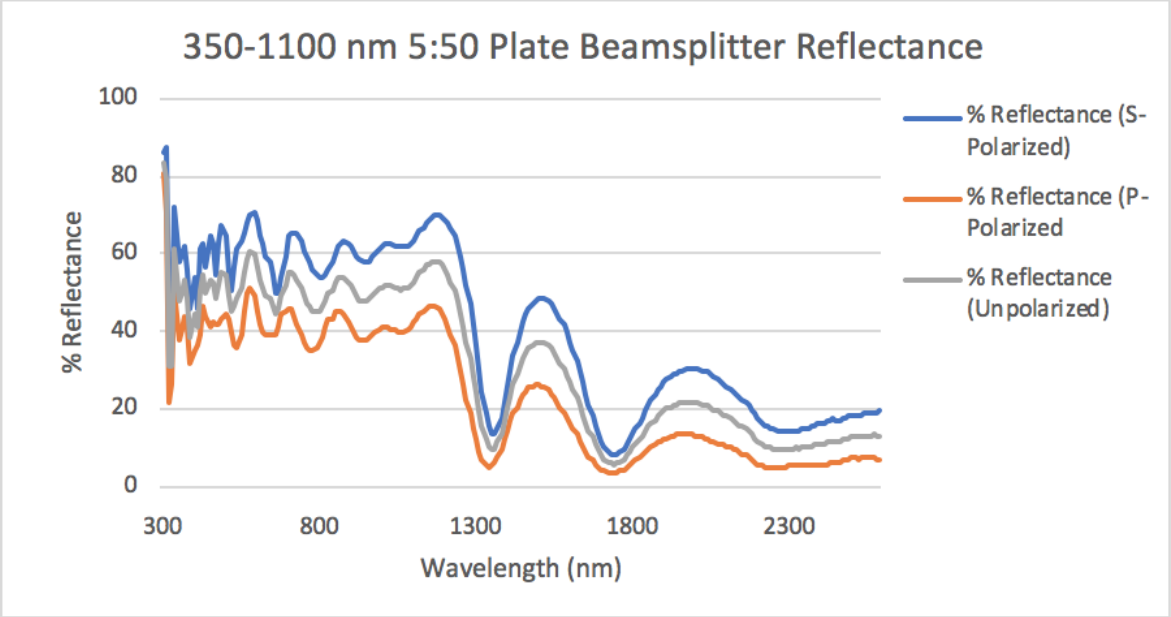

Fig. 3 - Transmittance and reflectance curves of the beam splitter

E. Photodetector: PDA100A

The photodetector specification supplied by Thorlab are seen in Table 4 [94].

Performance Specifications[2]			
0 dB Setting		**40 dB Setting**	
Gain (Hi-Z)	1.51 x 10^3 V/A ±2%	**Gain (Hi-Z)**	1.51 x 10^5 V/A ±2%
Gain (50 Ω)	0.75 x 10^3 V/A ±2%	**Gain (50 Ω)**	0.75 x 10^5 V/A ±2%
Bandwidth[3]	2.4 MHz	**Bandwidth[4]**	225 kHz
Noise (RMS)	254 µV	**Noise (RMS)**	799 µV
NEP (@ λ_p)	2.7. x 10^{-11} W/√Hz	**NEP (@ λ_p)**	3.55 x 10^{-12} W/√Hz
Offset	±5 mV (10 mV max)	**Offset**	±8 mV (15 mV max)
10 dB Setting		**50 dB Setting**	
Gain (Hi-Z)	4.75 x 10^3 V/A ±2%	**Gain (Hi-Z)**	4.75 x 10^5 V/A ±2%
Gain (50 Ω)	2.38 x 10^3 V/A ±2%	**Gain (50 Ω)**	2.38 x 10^5 V/A ±2%
Bandwidth[4]	1.6 MHz	**Bandwidth[4]**	78 kHz
Noise (RMS)	261 µV	**Noise (RMS)**	998 µV
NEP (@ λ_p)	1.1 x 10^{-11} W/√Hz	**NEP (@ λ_p)**	2.42 x 10^{-12} W/√Hz
Offset	±6 mV (12 mV max)	**Offset**	±8 mV (15 mV max)
20 dB Setting		**60 dB Setting**	
Gain (Hi-Z)	1.5 x 10^4 V/A ±2%	**Gain (Hi-Z)**	1.5 x 10^6 V/A ±5%
Gain (50 Ω)	0.75 x 10^4 V/A ±2%	**Gain (50 Ω)**	0.75 x 10^6 V/A ±5%
Bandwidth[4]	860 kHz	**Bandwidth[4]**	20 kHz
Noise (RMS)	349 µV	**Noise (RMS)**	1163 µV
NEP (@ λ_p)	8.91 x 10^{-12} W/√Hz	**NEP (@ λ_p)**	1.22 x 10^{-12} W/√Hz
Offset	±6 mV (15 mV max)	**Offset**	±8 mV (15 mV max)
30 dB Setting		**70 dB Setting**	
Gain (Hi-Z)	4.75 x 10^4 V/A ±2%	**Gain (Hi-Z)**	4.75 x 10^6 V/A ±5%
Gain (50 Ω)	2.38 x 10^4 V/A ±2%	**Gain (50 Ω)**	2.38 x 10^6 V/A ±5%
Bandwidth[4]	480 kHz	**Bandwidth[4]**	5.9 kHz
Noise (RMS)	561 µV	**Noise (RMS)**	1490 µV
NEP (@ λ_p)	4.65 x 10^{-12} W/√Hz	**NEP (@ λ_p)**	9.73 x 10^{-13} W/√Hz
Offset	±8 mV (15 mV max)	**Offset**	±30 mV (Max)

Table 4 - PDA Thorlabs photodetector specification

F. Optical Chopper: SR540

The optical specification supplied by Thorlab are seen in Table 3 [95].

SPECIFICATIONS

Chop Frequency	4 Hz to 400 Hz with 6 slot blade. 400 Hz to 3.7 kHz with 30 slot blade.		
Frequency Stability	250 ppm/°C typical.		
Long Term Frequency Drift	< 2%, 100 Hz < f < 3700 Hz		
Phase Jitter	0.2° rms from 50 Hz to 400 Hz. 0.5° rms from 400 Hz to 3.7 kHz.		
Frequency Display	4 digit, 1 Hz resolution, 1 Hz accuracy.		
Frequency Control	10 turn pot with 3 ranges: 4 Hz to 40 Hz 40 Hz to 400 Hz 400 Hz to 3.7 kHz		
VCO	0 to 10 VDC. Control voltage overrides frequency dial.		
Reference Modes	Switch	Left BNC	Right BNC
	up	f_{inner}	f
	middle	$5 \times f$	f
	down	$f + f_{inner}$	$f - f_{inner}$
Dimensions	Controller 7.7" x 5.1" x 1.8" Chopper Head 2.8" x 2.1" x 1.0" Blade Diameter 4.00"		
Power	100 / 120 / 220 / 240 VAC 50 / 60 Hz 12 Watts		
Warranty	Electronics - One year parts and labor on materials and workmanship. Chopper Motor - Ninety days parts and labor on materials and workmanship.		

Table 5 - Optical Chopper Specifications

G. Lock-in and piezo control code Supplementary material

This section discusses the overall functions of the lock-in and piezo controller code and then examines each section of the code in more depth. Figure 60, serves as the outline for the LabVIEW code that controls the stage and acquires data from the lock-in amplifier using the DAQ card. To begin the user inputs the different required data such as the axis parameters, communication ports for DAQ card and whether the scanning method is transposed or not. After the data is entered the code creates the required data arrays and calculate the necessary number of loops. Subsequently, a series of loops are followed to move the stage and collect the data while also displaying them to the user in real time. To end the code the stage is moved back to the original position to allow repetition of the sample scan. The code can also record the data in .txt file and abort the connections with piezo controller and DAQ. At any point if there is an error the program will abort and the user can also manually abort.

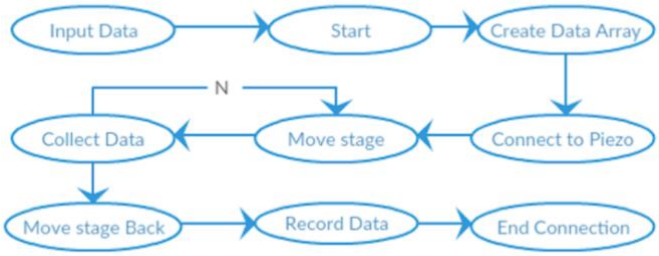

Figure 60- Overall LabVIEW code block diagram for controlling the lock-in amplifier and piezo controller while obtaining data from the DAQ card

Figure 61 is the front panel of the LabVIEW code. On the left side of the figure the required data parameters and instructions are displayed. The current location and voltage of the piezo controllers are also displayed on the top portion. Graphs are plotted while being collected from the DAQ card on the X-voltage and Y-voltage intensity graphs while being stored in the appropriate arrays. After the code is executed a final graph of the R-voltage intensity is plotted.

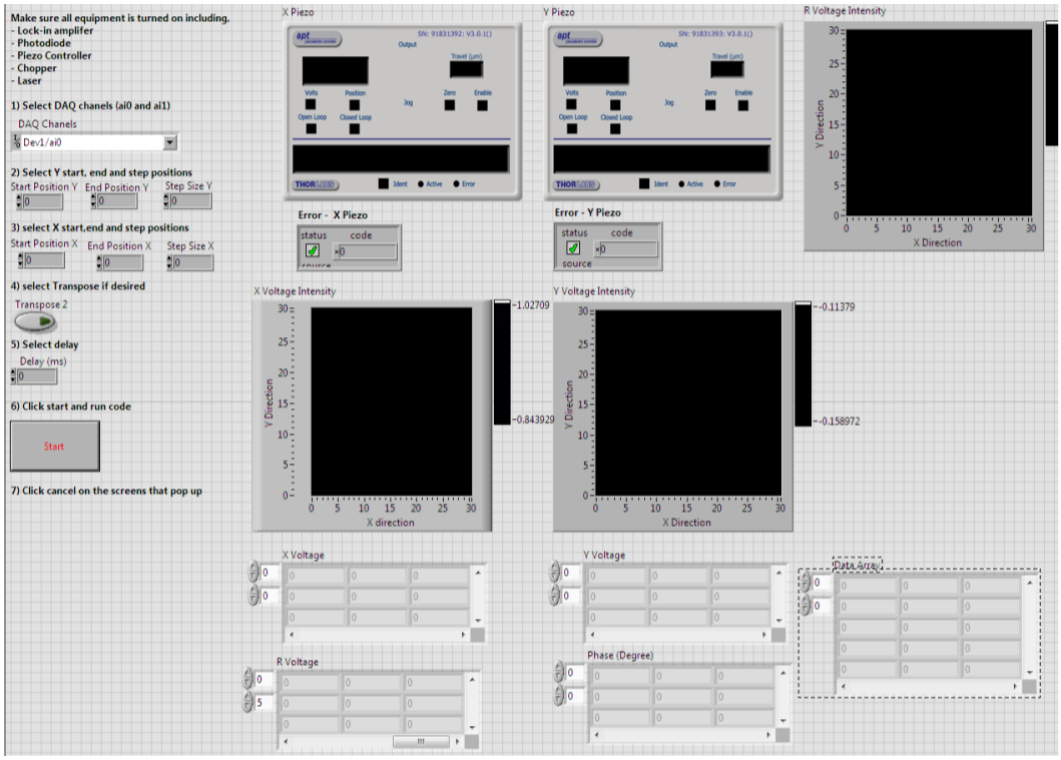

Figure 61 - LabVIEW front panel for controlling the lock-in amplifier and piezo controller while obtaining data from the DAQ card

The input parameters of the system are built to detect human error before the code is executed. Figure 61 shows the required axis parameters, a starting point, an end point and a step size for both axes in micrometer. The limitations of the stage allows a travel distance of $20\mu m$ in both directions and the actuators of the stage add an extra $10\mu m$ making the total travel distance $30\mu m$ in both directions. Thus, as a preliminary step the code will check if the total distance is smaller or equal to $30\mu m$ in both axes. In Figure 62 one can see that as a starting point the code tests if either step size of the axis is equal to zero and if so, the code is aborted and an error message is displayed. If the code is not aborted and the starting point is smaller than the ending point the code checks if the step size is bigger than zero. On the other hand, if the starting point is bigger than the ending point the code checks if the step size is negative. The code will allow the use of real numbers not only integers. When the code satisfies one of the conditions for both axes the program moves to the next stage of starting communication with the Piezo controller.

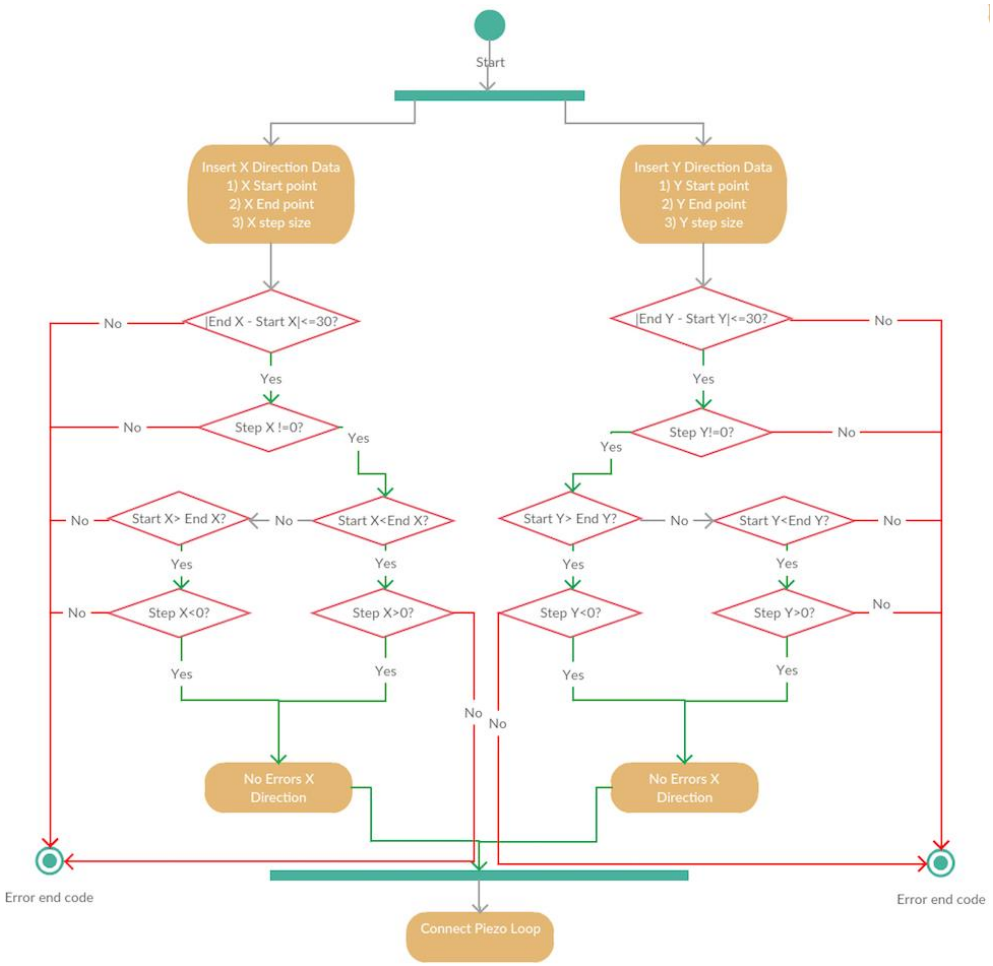

Figure 62 - x and y-axis parameters loop

The Piezo controller has a built in ActiveX LabVIEW component. ActiveX is a set of Microsoft technologies that allows the reuse of code to build the required computing program for ones needs. The piezo controller ActiveX is known as MG17Piezo. For each axes there is a different communication port and thus a different serial number. Figure 63 shows the flow of information to the piezo from obtaining the serial number to identifying closed or open loop and starting control. The user has the option of scanning in the x-axis first or y-axis by transposing the scanning method. If the transpose is chosen the serial numbers of the piezo controllers is switched around to make the rest of the code the same regarding the transpose. This can be seen in LabVIEW format in Figure 64.

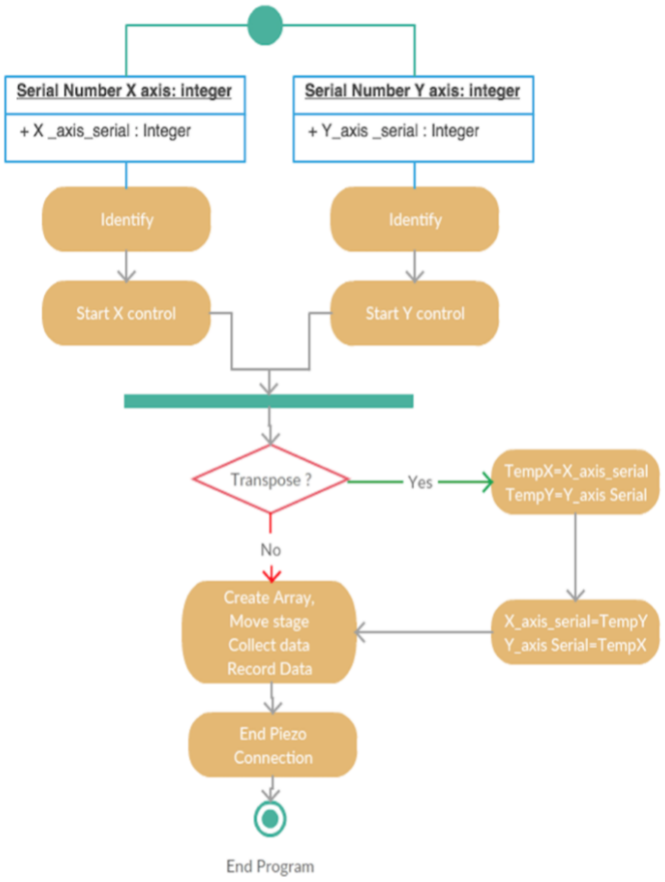

Figure 63 - Piezo Controller communication

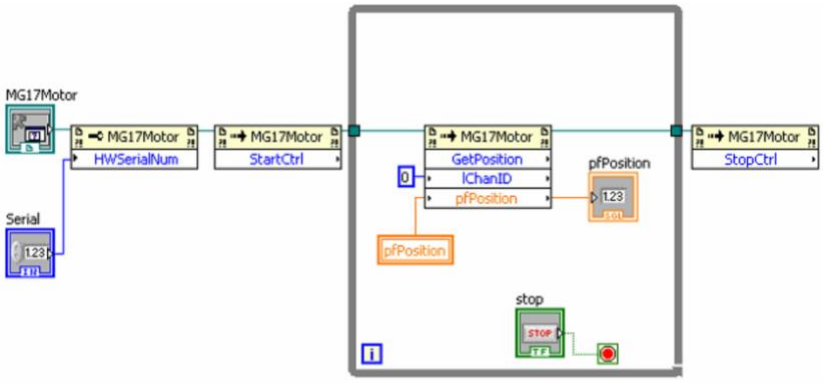

Figure 64 – Piezo controller simple get position loop

After the communication is started with the piezo controller the rest of the code is implemented such as, creating the array, moving the stage, and collecting and recording the data. The code than will terminate the connection with piezo controller before the execution ends.

In order to create the data array which consists of four columns, the axes position and the x and y voltages of the lock-in amplifier, the number of rows and the number of loop iterations is calculated. The LABVIEW code will concurrently find the number of x and y loop iterations labeled as Nx and Ny respectively as shown in Figure 65. Since the stage can move in the negative direction it's important to find the absolute of the difference of the end and start position.

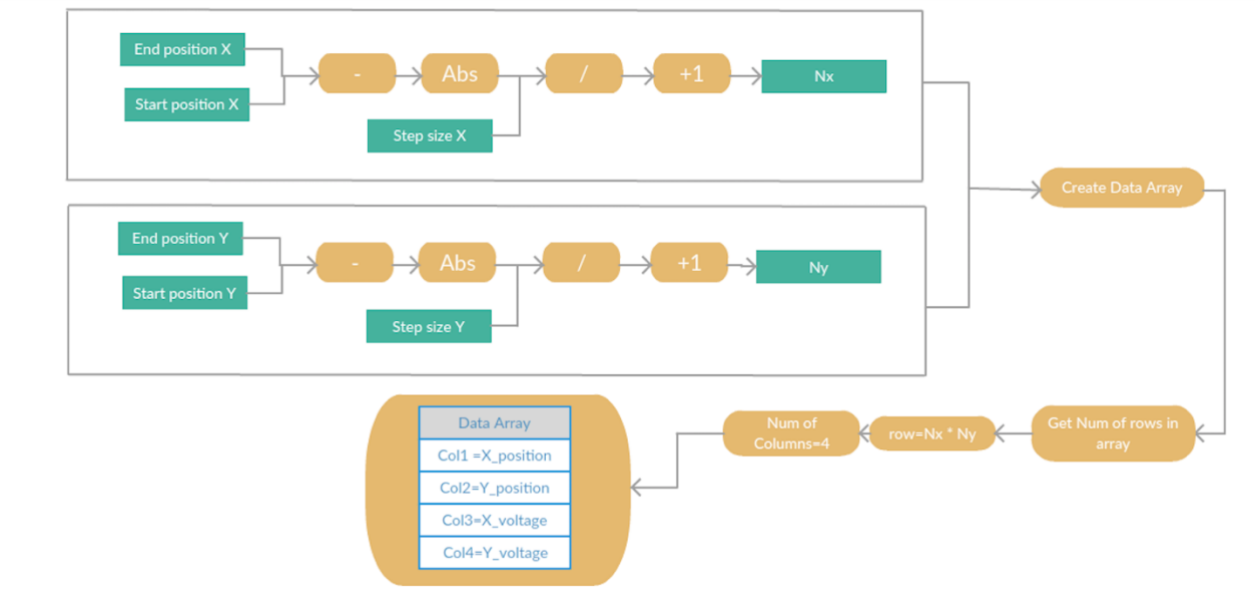

Figure 65 - Find number of iterations and create array

After the number of loops required to move the stage in a raster scan is found the stage will start by finding the y or x axis position depending on the transpose status. The code will then connect to the piezo controller and move the stage accordingly as seen in Figure 66. Moving the stage will consist of two nested loops, the outer loop moves it in the first direction by one step and the inner loop moving the full travel distance in the other direction. Not only will the inner loop move the full scan area it will furthermore connect to the DAQ card and collect the data from the 2-D data channels providing the x and y voltage readings from the lock-in amplifier at every (x, y) position. There is a delay of data collection which works with the lock-in amplifiers time constant as discussed in Section 3.1.8. The data is then recorded in the data array and the x and y voltage intensity graphs are displayed to the user.

After the stage travels the full array distance in the inner loop axis another loop is created for the stage inner axis to move back to the original position. Subsequently, the code

will go back to the main loop and move one step size until Ny or Nx loops are completed depending on the outer loop axis. After this point the output data array should include $Ny \times Nx$ rows. The nature of data collection may require multiple areal scans of the same region. Thus, before the code is terminated the stage must go back to the original position. This is done similar to moving the stage forward except position steps are subtracted from the current position instead of added, as can be seen in Figure 67. After the stage moves back to the original position the data is recorded and exported and all connections are terminated. This code is used to obtain measurements from the photodetector while keeping the laser position fixed but moving the sample which the stage is on. The sample on the stage is held together using a vacuum pump to avoid unwanted stage movement due to the shaking or the stage or surrounding area.

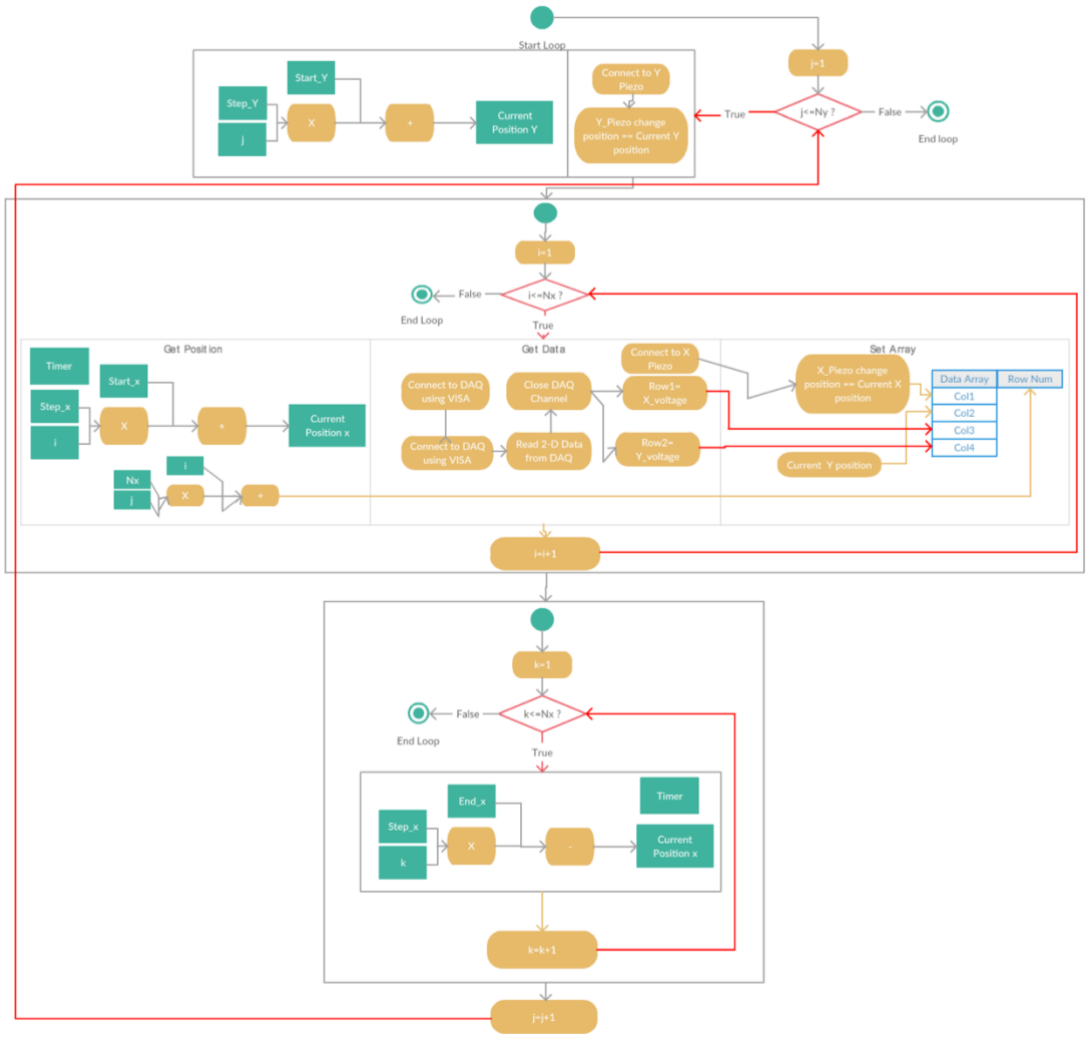

Figure 66 – Moving the stage in a raster scan fashion. If the code is transposed the x and y axis are switched around.

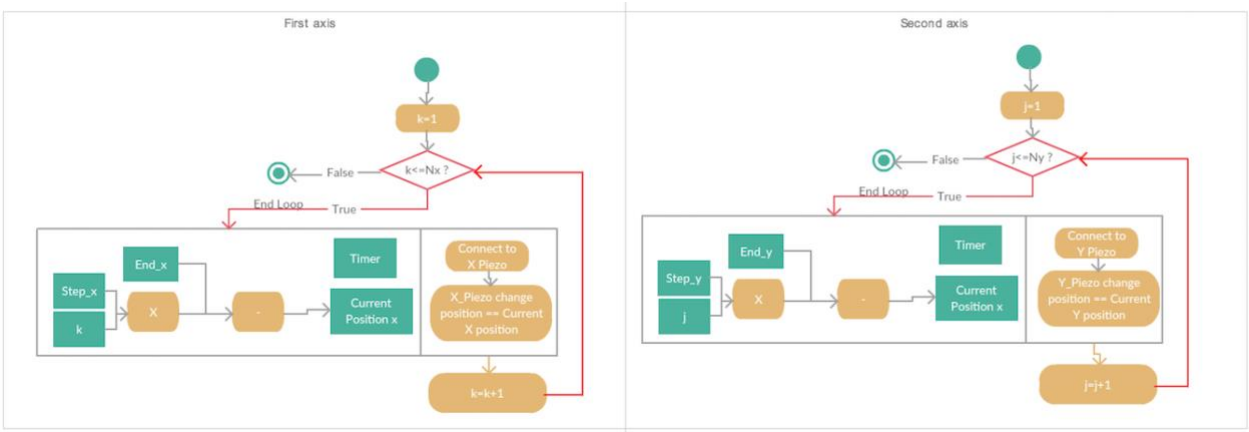

Figure 67 -Moving the stage back to the original position

H. SuperK control code supplementary material

This section discusses the overall functions of the SuperK code and then examines each section of the code in more depth. NKT photonics provides a LabVIEW and C codes that can be implemented into other codes. The LabVIEW code is used as a subVI in another LabVIEW code in order to control the stage and lock-in amplifier while scanning the wavelength. Figure 68 shows the front panel of the provided LabVIEW code and how it can be implemented into another VI. The register is responsible for deciding what is controlled in the laser, for example 90 is for the first wavelength peak since more than more wavelength can be chosen simultaneously.

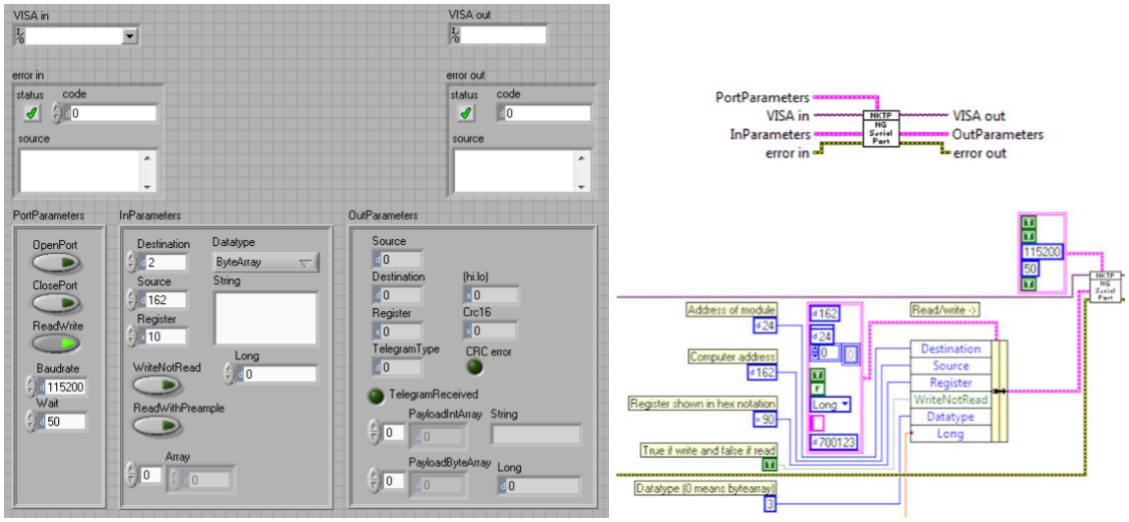

Figure 68 – a) SuperK front panel provided by NKT photonic. b)NKT code used as subVI

H.1 Scanning the stage and a wavelength range using LabVIEW

Similar to Appendix G overall block diagram of the code is seen in Figure 69. The program will similarly start by collecting data from the user, connecting to the Piezo controller (Figure 63) and creating the array. This is followed by a set of three nested loops to move the stage in a raster scan motion and scan the desired wavelength span. It will than end by moving the stage back to the original position and ending the connection with the Piezo controller and the laser.

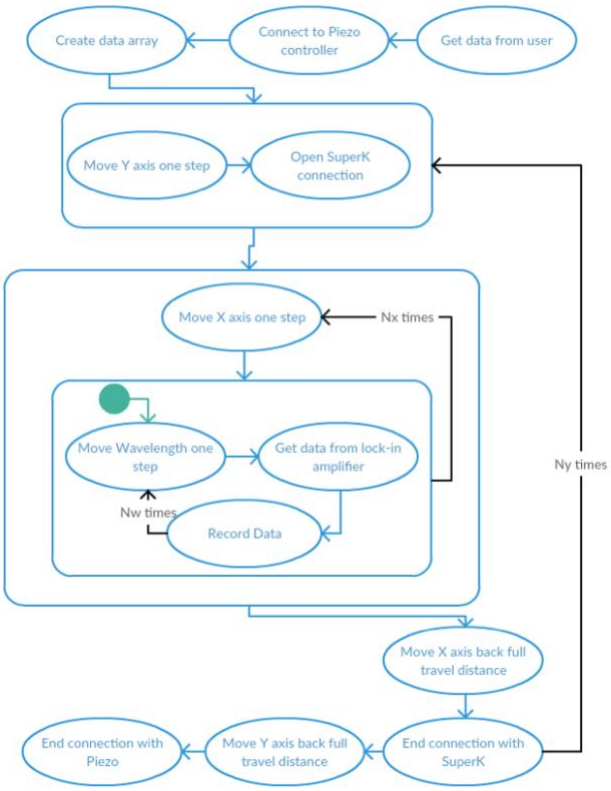

Figure 69 - Overall LabVIEW code block diagram for controlling the lock-in amplifier, piezo controller and SuperK while obtaining data from the DAQ card

Figure 70 is the front panel of the LabVIEW code controlling the SuperK and acquiring data from the DAQ card. On the left side of the figure the required data parameters and instructions are displayed. The current location and voltage of the piezo controllers are also displayed on the top portion. Finally, graphs are plotted in real time on the X-voltage and Y-voltage intensity graphs while also storing the data in the appropriate arrays. After the code is fully executed a final graph of the R-voltage intensity is plotted. This front panel is similar to that of Figure 61 with the addition of a step for the laser communication port and error. The graphs will plot the intensity of the last wavelength in the array.

Similarly, the code will check if the input data parameters are meaningful before the remainder of the code is executed. This is done in a similar approach as that of Figure 62. Furthermore, if the wavelength is out of range of the filter or laser being used the program will halt and display an error to the user. The wavelength of the laser changes and stabilizes in less than 50ms, however a bigger wavelength delay is desired to prevent any errors in the data collection.

In order to create the data array which consists of 5 columns, the wavelength, the axes position and the x and y voltages of the lock-in amplifier, the number of rows and the number of loop iterations is found for all three loops. The LabVIEW code will concurrently find the number of x and y loop iterations known as Nx and Ny respectively as shown in Figure 71 as well as the number of wavelength iterations Nw. Since the stage can move in the negative direction it's important to find the absolute of the difference of the end and start position. The number of rows is the number of all three iterations multiplied.

After the number of loops required to move the stage in a raster scan is found the program will then connect to the piezo controller and move the stage accordingly as seen in Figure 72. Moving the stage will consist of two nested loops, the outer loop moving it in the first direction by one point and the inner loop moving the full travel distance in the other direction. However, inside the loop is another loop for the wavelength. Thus, the stage will move one point in the y direction (or x if its transposed) and one in the x direction and travel the full wavelength distance before moving again in the x direction. Not only will the innermost loop move the full wavelength range it will furthermore connect to the DAQ card and collect the data from the 2-D data channels providing the x and y voltage readings from the lock-in amplifier at every (x, y) position and wavelength. During the acquiring of data there is a delay which functions with the lock-in amplifier time constant. The data is then recorded in the data array and the x and y voltage intensity graphs are displayed to the user for the last scanned wavelength.

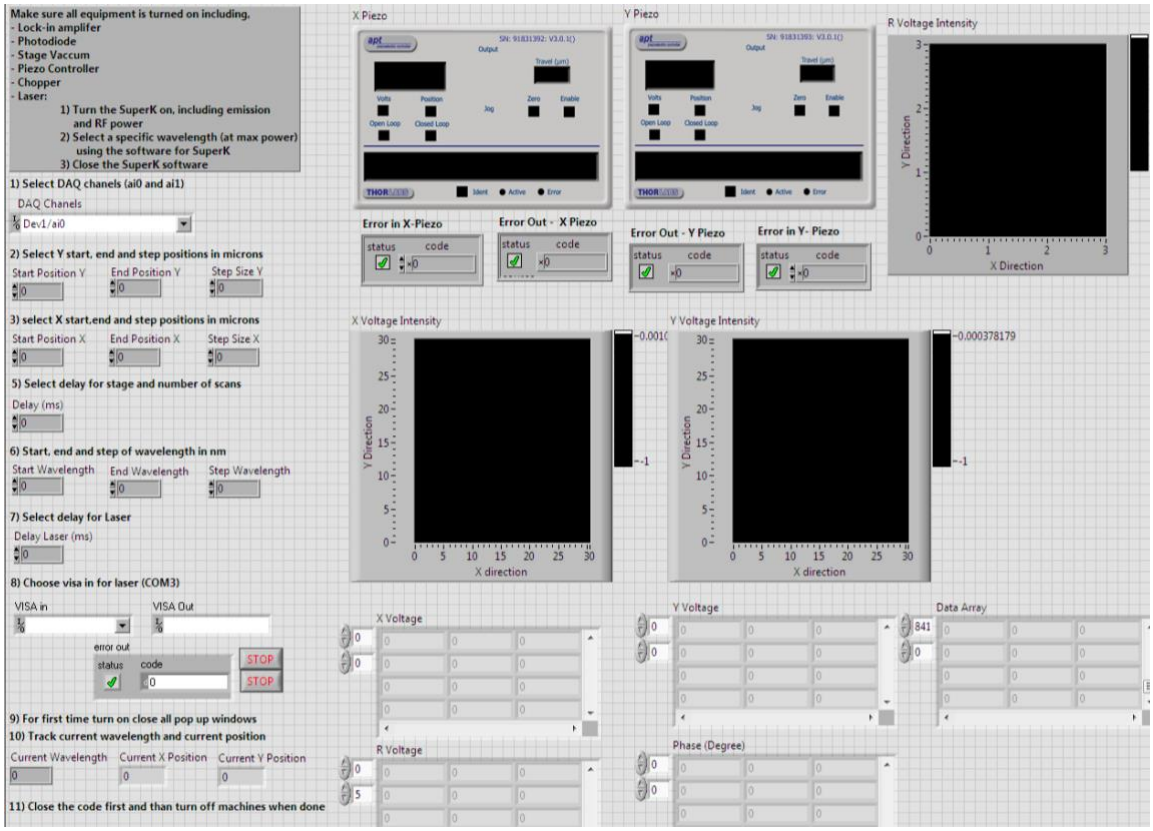

Figure 70 – LabVIEW front panel for controlling the lock-in amplifier, piezo controller and SuperK while obtaining data from the DAQ card

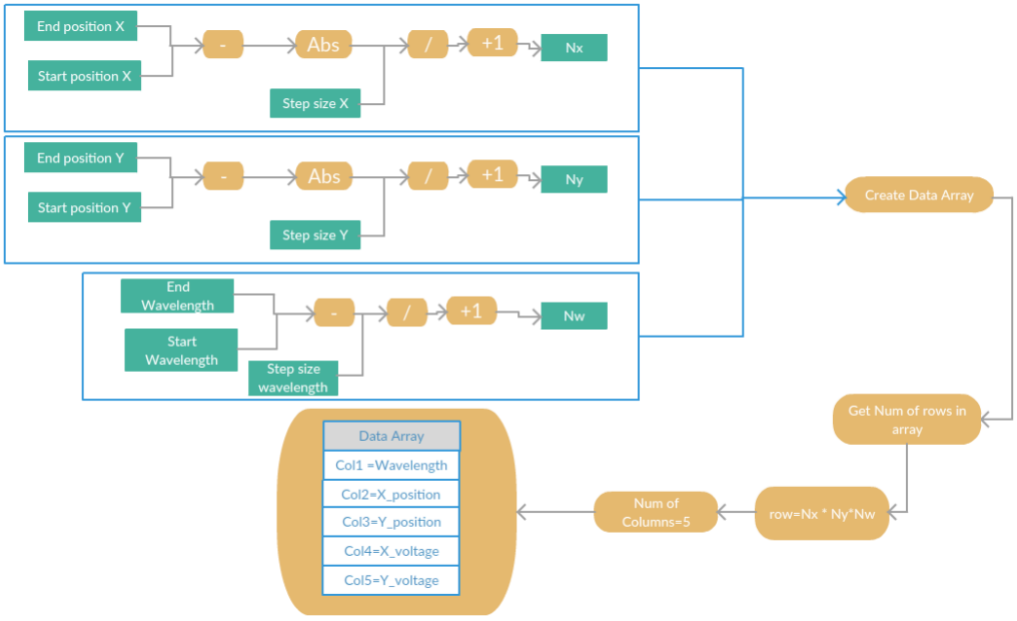

Figure 71 -Creating Arrays for controlling the SuperK, lock-in amplifier and stage

After the stage travels the full distance in the inner loop axis another loop is present for the stage inner axis to move back to the original position. Subsequently, the code will go back to the main loop and move one step size until Ny or Nx loops are completed depending on the outer loop axis. After this point the data array should include $Ny \times Nx \times Nw$ rows.

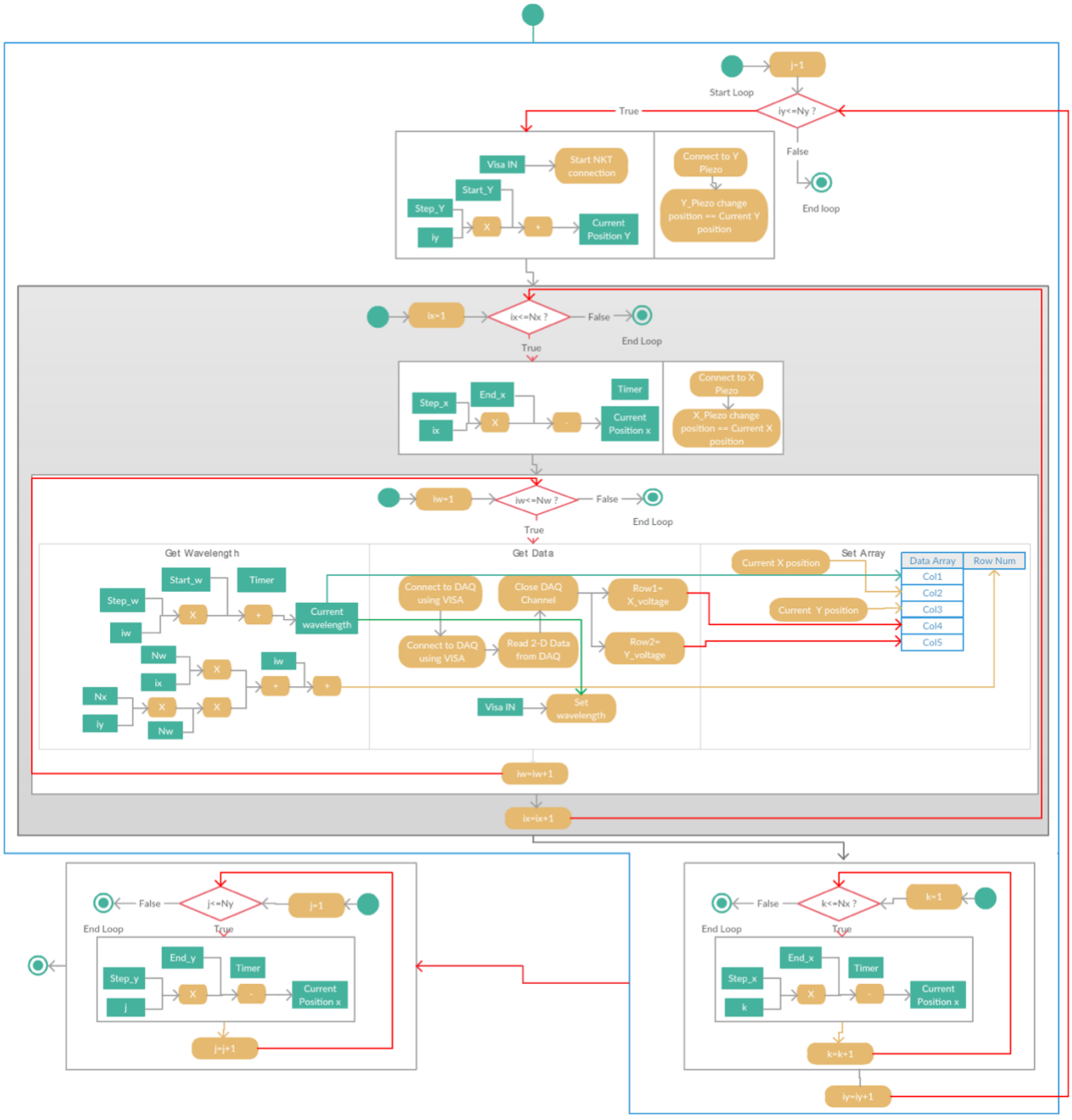

Figure 72 - Moving the stage in a raster scan fashion while scanning the desired wavelength span. If the code is transposed the x and y axis are switched around.

The nature of data collection may require multiple areal scans of the same region. Thus, before the code is terminated the stage must go back to the original position. This is done similar to moving the stage forward except position steps are subtracted from the current position instead of added. After the stage moves back to the original position the data is recorded and exported and all connections are terminated. The exported data can be further analyzed using MATLAB. The purpose of this code is to collect reflectivity measurements on an area at different wavelengths.

I. Approximate Price List

Description	Manufacturer	Part Number	Price
He-Ne Laser	Thorlabs	HNL210L	$2,540.00
Neutral Density Filter	Thorlabs	NDL-10S-4	$157
Laser Line Filter	Thorlabs	FL632.8-3	$140.76
Olympus Plan Flourite Objective Lens	Thorlabs	RMS20X-PF	$1,095.00
Plano-Convex lens	Thorlabs	LA1484-A	$29.10
Bi-Convex lens	Thorlabs	LB1757-A	$34.70
Dichroic Mirror	Thorlabs	DMLP650R	$490.00
Beam Splitter X 3	Thorlabs	BSW26R	$849
Photodetector	Thorlabs	PDA100A	$360.06
Achromat doublet lens	Thorlabs	AC254-200-A	$73.40
Eye-Piece		WF 10x/22	$90
FC/APC fiber collimator	Thorlabs	F220APC-850	$195.00
FC/APC fiber collimator	Thorlabs	F220APC-633	$195.00
Half wave plate	Thorlabs	AHWP05M-980	$814.98
Linear polarizer X 2	Thorlabs	LPNIRE100-B	$220.00
Bi-Convex lens	Thorlabs	LB1757-B	$36.21
Plano-Convex lens	Edmund optics	67-550	$39.00
Pin hole	Thorlabs	P5S	$73.00
Long-Pass filter	Thorlabs	FEL0650	$73.00
Aspheric Condenser	Thorlabs	ACL2520-B	$27.70
Plano-Convex lens	Thorlabs	LA1422-B	$31.90
Objective lens	Newport	40X 0.65NA	$225.50
Total Price of New parts			**$7,790.31**
Description	**Manufacturer**	**Part Number**	**Price**
Dual Phase lock-in amplifier	Scitec Inst.	420 lock-in	$1,990.98
DAQ	NI		$2,000
Super Extreme Continuum	NKT photonics	SuperK Extreme	$110,000
Nano-Max stage	Thorlabs	MDT630B	$3,869.88
Piezo controller	Thorlabs	PBC303	$4,662.42
Fiber	Thorlabs	NA	$300
Optical Chopper	SRS	SR540	$1,195.00
Spectrometer + CCD camera	Princeton Instruments		$88,000
Total Price of Lab Existing Equipment			**$212,018.28**
Total Price of New and Existing			**$219,808.59**